To the Graduate Council:

I am submitting herewith a thesis written by Lee Charles Wendell entitled "An Experimental Study of Incompressible Axisymmetric Cavity Flow with Swirl." I have examined the final electronic copy of this thesis for form and content and recommend that it be accepted in partial fulfillment of the requirement for the degree of Master of Science, with a major in Aerospace Engineering.

Ahmad Vakili
Major Professor

We have read this thesis and recommend
its acceptance:

Basil Antar

Christian Parigger

Acceptance for the Council

Linda Painter
Interim Dean of Graduate Studies

(Original signatures are on file with official student records)

An Experimental Study of Incompressible Axisymmetric Cavity Flow with Swirl

A Thesis
Presented for the
Master of Science
Degree
The University of Tennessee, Knoxville

Lee Charles Wendell
December 2006

Dedication

This thesis is dedicated to those people in my life for which words cannot adequately portray thanks and appreciation. To my wife and children, who stood by me through the initial desire to change career direction, obtain my Science Degree and complete my Masters. From the establishment of our goals, to the completion of this degree and onwards, I extend my deepest heartfelt appreciation.

Acknowledgements

This opus began some time before the physical writing began. The multitude of classes and late nights pouring over fluid mechanics texts in an effort to understand the nature and effects of fluids provided the basis for what you know hold before you. Of course, acknowledgement must go to Dr. Ahmad Vakili for his direction, guidance, and helpful manner in performing his role as thesis advisor and mentor. To the committee members, Dr. Basil Antar and Dr. Christian Parigger, I extend accolades for their role in contributing to the polishing of the draft and guiding me to the final product. To Dr. Abraham Meganathan, I offer my thanks for his participation in the testing and analysis phase. Thanks also go to Jeremy Smith for his patience and expertise in preparing me for this endeavour.

Acknowledgement must go to the technical staff, headed by Mr James Goodman. Chris Armstrong was thankfully there for patient interpretation of my drawings and construction of the apparatus, and Keith Walker for writing the critical data acquisition file for LabVIEW. Both were instrumental in the progress and advancement of this work.

I also want to thank my wife for her unwavering support throughout this whole ordeal. Thanks you, everyone, for not letting this experience evolve into something that could not be completed without your support.

Abstract

A systematic study was performed of the flow phenomena in an axisymmetric cavity. Axial flow Reynolds numbers ranged from 100,000 to 530,000 for cavity L/D range of 0.25 to 1.65. Working medium for this study was water reflecting that only incompressible domain of cavity flow was covered in this study. Previous results of axisymmetric flow investigations were reproduced and extended to lower L/D values, with the modified test article. Introduction of swirl in the cavity flow was studied in detail for its effects on the enhancement or suppression of cavity modes that have been measured.

The axial apparatus tested here recreated the results of that of the original apparatus. The values of the maximum peaks fell within the range of Helmholtz resonator values at that specific velocity, for a given L/D at and below L/D = 1.05, at the same flow conditions.

At and above moderate swirl numbers (S > 0.4), first mode of oscillation was completely suppressed. There was also evidence of a flattening of the remaining trend at higher swirl numbers (S > 0.6).

The range of maximum amplitudes experienced in this study was also in agreement with earlier work.

Overall, a trend of an increase of the frequency with an increase in swirl was seen in all tests. Generally, the range of greatest increase was for 47.23 ft/s axial flow, with the addition of 38.56 ft/s to 54.54 ft/s of tangential flow. The frequency increase was

attributed to the effects of swirl through the range of $0.3 < S < 0.6$. Over this range, the magnitude of the peak oscillation was seen to decrease markedly up to the point that the spectrum depicted no peaks, only a nominal level of broadband noise. This resulted in the conclusion that swirl effect existed only within a certain range of swirl numbers, and that the high swirl caused the elimination of certain cavity generated pressure oscillations.

With the introduction of swirl, through tangential injection, the frequency of peak oscillations in axisymmetric cavity flow can be controlled to a limited extend. The primary region of control lies in the moderate swirl number region of $0.3 < S < 0.6$.

The presence of helical modes in the flow was explored. Aliasing of high frequency acoustical tones is presented with peaks noted at the calculated values demonstrating the potential for the presence of helical modes in the flow. Helical modes were present at higher swirl velocities, with a trend approaching near agreement with theory.

Table of Contents

Chapter		Page
1	Introduction	1
	Objective	1
	Application	2
	Background	5
2	Technical Review	7
	Shear Layers	7
	Amplitude Enhancement	10
	Cavities	11
	Swirl	19
	Helical Modes and Aliasing	22
3	Experimental Approach	26
	Apparatus	26
	Flow Supply	28
	Cavity Model	32
	Pressure Transducer	47
	Computer Signal Processing	48

Chapter		Page
3 (cont.)	Calibration of Experimental Apparatus	50
4	Experimental Results and Discussion	53
	Basic Parameters	53
	Sources of Error	57
	Baseline Measurements	61
	Effects of Swirl	69
	Frequency Peaks	71
	Cavity Modes	71
	Swirl Flow	80
	Inlet Orifice Damage	85
	Helical Modes and Aliasing	85
5	Conclusion	94
	Results	94
	Future Study	96
List of References		97
Vita		102

List of Tables

Table	Title	Page
2.1	Table for aliasing value at first helical mode.	25
4.1	Average Velocity calculations based on gauge pressure readings.	55
4.2	Table of flux momentum (G) and Swirl Number (S) based on pressure readings at tangential injector valve.	56
4.3	Table of Strouhal Numbers (St) based on total velocity and frequency peak measured.	57
4.4	Rossiter's Empirical Constant.	59
4.5	Extrapolation of Rossiter's Empirical Constant.	60
4.6	Table of specification differences between transducers.	62
4.7	Frequency with corresponding mode number.	76

List of Figures

Figure	Title	Page
1.1	Pressure exerted by a train of slugs versus a steady stream.	4
2.1	Pressure distributions in a jet.	11
2.2	Description of the Cavity with the length to depth ratio (L/D) nomenclature.	12
2.3	Schematic representation of the cavity oscillation mechanism.	13
2.4	Classification of cavity flows as defined by the length to depth ratio (L/D).	14
2.5	Closed and open cavity flow.	16
3.1	Schematic of experimental Swirl Flow Cavity Chamber Apparatus.	27
3.2	Photo of apparatus elements (b) through (h).	29
3.3	Photo of apparatus swirl chamber (A) with cavity chamber (B) attached, 3” mounting adapter (C) and pressure transducer (D) installed.	30

Figure	Title	Page
3.4	Photo of apparatus swirl chamber tangential injection ports. Each port is 1/8” in diameter.	31
3.5	Cross sectional sketch of axial cavity depicting the inlet and exit orifices, pressure transducer mount and retaining rings.	33
3.6	Photo of Axial Flow (exit orifice end) apparatus.	34
3.7	Photo of Axial Flow (inlet orifice end) apparatus.	34
3.8	Cross Sectional sketch of apparatus swirl chamber and tangential injection ports (A).	35
3.9	Cross Section of Cavity Chamber Adapter.	37
3.10	Photo of elements that comprise the cavity apparatus (see narrative for dimensions).	39
3.11	Photo of inlet orifice-end flush face mounting.	40
3.12	Photo of swirl chamber apparatus (breakdown).	41
3.13	Photo of swirl tube spacer.	42
3.14	Photo of swirl chamber apparatus reservoir and swirl injector ports.	43
3.15	Photo of swirl chamber apparatus and cavity chamber (breakdown).	44

Figure	Title	Page
3.16	Photo of cavity chamber apparatus.	46
3.17	Photo of LabVIEW screen.	49
3.18	Chart with axial and tangential flow components.	52
4.1	Extrapolation of Rossiter's Empirical Constant.	60
4.2	Plot 1 of Axial Baseline Frequency Response with flow at indicated velocities.	63
4.3	Plot 2 of Axial Baseline Frequency Response with flow at indicated velocities.	64
4.4	Plot 3 of Axial Baseline Frequency Response with flow at indicated velocities.	65
4.5	Plot 1 of Tangential Baseline Frequency Response with flow at indicated velocities.	66
4.6	Plot 2 of Tangential Baseline Frequency Response with flow at indicated velocities.	67
4.7	Plot 3 of Tangential Baseline Frequency Response with flow at indicated velocities.	68
4.8	Effect of swirl on axial flow.	70
4.9	Graphs of Lower L/D Data (L/D=0.35) with associated velocities listed.	72

Figure	Title	Page
4.10	Graphs of Lower L/D Data (L/D=0.45) with velocities listed.	73
4.11	Graphs of Lower L/D Data (L/D=0.75) with velocities listed.	74
4.12	Plot of the Frequency versus L/D for Helmholtz Resonator, Smith [5], and tested results.	77
4.13	Plot of the frequency of maximum amplitude detected versus L/D at lower L/D ranges (0.35 < L/D < 1.35).	78
4.14	Graphs showing the mode shift with increase in flow velocity.	79
4.15	Plot of Strouhal Number versus Swirl Number.	81
4.16	Plot of peak amplitudes detected versus swirl number.	82
4.17	Plot of frequency versus Reynolds number for the range of L/D in this study.	83
4.18	Plot of Strouhal Number versus Reynolds number for the range of L/D in this study.	84
4.19	Plot 1 of power spectrum for Axial and Tangential flow.	86
4.20	Plot 2 of power spectrum for Axial and Tangential flow.	87
4.21	Photos of inlet orifice cap damage after testing.	88
4.22	Plot of the aliasing effect on longitudinal and helical modes.	89

Figure	Title	Page
4.23	Plot 1 of the first helical modes (peak A) present in swirled flow.	91
4.24	Plot 2 of the first helical modes (peak A) present in swirled flow.	92
4.25	Plot of the trend in observed frequency with increased swirl velocity.	93

Nomenclature

A	Rossiter's correction when Mach > 1.5
a_0	Speed of sound in the medium
D	Cavity depth
d_c	Diameter of a continuous jet
d_s	Diameter of a train of slugs
d_1	Cavity entrance orifice diameter
d_2	Cavity exit orifice diameter
F_c	Total force of a continuous jet
F_s	Total force of a train of slugs
f	Frequency
f_c	Natural frequency
f_{obs}	Observed frequency
f_{nyq}	Nyquist frequency
f_{act}	Actual frequency expected
f_{int}	Intended frequency
G_θ	Axial Flux of the Swirl Momentum
G_x	Axial Flux of the Axial Momentum
I.D.	Inside diameter
$j'_{m,n}$	Derivative of the Bessel Function – used in Helical Modes calculation

K	Rossiter constant for vortex propagation rate versus free-stream velocity
L_c	Reference length (usually cavity length or orifice diameter)
l_T	Length of throat – used to calculate Helmholtz Resonator frequency
$\frac{L}{D}$	Cavity length to depth ratio
$\frac{L}{U_\infty}$	Residence time
M	Mach Number
m	Integer mode number
n	Rossiter empirical constant
O.D.	Outside diameter
P	Pressure
P_s	Static pressure
P_t	Total pressure
q	Dynamic pressure
R	Radius of pinhole
R_{em}	Remainder
Re	Reynolds Number $\left(=\frac{\rho U_\infty L_c}{\mu}\right)$ based on cavity length
r_o	Radius of the swirl chamber
S	Swirl Number
St	Strouhal Number $\left(=\frac{fL_c}{U}\right)$ based on cavity length

t_1	Time for vortices to cross cavity
t_2	Time for vortices to interact with cavity trailing edge
t_3	Time for acoustic waves to cross cavity
U, U_∞	Average free-stream velocity
u, u_{m0}	Velocity in the x-axis, axial velocity
V_c	Volume of cavity
v	Velocity in the y-axis
w_{max}, w_{m0}	Maximum Tangential Velocity
x	Coordinate
y	Coordinate
z	Coordinate

Greek Symbols

γ	Rossiter's Empirical Constant
λ	Wavelength
μ	Viscosity of fluid
ρ	Fluid density
τ	Shear stress

Chapter One

Introduction

There are a number of publications covering the topic of cavity resonance generation, specifically those that resulted from the early problem of vibrations created once the bay doors were opened on World War II bombers [1]. Chahine and Johnson hypothesised that "self-resonating jets take advantage of the natural tendency of an axisymmetric jet to organize into large structures [2]". These structures then contact the trailing surface and take the form of pressure pulses travelling opposite to the direction of the flow. Rossiter [1] suggested an empirical solution to eliminate the tones through the use of a small spoiler that effectively reduces the large structure composition, thus eliminating the pressure oscillations. Several papers have been written concerning the principle [2 through 8] and control of the resulting flow. Experimentalists have also introduced swirl to the axial flow and have seen increases in flow heat transfer [9], flow energy and mass entrainment [10]. Additionally, Meganathan [4] and Majdalani [7] both noted vorticity in the flow downstream from the rectangular cavities.

Objective

The objective of this study was to recreate previous results and extend the L/D region below that established in [5], and to then introduce swirl to study the effects that a range of swirl numbers have on the flow.

Coherent structures are present in almost all turbulent flows and flow oscillations are generated in a number of ways, including exit end configuration [3], flow field-target interaction [11], and jet nozzle-target interaction [12]. The current study focuses on employing an axisymmetric nozzle with an internal cavity to generate unsteady pressure pulses at certain frequencies. Meganathan's [3, 4] experiments dealt with a compressible fluid, while the current study and that of Smith [5], dealt with an incompressible fluid. Here we utilized water as our working fluid.

The aforementioned cavities within the apparatus were created by the use of two orifices placed in line with an axisymmetric source flow. The length and depth of the cavity, and resultant pressure pulses created, were expected to overlap and be compared to that in [5] in order to explore the effects of lower Length to Depth (L/D) ratios. Once the optimum L/D was established to generate the maximum pressure peaks, further testing will be conducted to explore the effects of tangentially generated swirl on the frequencies and amplitudes of the peak tones created, specifically the related swirl number effect on the flow characteristics.

Application

Keeping in mind the original application of fluid mixing and emulsification, cleaning, cutting, deep hole drilling, and underwater sound generation of Chahine and Guo [6, 9], the added twist here is an increase in flow energy and heat transfer with the introduction of swirl to the axisymmetric flow [9]. Jet growth, mass entrainment, and velocity decay [12] are additionally experienced. Gupta [10] has also found that the flow is affected by the degree of swirl generated in the flow.

The primary concern in new applications is the efficient operation and reliability of the device. Practicality and ease of construction, specifically the construction that minimized the moving parts involved, is the goal. Eventual miniaturization for application in vehicle fuel mixing is discussed in Smith, where "fewer moving parts would aid achievement of this aim of reliability, but mixing needs to be done within a minimal space [5]." Guo and Dhir state that "swirl flow is one of the techniques that has been used successfully in the past to augment heat transfer [9]". Swirl has important application in flame control and stability, "ranging from dust separators through to burner systems, they offer good fluid mixing and long residence times for complete reactions to take place [13]".

The formulas for the train of slugs versus the force exerted by a stream of water are [5]:

$$F_c = \frac{1}{2}\rho U^2 \cdot \frac{\pi d_c^2}{4} \tag{1.1}$$

and

$$F_s = \frac{1}{2}\rho U a_0 \cdot \frac{\pi d_s^2}{4} \tag{1.2}$$

with ρ and U the density and velocity of the water, and a_o is the speed of sound in water. The diameter of the core of the flow is represented by d_c and d_s. Graphically, as in Figure 1.1, the pressure exerted by a train of slugs increases much more rapidly since the speed of sound (a_o = 4862 ft/s @ 20° C/70° F) in the medium is used in the calculation and is two orders of magnitude higher than the speeds we employ in these tests (72 ft/s implies M = 0.0148).

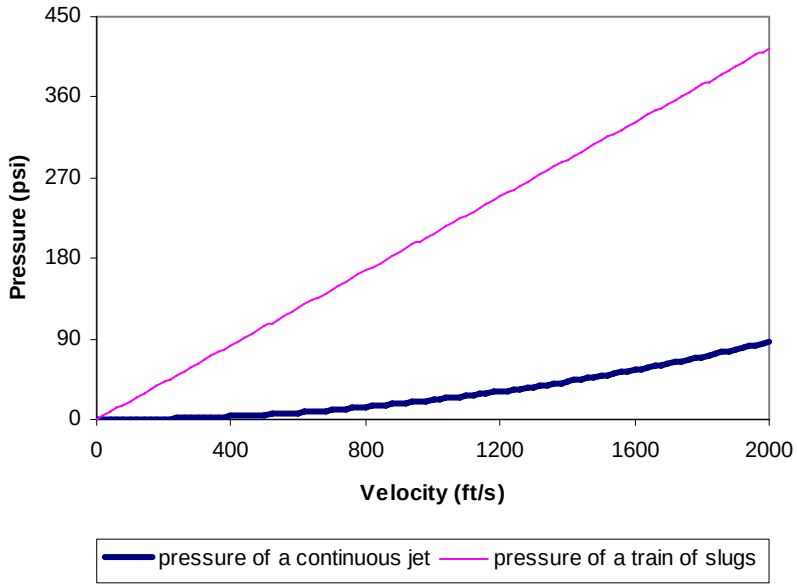

Figure 1.1. Pressure exerted by a train of slugs versus a steady stream.

With the addition of tangentially injected swirl to the flow, not only is the mass flow rate increased, but the tangential shear stresses contribute both a destabilizing effect on the flow in addition to a stabilizing effect due to the centrifugal force of the swirling component of velocity [14]. Here we utilize the stabilizing effect to suppress the turbulent effects. For simplicity the swirl numbers will be calculated using, from Gupta [10],

$$S = \frac{G/2}{1-(G/2)^2} \tag{1.3}$$

with,

$$G = \frac{w_{\max}}{u} \tag{1.4}$$

where we use w_{max} as the maximum tangential velocity injected into the flow, and u as the maximum axial flow velocity. This swirl number formula was employed using the calculated axial and tangential flow velocities. A rigorous derivation will be presented in Chapter Two.

An increase in energy is anticipated to complement the cleaning and drilling capabilities of the swirl injected flow. The swirl also aids in mixing and duty cycle in chemically reactive flows, although here we are primarily concerned with the resultant flow characteristics of water.

Background

Through continuation of the work of Smith [5], the frequency and duty cycle of the cavity chamber was re-established and then swirl was added to the flow to measure the swirl effects on the flow. In constructing the apparatus to inject swirl into the flow, we are using the active means to create the pressure pulses through mass injection [11]. Additionally, the work of Meganathan [3] and Majdalani [7] were used for the exploration of the vortical nature of the flow downstream of the cavity. They showed swirl increased jet growth rates and thus entrainment of ambient fluid, although not intentionally introducing swirl. Here we are utilizing both active and passive means to create the pulses in the flow. The active means employed are mass injection upstream [11] with swirl, and passive means through the employment of the cavity chamber orifice arrangement.

Similarly, in other studies [2, 3, 4, 11, 14 – 17], the nature of the flow over rectangular cavities was explored in two dimensions. The goal of these analyses is to

provide a good understanding of the nature of the flow and then apply the goals and assumptions to our three dimensional case of axisymmetric cavity flow with and without swirl.

Chapter Two will contain a discussion on the nature of cavity flows as well as the swirl phenomenon. The experimental approach taken here is described in detail in Chapter 4. The results and discussion are presented in Chapter Five, with recommendations for future study in this field.

Chapter Two

Technical Review

The flow of air over an open cavity formed in the surface of an aeroplane is usually unsteady, and large fluctuations may occur in the pressure acting on the walls [1]. The open cavity formed well for analysis in two dimensions. When the pressure, evolving into harmonic disturbances, are introduced into a rectangular cavity with compliant walls, a rotational component of the time-dependent velocity is produced along with the plain, irrotational, acoustic field [7]. If we were to intentionally introduce a tangential force into a three dimensional version of this cavity, in the form of axisymmetric flow, there are two counter effects seen within the flow. One is a destabilizing effect, due to the large shear forces, and the other is a stabilizing effect, due to the centrifugal forces within the flow [14]. These forces are created through injecting mass into the flow at strategic locations.

Shear Layers

A discussion on the nature and characteristics of turbulent flow and shear layers is required for understanding the nature of flows in cavities that follows. The reader is directed to Smith [5] for an admirable discussion on these topics. For brevity, the discussion here will confine itself to briefly describe the topics below:

1. Boundary Layer Properties.

   For three dimensional flow upstream of the cavity, shear stress is:

$$\tau = \mu\left(\frac{\partial u}{\partial y} + \frac{\partial v}{\partial x} + \frac{\partial w}{\partial z}\right) \tag{2.4}$$

where τ is the shear stress, μ is the viscosity of the fluid, and u, v, w and x, y, z are the component velocity and directions respectively as the flow moves in the positive x direction ($u >> v$ and $u >> w$). The boundary layer conditions will exist prior to the cavity, and so $\frac{\partial u}{\partial y} >> \frac{\partial v}{\partial x}$ and $\frac{\partial u}{\partial y} >> \frac{\partial w}{\partial z}$, thus we can assume the shear stress as in a 2-D fluid,

$$\tau = \mu\left(\frac{\partial u}{\partial y}\right) \neq 0\,. \tag{2.5}$$

Boundary layer separation occurs when the shear stress is zero, and will occur for axial flow through the apparatus. With the addition of tangentially injected swirl, this is no longer the case, as we will see in the next section.

2. Shear Layers.

(a) Free Shear layers. Shear layer instability leads to the growth of perturbations along the shear layer generating shear layer vortices. Smith [5] describes free shear layers in regards to these experiments, and in particular, the shear layer growth and how the vortices roll up to form coherent structures. Free shear layers are created by an upstream means, including.

(i) between parallel streams of dissimilar velocities;

(ii) in wakes; and

(iii) in jets [23].

Shear layers develop and spread in an open ambient fluid with velocity gradients contained within the shear layer. They are unaffected by walls or barriers but will propagate their pressure gradients over time and space. Having the dominant free shear velocity move in the x-direction at a velocity of u, and knowing that the Reynolds Number (Re) is large, the boundary-layer approximations hold true:

(i) $u >> v$;

(ii) $\frac{\partial u}{\partial y} >> \frac{\partial u}{\partial x}$; and

(iii) $\frac{\partial P}{\partial y} = 0$.

With no confining barriers to free shear layers, we effectively have no pressure change in the axial direction. Despite the absence of walls to maintain the no-slip condition, the conditions above allow the plane free shear flows to conform to the flat plate equations [5]:

$$\frac{\partial u}{\partial x} + \frac{\partial v}{\partial y} = 0 \text{; and} \tag{2.6}$$

$$u\frac{\partial u}{\partial x} + v\frac{\partial u}{\partial y} \approx v\frac{\partial^2 u}{\partial y^2}. \tag{2.7}$$

(b) Confined Shear Layers. Once a cavity is placed in the flow path, the shear layer within the cavity is considered a confined shear layer. The pressure oscillations and shear layer interaction within the cavity are constrained within the cavity wall, which results in the characteristics of forced shear layer [5].

(c) Forced Shear Layers. This type of shear layer can occur through several means, specifically mechanical, acoustical and fluidic. The key factor is that the method must be spatially coherent in order for the shear layer forcing to result in an increased shear layer growth rate. The parameters of shear layer forcing include [5]:

(i) Frequency;

(ii) Phase; and ,

(iii) Amplitude [16].

Of these factors, frequency is the most effective and that is the primary reason Rossiter's empirical formula can be utilized to a certain degree of success.

3. Cavity Shear Layer Forcing. Having the cavity placed in the flow path results in forced shear layer since the interaction of the shear layer departing the inlet orifice, the ensuing collision with the trailing edge, and the interaction with the pressure feedback in the form of acoustic radiation. It is the feedback of acoustic waves that act as a forcing frequency for the shear layer, which attempts to adjust the shear layer to this frequency. The length of the cavity determines the frequency for the given flow and if the forcing frequency is matched to the cavity resonant frequency, then higher level self-sustained oscillations will result [5]. The ability to adjust the cavity length in this experiment determines when the peak oscillations occur.

Amplitude Enhancement

It is interesting to point out that Chan [26] determined the optimum Strouhal Number (St) where the peak amplification occurred. He determined that (see Figure 2.1)

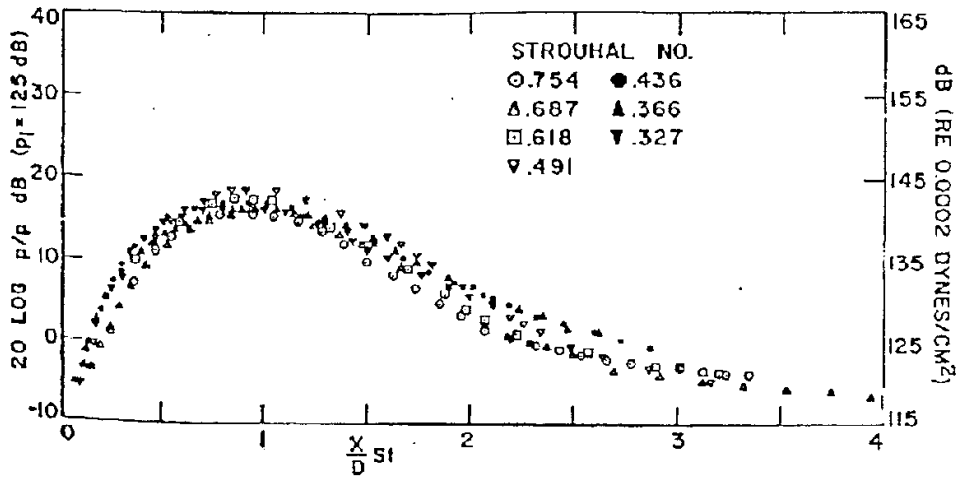

Figure 2.1. Pressure distributions in a jet (from Chen [26]).

at approximately St = 0.92, there was a considerable increase in the amplitudes of the tones generated.

Within the analysis contained in this paper, the range of Strouhal Numbers covers this region, specifically in the region around (X/D)St = 0.9. In this study, the values utilized are L/D = 0.9, resulting in (X/D)St = 0.82.

Cavities

In order to understand the concept of acoustic tone creation, we must look at the construction of the cavity, specifically the length to depth ratio (L/D), as well as the forces behind the creation of flow characteristics. Figure 2.2 shows a two-dimensional view of a cavity and the corresponding nomenclature involved. Varying the length or depth of the cavity will create two classifications of cavities. Shallow cavities have the

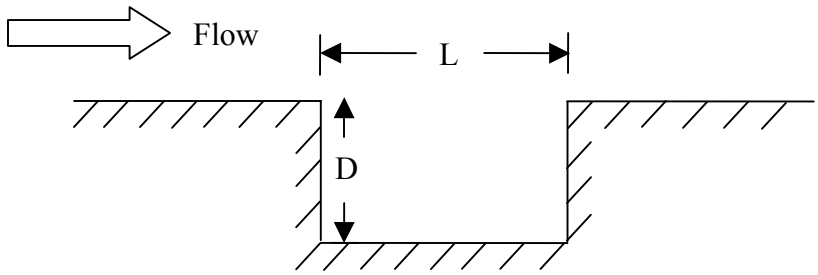

Figure 2.2. Description of the Cavity with the length to depth ratio (L/D) nomenclature.

longest dimension in the streamwise direction, with a corresponding L/D > 1. Deep cavities have the greatest dimension perpendicular to the flow with a corresponding L/D < 1 [4]. In this experiment, we will deal strictly with deep cavities.

From [4], Figure 2.3 shows the mechanism involved in creation of the cavity oscillations. The shear layer rolls up into vortices after departing the leading edge, eventually forming larger and larger structure and then collides with the trailing edge of the cavity.

This collision of the vortices with the trialing edge is the mechanism for the creation of pressure pulses, resulting is an audible tone.

There can be a variety of configurations involved in the construction of the cavity. The depth and length can vary to create three regimes within the flow. Figure 2.4 contains a description of the flow regimes with respect to the various L/D ratios.

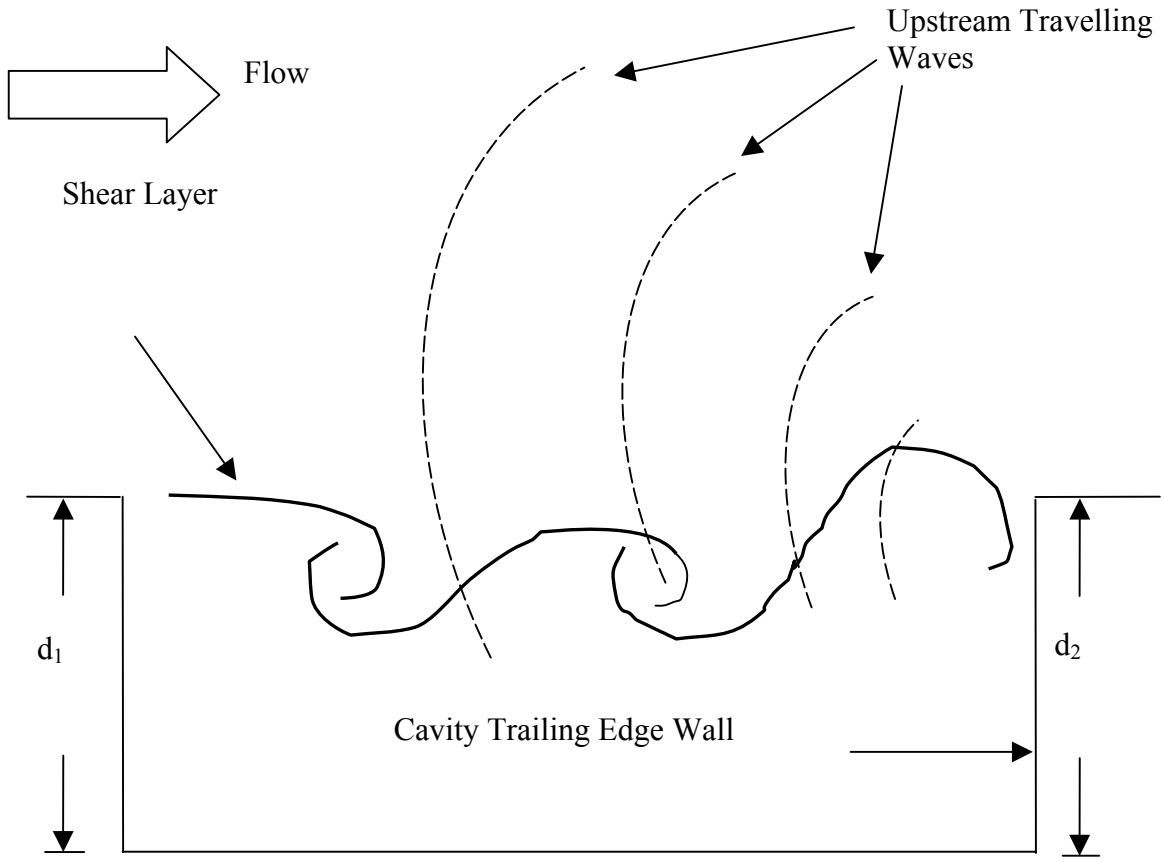

Figure 2.3. Schematic representation of the cavity oscillation mechanism. Here we have d_1 and d_2 as the inlet and exit orifice dimensions, where $d_2 > d_1$, in our experiment.

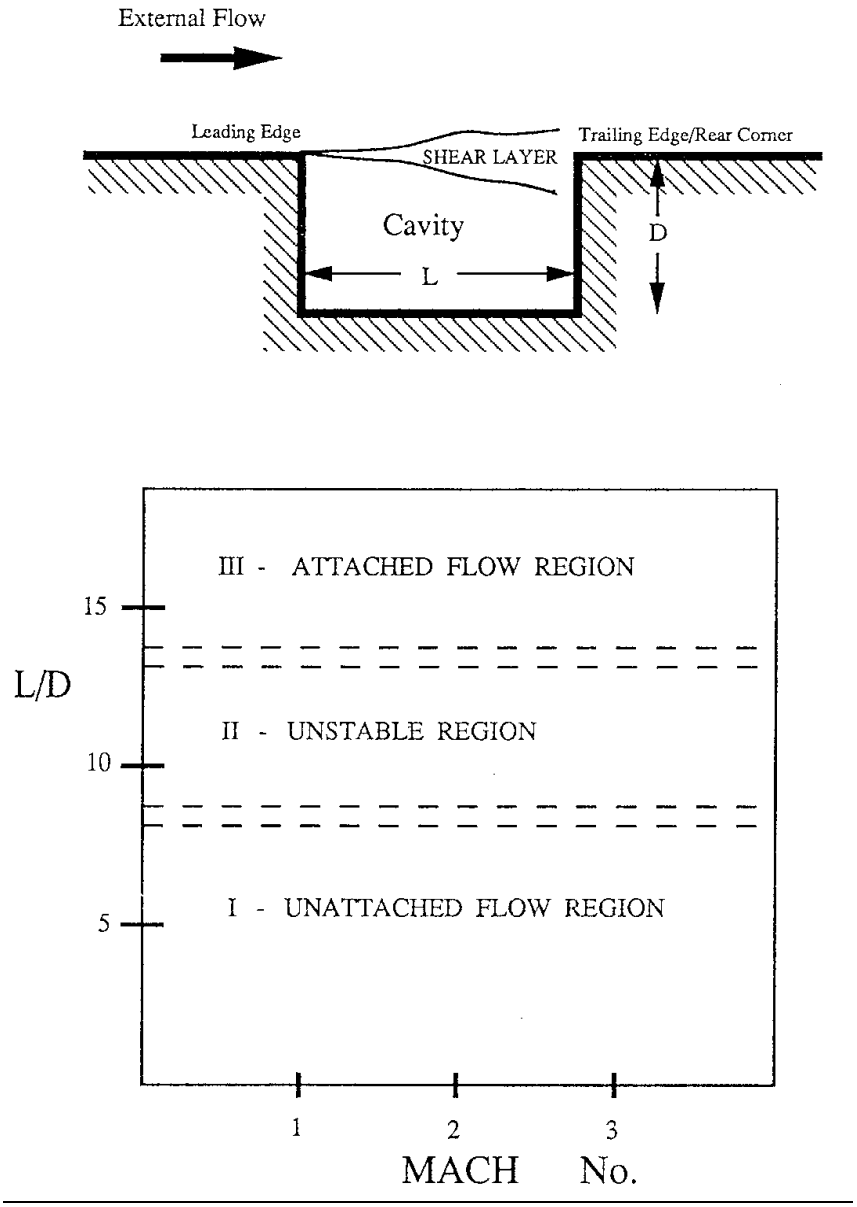

Figure 2.4. Classification of cavity flows as defined by the length to depth ratio (L/D) [20].

The flow in region I remains predictably unattached to the cavity floor, with a recirculation zone dominating the interior of the cavity (see Figure 2.5 (b)). In region III, the flow attaches to the floor due to the length and has recirculation zones below the leading and trailing edges (see Figure 2.5 (a)).

Region II in Figure 2.4, described as unsteady, refers to the periodic attachment and reattachment of the flow to the bottom of the cavity. The flow regime here does not remain attached, as in region III, for any predictable period. Thus the region here is described as unsteady.

The L/D, a convenient non-dimensional parameter, has been found to be useful in dividing cavity flow into three categories [20]. These are considered when dealing with shear layer attachment [4]:

1. Closed Cavity-Flow Region. When L/D is large (Region III, Figure 2.4) the external flow attaches to the bottom of the cavity and then ascends at the aft portion to exit the cavity, with small recirculating regions below the steps (shown in Figure 2.5 (a));
2. Open Cavity-Flow Region. For small L/D (Region I, Figure 2.4), the external flow enters the cavity, and fills the cavity with recirculating flow that forms a barrier to prevent further external flow from entering. The remaining external flow passes over the cavity (shown in Figure 2.5 (b)); and,
3. Transition Cavity-Flow Region. There is a range of values for L/D (Region II of Figure 2.4) that cannot be defined by the closed or open

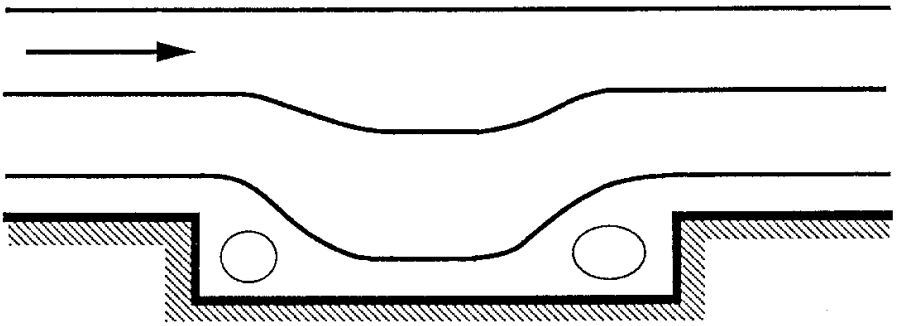

(a) Closed (attached) cavity flow for large L/D ratio

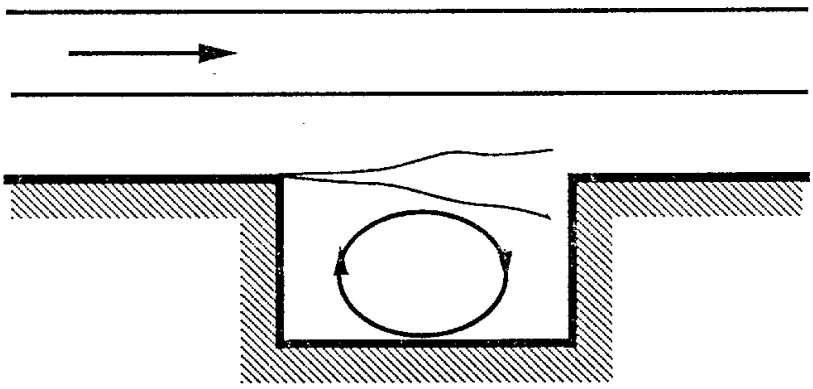

(b) Open (unattached) cavity flow for low L/D ratio

Figure 2.5. Closed and open cavity flow [21].

regions. This is because the flow is unstable and the external flow attaches and detaches from the bottom of the cavity. Basically, the flow alternates between the two types.

In viewing the transition region, Karamcheti [22] found that, after studying a shallow, open flow cavity of variable length, there was a minimum length of cavity below which the shear layer traverses the cavity and does not interact with the trailing edge. From here Rossiter [1] found that vortices were created from the leading edge that, given sufficient length of cavity, would roll up and collide with the trailing edge of the cavity.

Rossiter formulated an empirical equation that predicted the frequencies of oscillations generated within the cavity. The equation is:

$$St = \frac{fL}{U_\infty} = \frac{m - \gamma}{\frac{1}{K} + M} \tag{2.1}$$

where:

St = Strouhal number;

f = frequency;

L = reference (cavity) length;

U_∞ = average free-stream velocity;

m = integer mode number (the number of vortices);

γ = empirical constant [1] that provides for the phase difference between

i. Upstream arrival of the acoustic wave and the subsequent vortex shedding; and

ii. Downstream interaction with the trailing edge and acoustic wave creation;

K = vortex propagation rate versus the free-stream velocity. When L/D is two, K is approximately two-thirds; and

M = Mach number.

It has been found that Rossiter's equation is valid for Mach numbers ranging from 0.4 to 1.5 for compressible flow [5]. We use the Strouhal Number (St) here in order to establish a reference time (f^{-1}). Steady flow has a residence time (L/U_∞) as a reference constraint since it has no characteristic time of its own [23]. The inverse of the reference time is the characteristic frequency due to the oscillations within the cavity. In calculating the Strouhal Number, from Equation 2.1, we use the velocity of the water, calculated from the pressure gauge, as the average free-stream velocity.

In this experiment, the Mach Number (M) is considered negligible, and using the value for K at L/D = 2 of two-thirds, we can re-write the equation as:

$$St = \frac{fL}{U_\infty} = \frac{2}{3}(m - \gamma) \tag{2.2}$$

There were several limitations identified with Rossiter's model. Heller and Bliss [18] theorized a 'pseudopiston' that accounted for the pressure pulse creation, but this failed to accurately characterize the experimental results [5]. Tam and Block [24] found that Rossiter's model, below Mach 0.4, did not account for either the size and geometry of the cavity, or the shear layer characteristics. The model proposed by Tam and Block, although limited, did predict the amplitude of the oscillations. The usefulness of the

model lies in the accounting for cavity dimensions and shear layer thickness in determining the dominant frequencies and amplitudes of oscillation [5].

Swirl

Gupta [10] has completed many experiments utilizing swirl flows. The non-dimensional variable concerned here is the Swirl Number (S), which is defined as the axial flux of swirl momentum divided by the product of the axial flux of axial momentum and the nozzle radius. The rigorous derivation is provided here for understanding.

$$S = \frac{G_\vartheta}{G_x r_0} \tag{2.3}$$

where:

S = Swirl Number;

G_θ = Axial flux of swirl momentum;

G_x = Axial flux of axial momentum; and

r_0 = nozzle radius (in our case 0.5").

The turbulent terms are included, and noted with an over-bar, as in equations 2.4 and 2.5

$$G_\vartheta = \int_0^{r_0} (\rho uw + \rho\overline{u'w'}) r^2 dr \tag{2.4}$$

and,

$$G_x = \int_0^{r_0} (\rho u^2 + \rho\overline{u'^2} + (p - p_\infty)) r dr \tag{2.5}$$

with *u, v,* and *w* the velocity components in (*x, r,* and θ) cylindrical coordinates. We can use the radial form of the momentum equation and neglect the averaged turbulent terms

$$\overline{u'^2} + (\overline{w'^2} + \overline{v'^2})/2 \tag{2.6}$$

to rewrite the pressure contribution of G_x in terms of *w*,

$$G_x = \int \rho[u^2 + (w^2 - w_{m0}^2)/2] r dr \tag{2.7}$$

when w_{m0} is the swirl velocity at the outer radius r_0. One consequence of neglecting terms here is that the value of S will be calculated and a resulting lack of downstream conservation of the G_θ and G_x momentums [10]. This can be avoided somewhat by assuming solid body rotation plug flow at the nozzle. It is instructive to note that slug flow here is different form that described earlier in Chapter 1, in that we refer to the constant velocity profiles in the axial and tangential directions. In essence the water travels as a solid body, rotated just prior to impacting the inlet orifice. We can then make the substitutions:

$$u = u_{m0} \tag{2.7}$$

and,

$$w = w_{m0} \frac{r}{r_0} \tag{2.8}$$

We get the new form of the flux momentum as:

$$G_\vartheta = \frac{\pi}{2} \rho u_{m0} w_{m0} (r_0^3) \tag{2.9}$$

$$G_x = \frac{\pi}{2} \rho u_{m0}^2 (r_0^2)(1 - (\frac{w_{m0}}{2u_{m0}})^2) \tag{2.10}$$

and putting this back into Equation (2.3) we get:

$$S = \frac{G/2}{1-(G/2)^2} \tag{2.11}$$

where,

$$G = \frac{w_{m0}}{u_{m0}}$$

The flux ratio is defined as the maximum tangential velocity over the average axial velocity. We can utilize a basic assumption in the flow to calculate the Swirl Number with the pressure of water injected into the flow.

As a sample calculation, with 20 psig axially flowing, and 10 psig overpressure in the swirl reservoir, injected tangentially, we would expect a flux ratio of:

$$G = \frac{54.54\,ft/s}{66.97\,ft/s} = 0.814 \tag{2.12}$$

and a swirl number of

$$S = \frac{.4072}{1-(0.4072)^2} = 0.49 \tag{2.13}$$

This is considered a moderate degree of swirl. This form of the equation is used in calculating the Swirl Number and plotting the results, discussed in Chapter Four.

We deal with a wide range of swirl numbers in this experiment (0.21 – 3.5). When we consider a low degree of swirl (S < 0.4), we can reduce the radial momentum equation by neglecting the turbulence terms, to obtain the radial pressure gradient,

$$\frac{\partial p}{\partial r} = \frac{\rho w^2}{r} \tag{2.14}$$

When dealing with weak swirl, (S < 0.2), we can neglect the pressure gradients altogether [10], but that is not our concern here. As swirl velocity decays downstream, it is possible to obtain the axial pressure gradient on the axis. Gutpa [10] goes on to state that weakly swirling boundary layer jet flows retain $\partial p/\partial x$ in their flow direction momentum equation. This property is not contained in non-swirling boundary layer theory and with the tangential injection of flow, we are changing the boundary layer characteristics at the wall if the swirl tube. The low adverse pressure gradient is insufficient to cause axial recirculation, but once the swirl number increases (S > 0.6) there exists a zone of axial recirculation in the form of a Central Toroidal Recirculation Zone (CTRC).

Notwithstanding the previous discussion, which comes from chemically reacting flow analysis, the application here is to the characteristics imparted to the flow in this experiment. The range of swirl numbers here includes those described above. The characteristics we concern ourselves with are those of the swirl number, the radial pressure gradient, and possible recirculation zones generated at the cavity exit.

Helical Modes and Aliasing

Using Equation 2.15 [3], we can extract helical modes as well as the longitudinal modes present in the flow. The radius of the cavity is taken to be the full radius of the cavity chamber section, not that which incorporates the cavity orifices used for calculation of the L/D seen previously,

$$\omega = a_o \left[\left(\frac{j'_{m,n}}{r_c} \right)^2 + \left(\frac{q_z \pi}{L_c} \right)^2 \right]^{\frac{1}{2}} \qquad (2.15)$$

with,

ω = observed frequency in radians/sec (22950 Hz in this apparatus)

a_o = speed of sound in water (4895 ft/s),

$j'_{m,n}$ = 1.84118, root of the zero to the derivative of the Bessel Function [3],

r_c = radius of the cavity (0.75”),

m = azimuthal (helical) mode number,

n = radial mode number,

q_z = longitudinal (axial) mode, and

L_c = cavity length.

We concern ourselves here with only the helical mode portion for an example, thus from Equation (2.15) we extract and utilize,

$$\omega = a_o\left(\frac{j'_{m,n}}{r_c}\right) \tag{2.16}$$

to determine the helical mode frequency. From this frequency analysis, we can find the presence of helical modes through the use of an aliasing formula also presented in Meganathan [3], as:

$$f_{obs} = R_{em} f_{nyq} + B(f_{nyq} - 2R_{em} f_{nyq}) \tag{2.17}$$

with

f_{obs} = observed frequency,

f_{nyq} = sampling rate (4096 Hz),

R_{em} = remainder from the ratio R_1 (below),

$R_1 = \frac{f_{act}}{f_{nyq}}$, broken into integer (Int) and remainder (R_{em}),

$f_{act} = nf_{\text{int}}$, actual frequency expected,

f_{int} = the intended frequency of the mode required, and

B = MOD(Int,2)

In these tests we observed only a small portion of the full frequency spectrum. Aliasing occurs when the frequency of the waveform measured is beyond twice that of the sampling frequency. In these tests the sampling rate, denoted as the Nyquist frequency (f_{nyq}) at 4096 Hz, is insufficient to capture the extremely high frequencies experienced in our tests. We have a calculated frequency of an order of magnitude greater than the sampling frequency, at 22950 Hz. The sampling of the test frequency captures only a portion of the waveform and presents an erroneous reading on the pressure spectrum as an aliased frequency. Using the calculated values for water, through a cavity of 0.75" radius, concerning only the first helical mode, we should experience an aliased frequency of 1626 Hz, based solely on the theory presented here. If there are first helical modes present, the pressure spectrum would indicate a frequency peak at this level. Table 2.1 shows the values utilized to arrive at the expected aliased frequency.

Table 2.1 Table for aliasing value at first helical mode.

f_{int}	22950
n	1
f_{act}	22950
f_{nyq}	4096
R_1	5.603027
Int	5
R_{em}	0.603027
B	1
f_{obs}	1626

Chapter Three

Experimental Approach

Apparatus

The experiments were conducted at the University of Tennessee Space Institute laboratories, Tullahoma Tennessee. The set up constructed similarly to that of Smith [5], with a redesigned exit orifice end to accommodate a greatly reduced length to depth ratio (L/D). Additionally, there was a second configuration set-up for swirl-induced flow, described below. A general schematic of the swirl apparatus is shown in Figure 3-1. The individual parts comprised are listed below:

a. 1.5 inch high pressure water hose;
b. 0.5 inch high pressure water hose;
c. Axial flow inlet gate valve;
d. Tangential flow inlet gate valve;
e. 60 psi gauge (10 psi increments);
f. 60 psi gauge (5 psi increments);
g. Swirl chamber test section;
h. Kistler type 211B5 dynamic pressure transducer;
i. Axial flow injection region;
j. Tangential flow injection;
k. Co-axial cable;
l. Signal conditioner;
m. Co-axial cable
n. National Instruments BNC 2120 board;
o. Computer cable;
p. Computer;

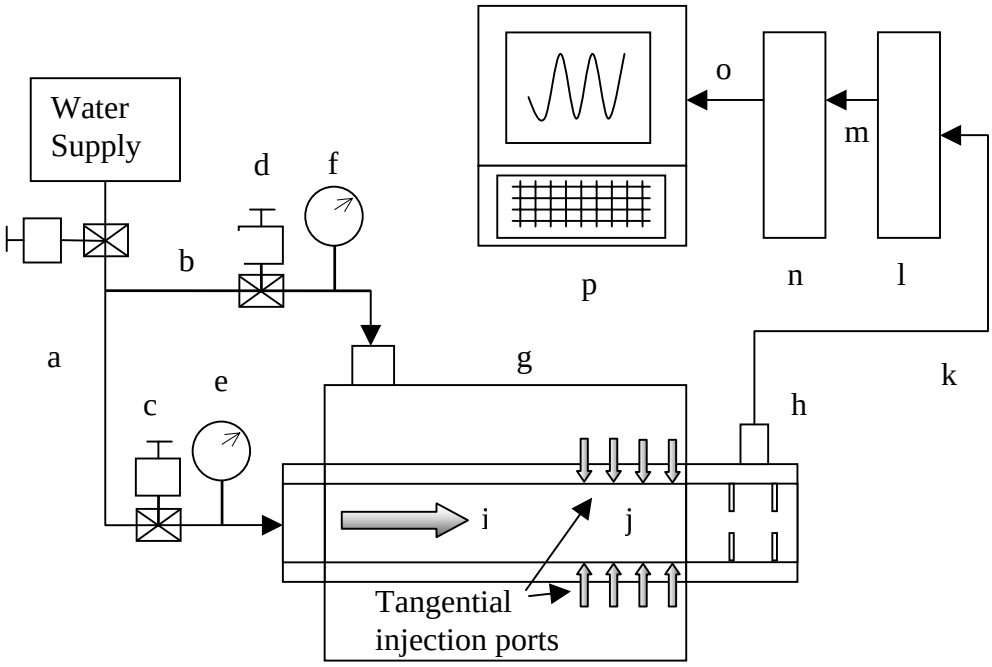

Figure 3.1. Schematic of experimental Swirl Flow Cavity Chamber Apparatus.

The reader is directed to [5] for the significant structures that make up the apparatus for direct cavity flow experimental set-up. The experimental apparatus, constituting the swirl chamber and cavity chamber are constructed as in Figure 3-2. Photos of the internal composition and configuration of the swirl chamber are shown in Figure 3-3 and Figure 3-4. Figure 3.4 shows both the injector ports in the swirl tube and the spacer ring installation. There are four groups of four injector ports each, placed equally around the circumference of the swirl tube.

The minimum travel distance from last injector hole to the cavity was 1 3/8". The thickness of the swirl chamber end cap and the pressure transducer mounting bracket precluded any closer distances. The distance from the inlet orifice to the swirl chamber spacer ring was 3/4". The spacer ring was installed between the swirl tube and cavity chamber adapter to prevent any steps in the flow from adversely affecting the flow development.

Flow Supply

For the axial flow cavity chamber experiments, the flow was supplied exactly as in [5]. For the axial-tangential injection cavity chamber flow, the supply was exact up to the inlet for axial flow shut-off. A three-quarter inch feed, off the one and a half inch line to the axial flow valve, was installed to facilitate flow to the tangential injection swirl chamber. The flow was routed through a valve to the swirl chamber, through a hole drilled in the sleeve. The swirl supply was then fed through sixteen drilled holes tangential to the inner surface of the swirl tube, at the forward end of the swirl tube, shown in Figure 3-4.

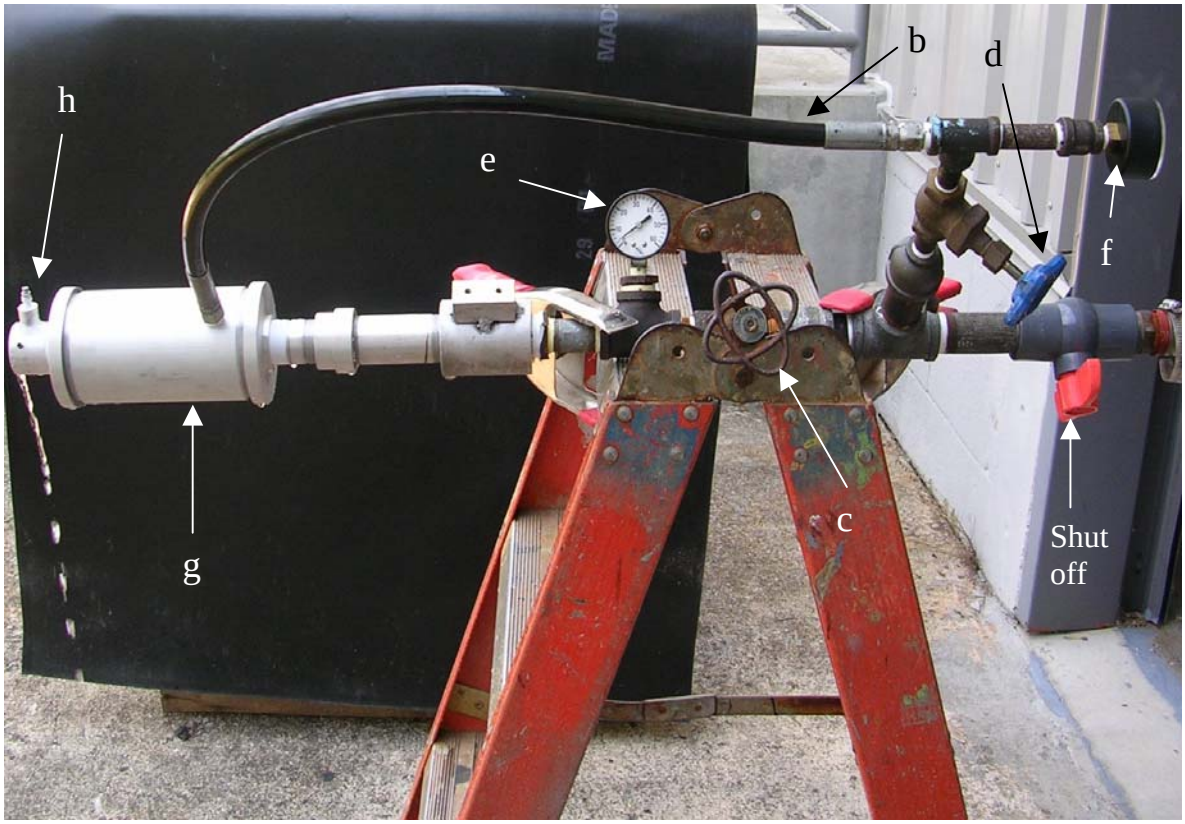

Figure 3.2. Photo of apparatus elements (b) through (h). Background Black provided for contrast only.

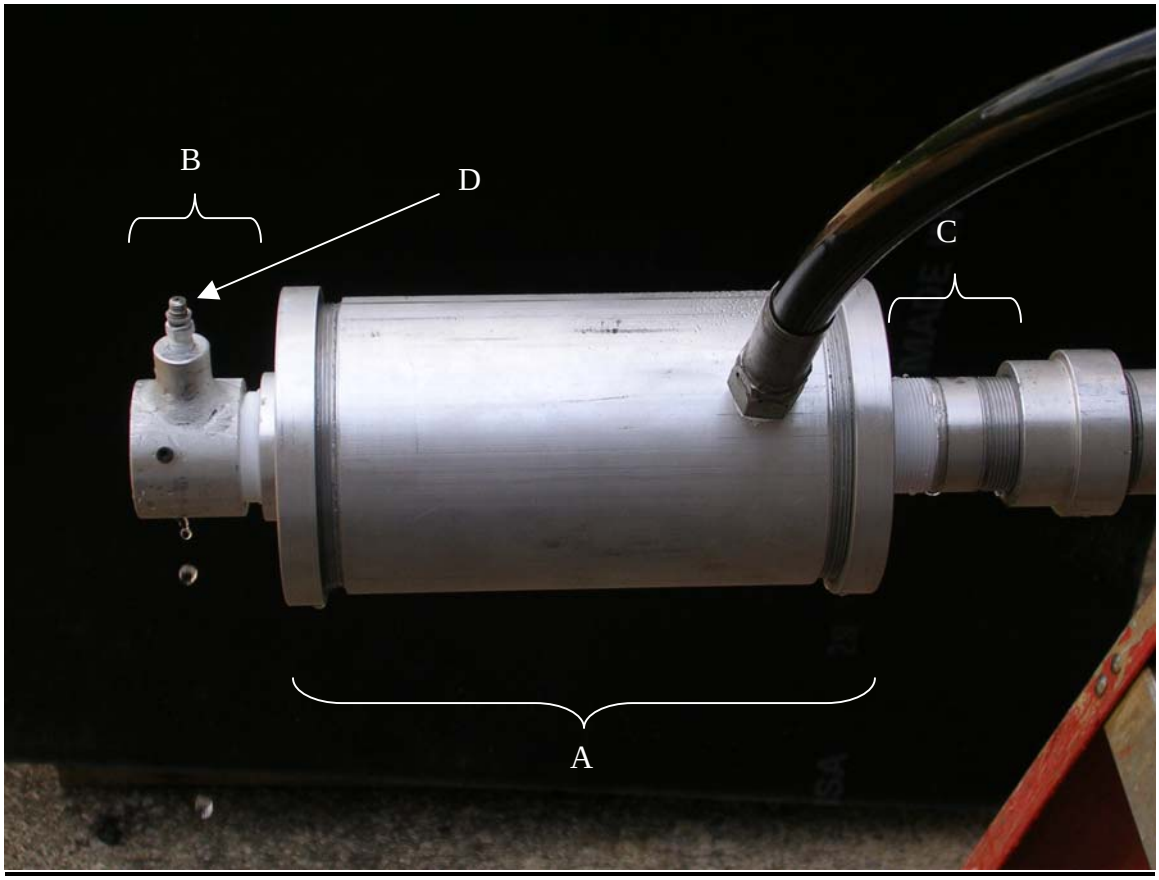

Figure 3.3. Photo of apparatus swirl chamber (A) with cavity chamber (B) attached, 3” mounting adapter (C) and pressure transducer (D) installed.

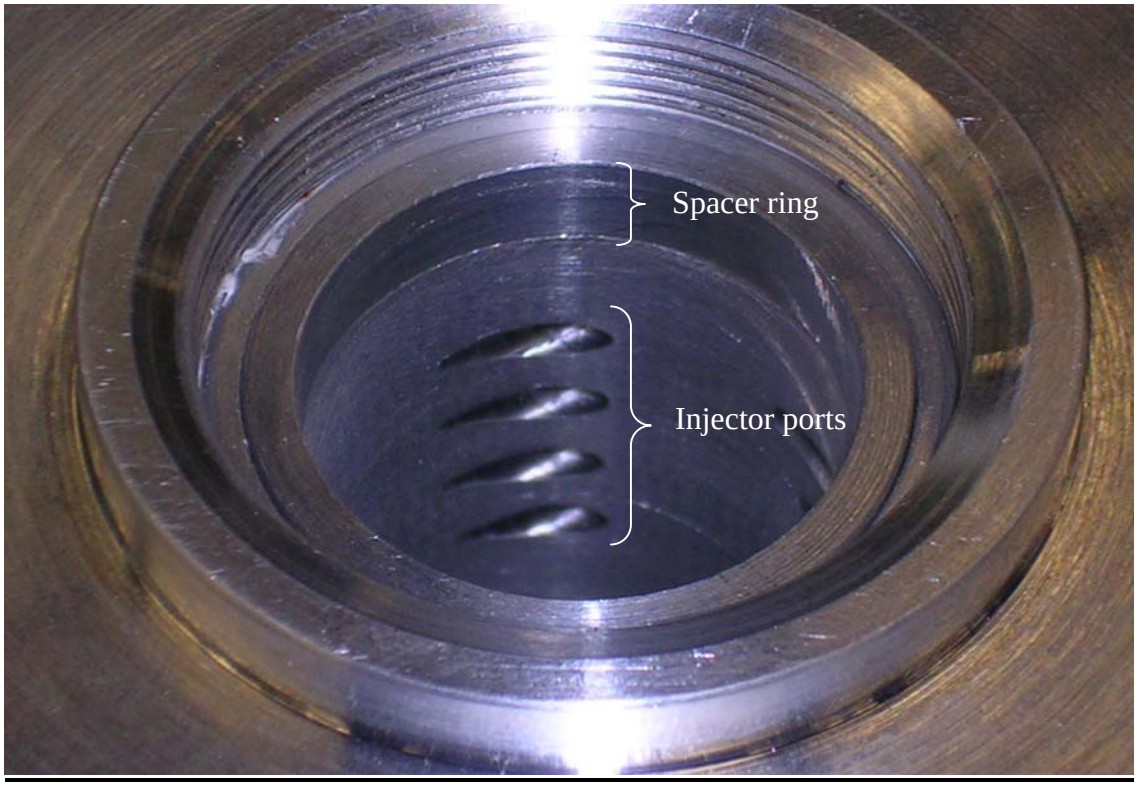

Figure 3.4. Photo of apparatus swirl chamber tangential injection ports. Each port is 1/8” in diameter.

Pressure in the system upstream of the cavity section was determined from a 60 psig pressure gauge placed next to the gate valve, and another placed aft of the tangential injection supply valve. The axial flow was then expanded into a one inch diameter pipe for 7 1/4 inches, which could be considered a short settling chamber prior to entering the cavity test section. The supply to the swirl chamber was fed into the aft portion of the swirl chamber, with an approximately 5” distance to the first tangential injector hole. This allowed for sufficient settling of the flow and prevented the sleeve supply flow from directly entering the injected flow.

Cavity Model

The sketch of the adjustable cavity chamber is presented in Figure 3.5. The cavity was made up of two separate sections that were threaded together; the entry orifice end, and the exit orifice/pressure transducer end. The exit end (Figure 3.6) was threaded onto the supply end (Figure 3.7). The supply end of the apparatus had threading on the outside, and the exit end had threading on the inside at a pitch of twenty threads per inch. The inside diameter (I.D.) of the exit section was 1 5/16” while the outside diameter (O.D.) of the supply end was 1 3/8”. Having this configuration allowed the cavity length (L) to be varied from a minimum of 1/8” up to 2 3/4". An overlap of those lengths explored by Smith [5] was included.

The axial-tangential flow cavity and swirl chamber apparatus was constructed from three components: a supply line adapter, the swirl chamber, and the cavity chamber, as in Figure 3.8.

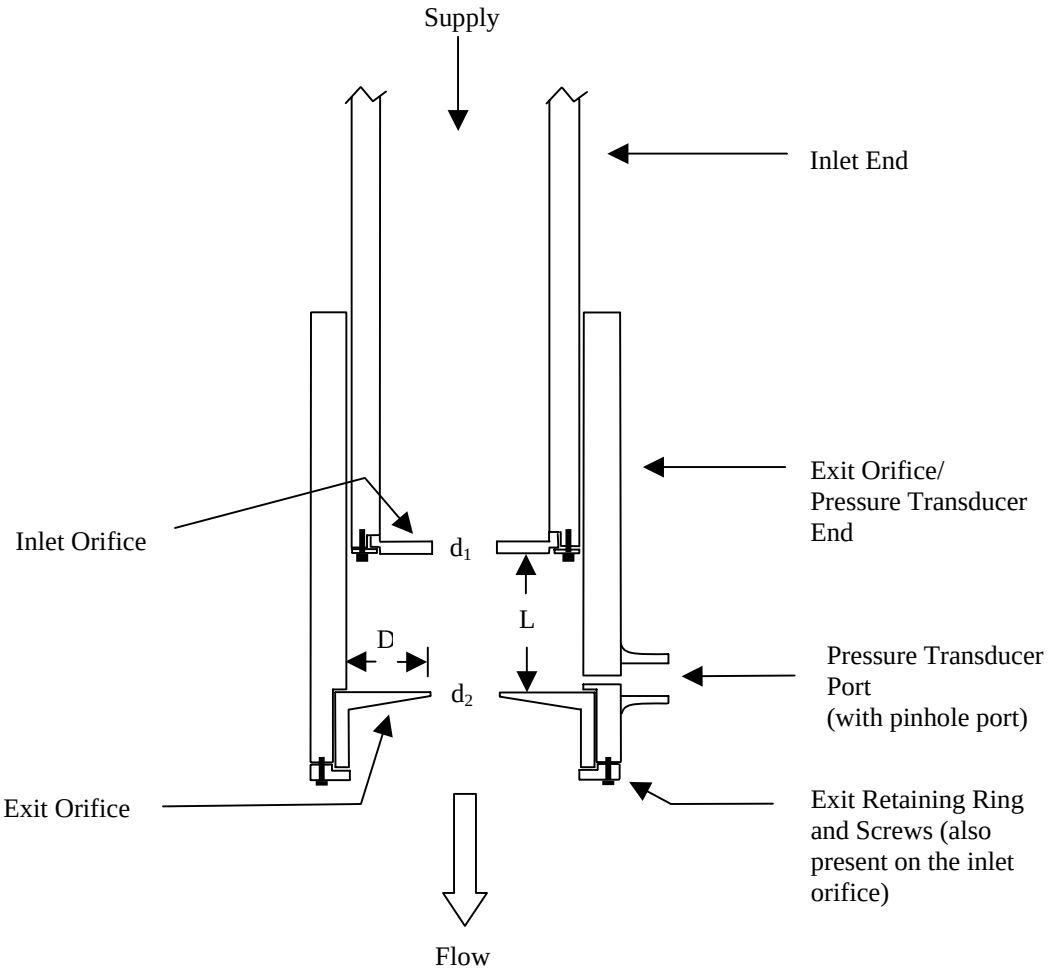

Figure 3.5. Cross sectional sketch of axial cavity depicting the inlet and exit orifices, pressure transducer mount and retaining rings.

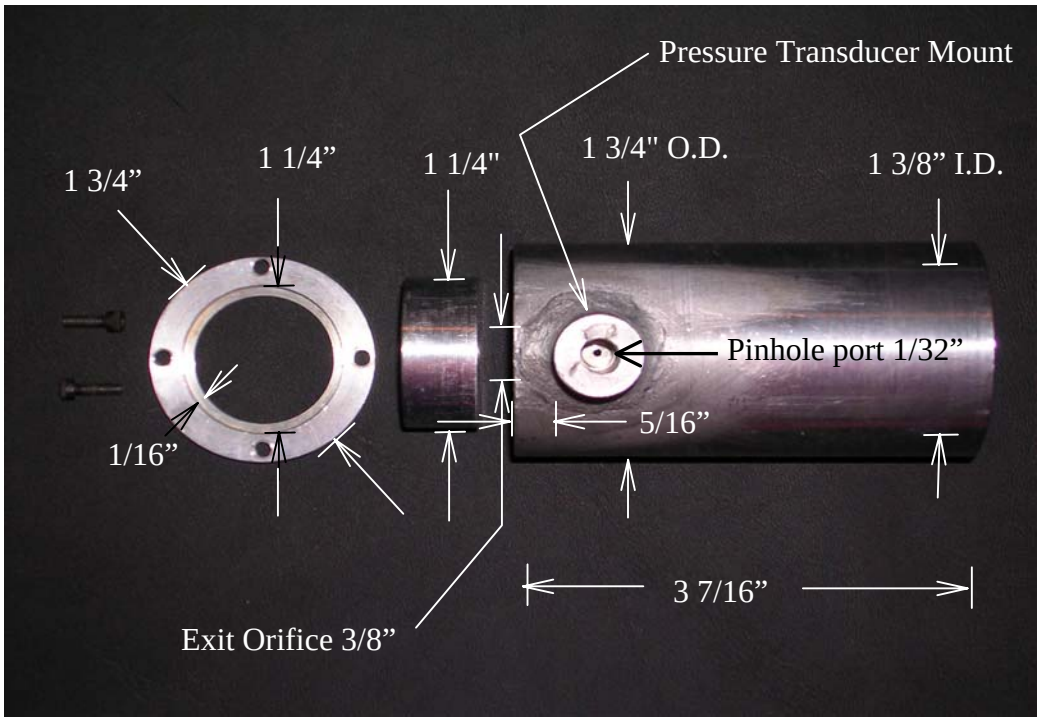

Figure 3.6. Photo of Axial Flow (exit orifice end) apparatus.

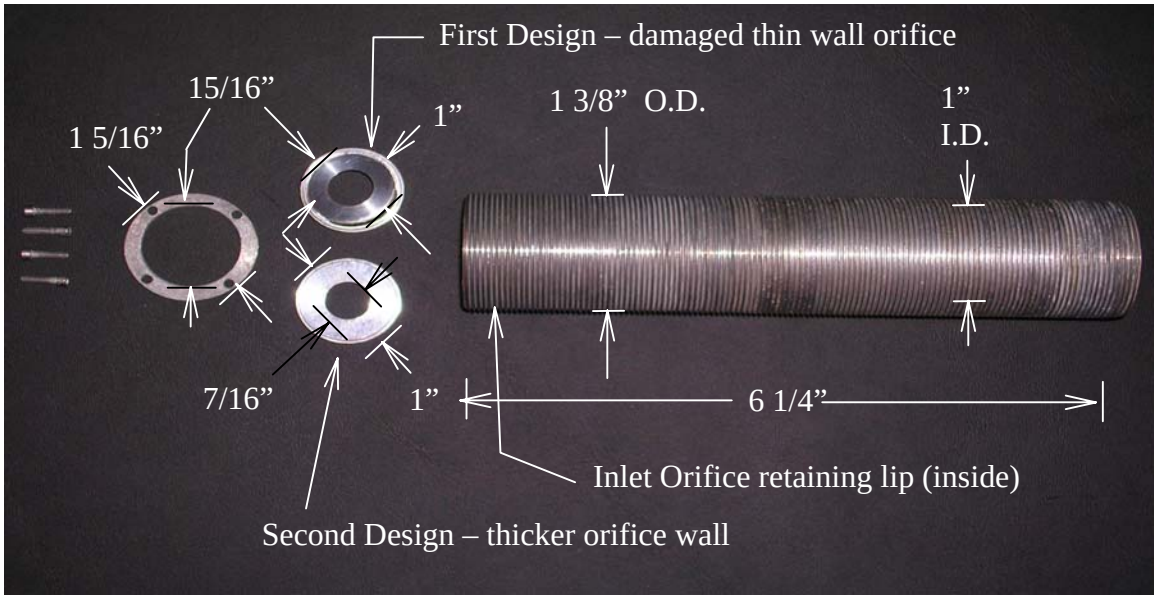

Figure 3.7. Photo of Axial Flow (inlet orifice end) apparatus.

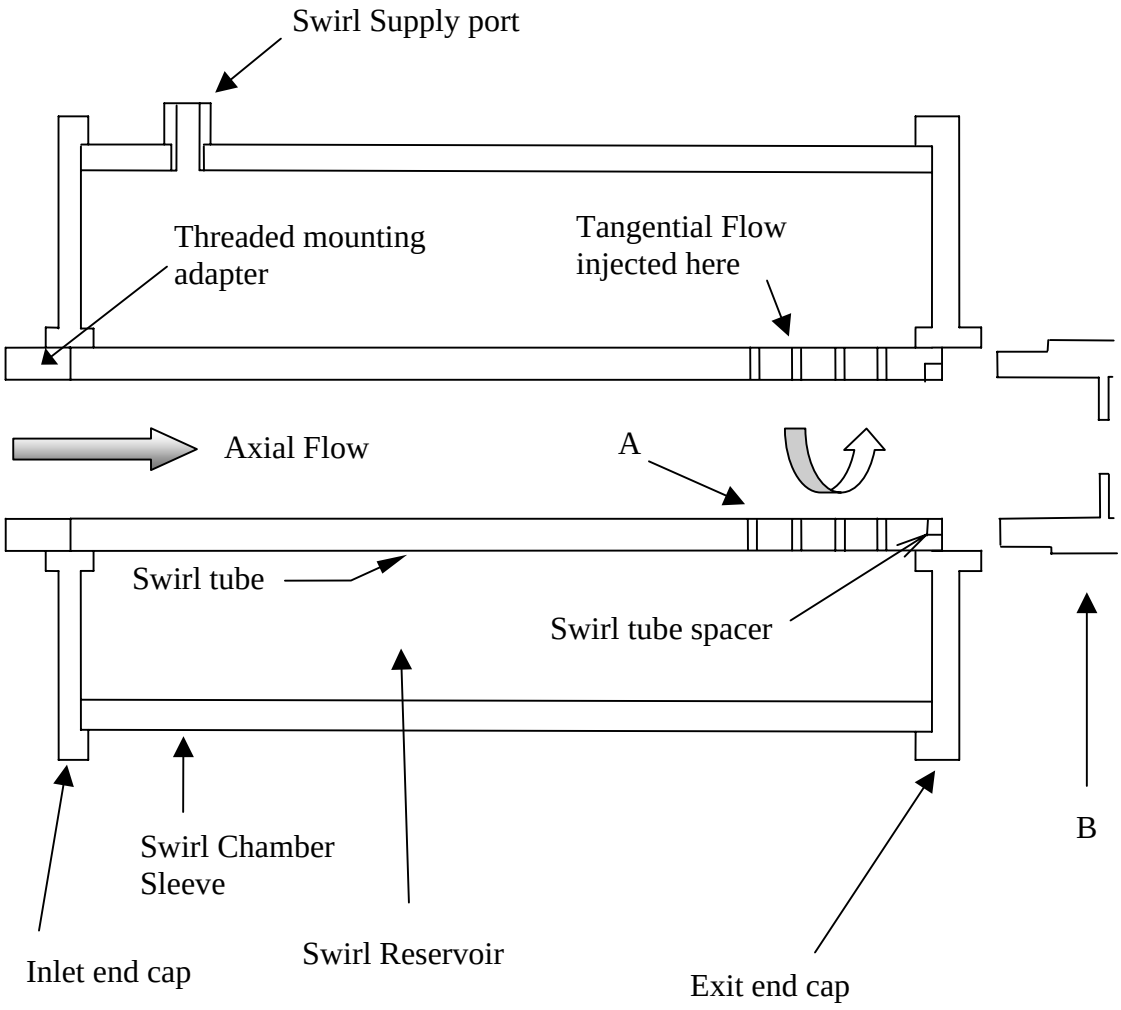

Figure 3.8. Cross Sectional sketch of apparatus swirl chamber and tangential injection ports (A). Cavity Chamber Adapter (B) partially shown on right.

The swirl chamber was threaded onto the supply line with one of two adapters. One adapter measured 3", the other 1". This configuration was required since the swirl chamber supply line was limited in length, a small adapter was employed (1") and the swirl chamber sleeve was reversed to have water fed at the opposite end to the swirl injection ports. A three-quarter inch supply line fed the swirl chamber sleeve, and the cavity chamber/pressure transducer adapter was fixed to the end of the swirl chamber, as in Figure 3.9. All threads along the axial direction are a pitch of twenty threads per inch. This permitted a good resolution of length adjustment for precision L/D control. There was a fixed L/D of 0.9 in the first configuration, with a second cavity chamber exit orifice constructed with a lower L/D of 0.8. These values were determined from axial flow cavity chamber experiments as creating the greatest frequency peaks for the subsequent experimental tests involving tangential flow injection prior to cavity chamber impingement.

The end of each exit end was designed so that an orifice was held in place by four screws and a retaining ring. This allowed the orifice to be removed and replaced with a different diameter or design of orifice. These elements are shown in Figure 3.8. The orifice diameters in this study were:

a. Cavity entrance (d_1) – 7/16"; and
b. Cavity exit (d_2) – 3/8".

These orifice diameters were chosen based upon the research of Meganathan [5]. He discovered that the shear layer interactions were greatest when the cavity exit diameter was slightly smaller than the cavity entrance diameter.

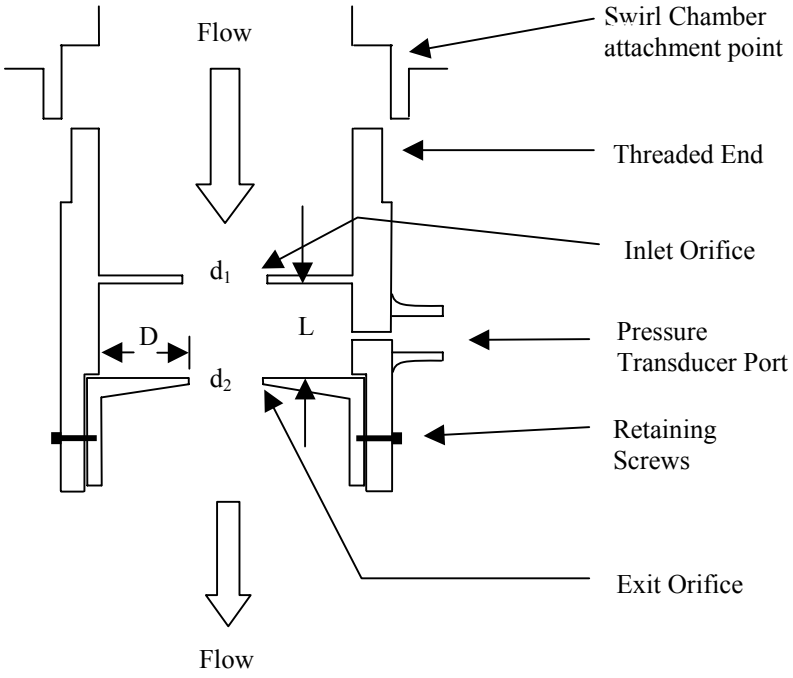

Figure 3.9. Cross Section of Cavity Chamber Adapter. Swirl chamber partially shown above.

Of particular note here is the damage to the original inlet orifice ring. The wall thickness was approximately 0.010", and was torn away from the ring roughly 75% of the circumference of the ring. There was an abrupt ending of the tones generated once the rupture occurred. A further discussion of this incident is included in Chapter Four.

The pressure transducer was positioned into a threaded sleeve in the exit section of the cavity apparatus (see Figure 3.10). There was a small retaining lip (approx. 0.010") within the exit orifice/pressure transducer portion to hold the exit orifice as close to the pinhole pressure port into the pressure transducer as possible, located 9/16" in from the exit end.

A retaining ring was incorporated to maintain the exit orifice in place during the tests. The sensing surface of the pressure transducer was placed approximately 1/4" above the inner surface of the transducer cavity.

In order to establish as small an L/D as possible, it was also necessary to notch the inlet orifice to place the face of the orifice flush with the outside face of the inlet tube. The limiting measurement here was the height of the retaining ring screws, as in Figure 3.11, and the exit orifice retaining lip, Figure 3.10.

Additionally, the pressure transducer was mounted, as in [Smith], but with a pinhole pressure port, see figure 3.9, to accommodate the very small L/D.

Shifting our attention to the swirl chamber apparatus, as in Figure 3.3, the breakdown of the internal components is presented in Figures 3.12 to 3.15.

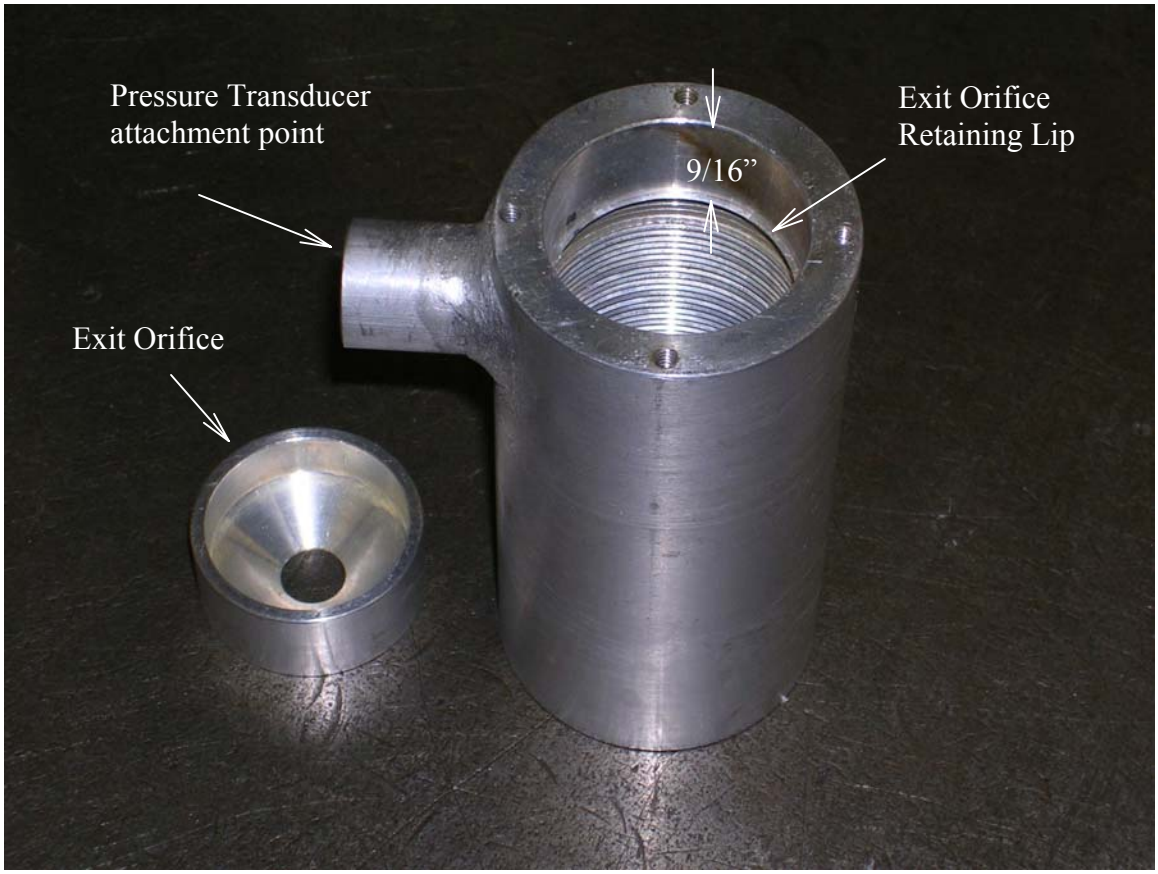

Figure 3.10. Photo of elements that comprise the cavity apparatus (see narrative for dimensions).

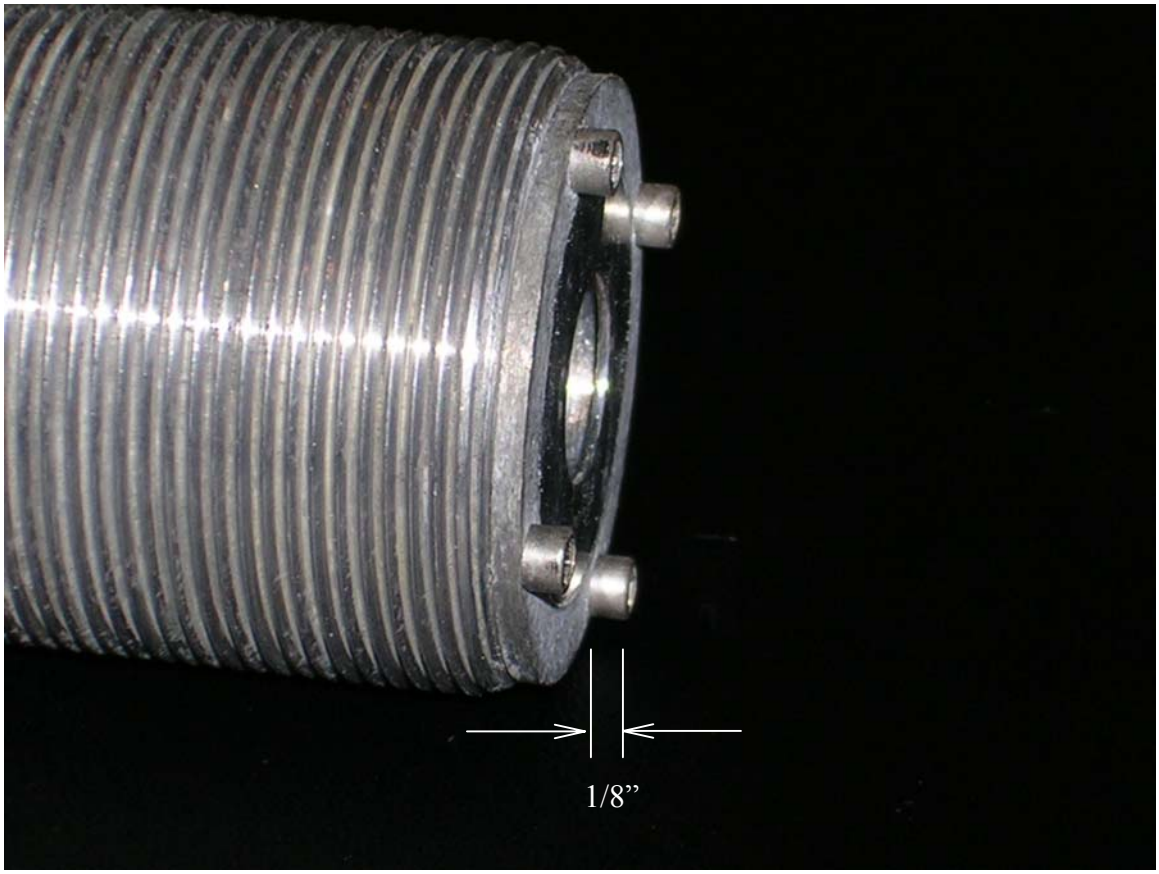

Figure 3.11. Photo of inlet orifice-end flush face mounting.

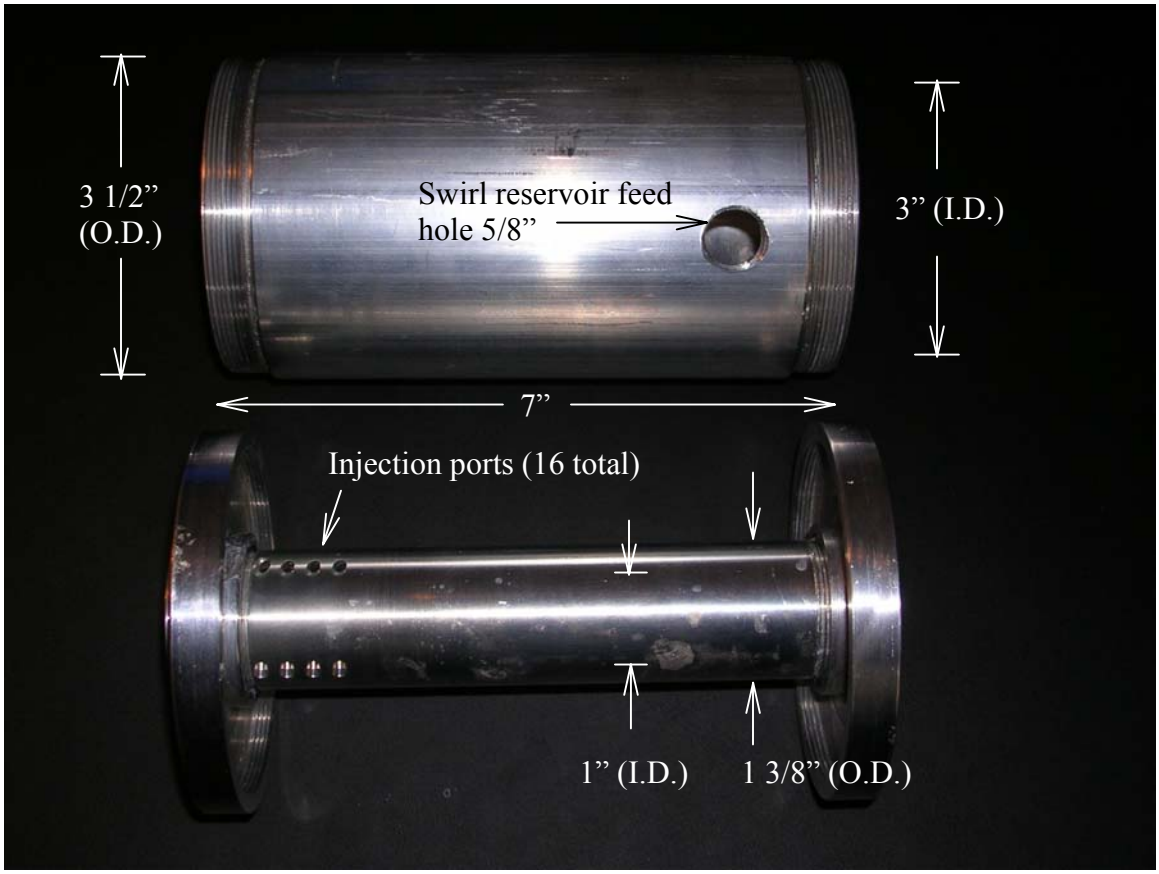

Figure 3.12. Photo of swirl chamber apparatus (breakdown).



Figure 3.13. Photo of swirl tube spacer. Spacer was required for smooth flow. The end of the space protruded beyond the end of the swirl tube to make flush contact with the cavity chamber adapter.

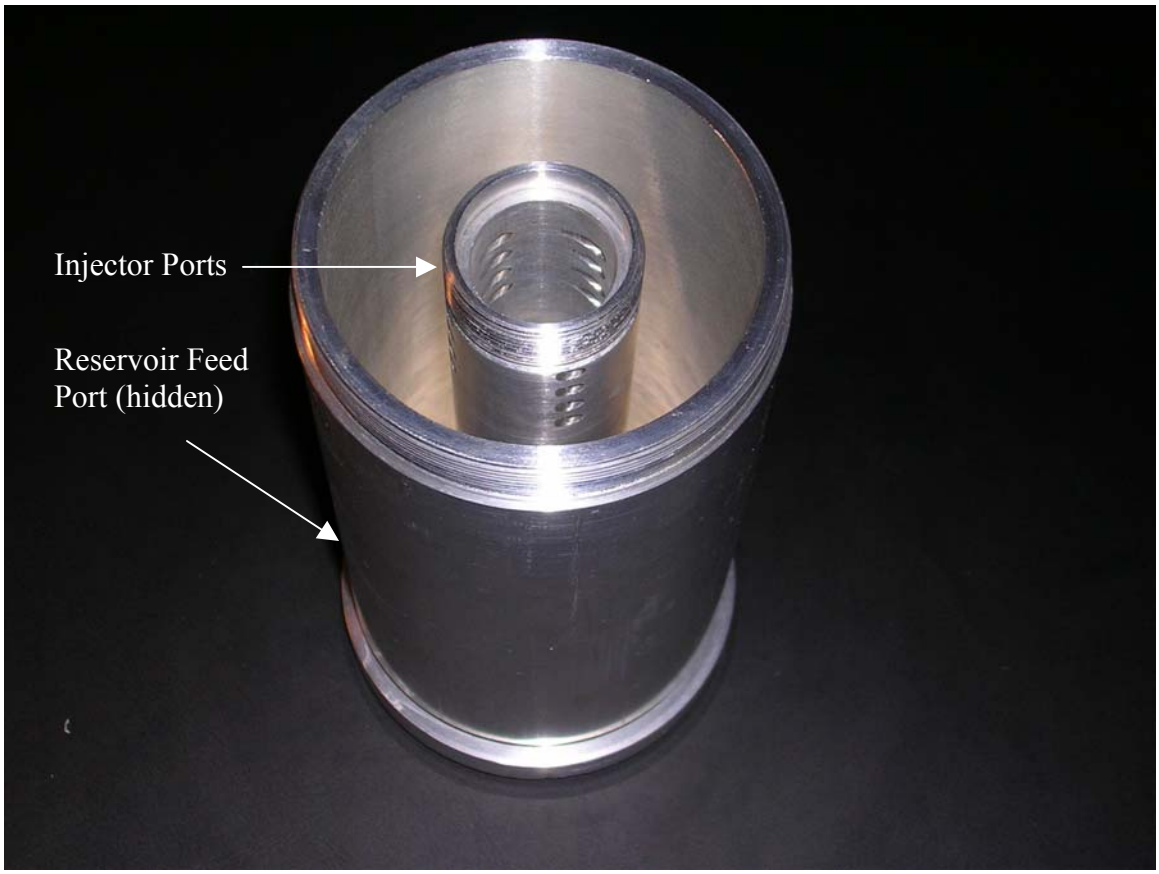

Figure 3.14. Photo of swirl chamber apparatus reservoir and swirl injector ports. Reservoir feed hole at bottom back (hidden from view).

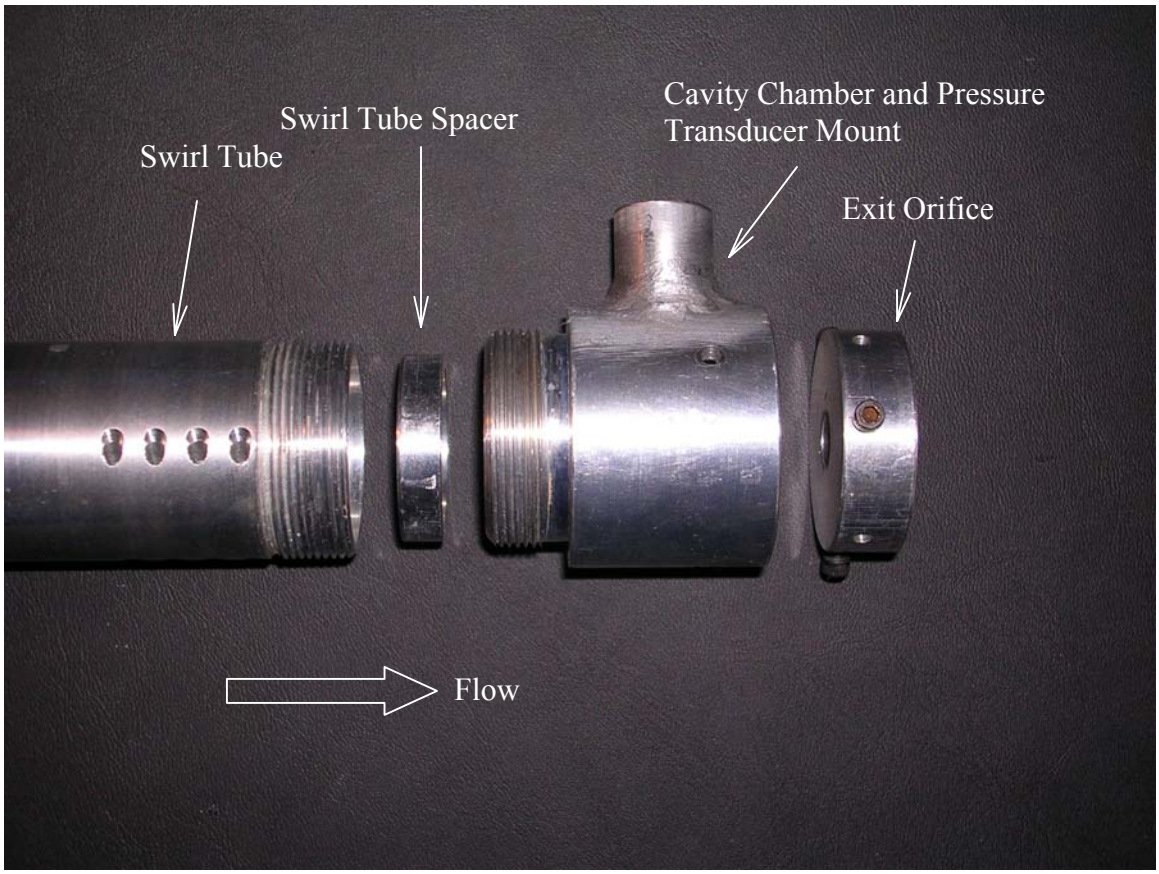

Figure 3.15. Photo of swirl chamber apparatus and cavity chamber (breakdown).

The depth of the cavity was calculated with the equation:

$$D = \frac{I.D. - d_2}{2}, \tag{3.1}$$

where:

D = The cavity depth;

I.D. = The inside diameter of the test section at 1 3/8”; and

d_2 = The diameter of the exit orifice, at 3/8”.

In our case we have $D = 0.5"$.

As in Smith [5], the exit orifice diameter was utilized in calculating the length to depth ratio (L/D). This first configuration of the apparatus was designed so the cavity L/D could be varied easily, below that established by [5], through changing the cavity length (preferred method), the entering or exiting orifice diameters, or both parameters together. The second configuration of the apparatus had a fixed L/D that was established through testing of the first configuration, which resulted in the highest level of peak pressure pulses. It was desirable to establish these high levels and note the resulting affect the swirl had on these values. The creation of baseline peaks with the second configuration was confirmed on two individual cases, and repeated prior to each test run. The effects are displayed, tabulated, and discussed in Chapter 4.

The cavity chamber was constructed with a fixed L/D. Figure 3.16 shows the dimensions used in this experiment.

The two sets of mounting holes for the exit orifice are offset to accommodate an L/D of 0.9 and 0.8 respectively. The values of this L/D would bracket the peak L/D discovered by Smith [5]. There is a 0.015” shoulder milled to bring the exit orifice to the

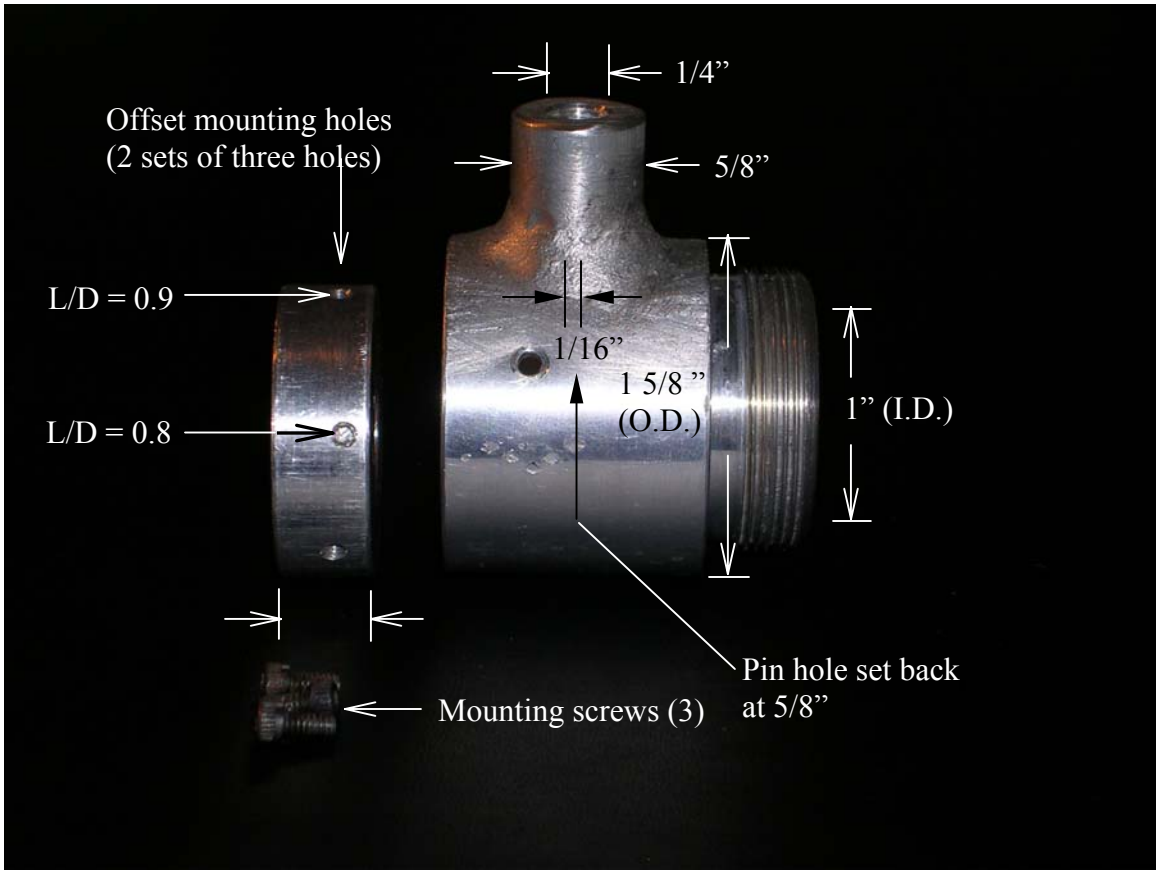

Figure 3.16. Photo of cavity chamber apparatus.

desired L/D, where the mounting holes are used to secure the orifice in place. Figure 3.7 shows the profile of the shoulder design. Data was collected at an L/D = 0.9, then the apparatus was modified to suit the L/D = 0.8. The difference of 0.050" is not considered to affect the tone generation to any extent.

Pressure Transducer

The pressure transducer for this study was selected [Smith] to meet three stringent requirements. In brief, water resistance, fast response time, and size were the key decision factors.

The pressure transducer selected was a Kistler Type 211B5. It was selected to measure fast transient and repetitive dynamic events [22]. It has a quartz compression sensing element, a pressure range of 0 to 100 psi and a sensitivity of 55.08 mV/psi. The threshold of the Kistler 211B5 is 0.001 psi with a hysteresis of 1%. The rise time (10 to 90%) of the transducer is published to be 2 μs [22]. Kistler states that the resonant frequency of this model of pressure transducer is 300 KHz. The rise time and the resonant frequency were deemed not to be a concern for this application, as the frequency range expected was going to be well under 30 KHz.[1] The reader is directed to the general operation and connection of the transducer as covered in [Smith].

Two key points required to note here are the high sampling rate of 333 kilosamples per second and that the pressure transducer arrived from the manufacturer dynamically calibrated, so no calibration was required prior to the testing.

[1]Smith, J.D.B., "An Experimental Study of Axisymmetric of Cavity Oscillations in Low Speed Incompressible Flow," M.Sc Thesis, University of Tennessee, December 2000.

Computer Signal Processing

LabVIEW (version 6.0) was the software used in order to obtain usable information from the pressure transducer data. The programme created in LabVIEW allowed the frequency spectrum and amplitude to be displayed on the PC monitor screen (Figure 3.17). The parameters of the LabVIEW programme were set so that any quarter second interval could be saved as raw data. Later the raw data could be imported into Microsoft Excel to reproduce the graphs from LabVIEW. Examples of typical data graphs will be discussed in Chapter 4.

Similarly to Smith [5], the computer was set up so that the scan rate was 8192 samples in a second. This gave a total bandwidth (folding frequency) for the spectrum of 4096 Hertz. The number of scans to acquire was 2048, and the system did this at one time. Therefore, a cycle took a quarter second. While the number of samples used may seem like odd numbers, they are purposeful. The numbers are powers of 2^n, which allowed the computer to take readings at even intervals and perform Fourier Transforms. No averaging mode was employed during the tests.

There are half as many points in the frequency spectra figures as the number of scans made by the pressure transducer during a cycle. Therefore, there are 1024 points on each frequency spectra graph. The system was configured so that the level of amplitude resolution was greater than 0.003 psi and a minimum frequency resolution of 4 Hz.



Figure 3.17 Photo of LabVIEW screen. Parameters are L/D = 0.9 and pressure gauge reading 10 psi. Note peaks at 750 Hz, 1500 Hz, and 2250 Hz, and smooth oscillation of frequency amplitude (top graph).

Calibration of Experimental Apparatus

The entrance and exit orifice sizes were kept constant during the tests. The length of the cavity was varied in order to change the length to depth ratio. Investigations of L/D ratios were conducted below those established by Smith [5]. The data collected in [5] were used to establish validity of the current apparatus tests. The second configuration of the apparatus maintained a constant depth and length, with highest peak values of pressure pulses created for baseline measurements and comparison when swirl was injected into the flow.

The baseline jet (single exit orifice) established by [5] was utilized. An additional baseline was generated on two separate occasions, as well as prior to each test run. For this test, the axial pressure was varied through nine different values, stepped at 5 psig intervals, and recorded. Additionally, the tangential flow baseline was recorded, with the same nine values of pressure injected without any axial flow. These tables and graphs are discussed in Chapter 4.

The pressure transducer was mounted above a pinhole pressure port to the cavity, located as close to the exit orifice as possible. Lengths generated from 0.125" through 0.7" were recorded, in full and half-turn increments. This allows L/D ratios of 0.25 to 1.4 to be explored. Notwithstanding, the initial configuration was created to explore these lower L/D's, with the intent that the range of L/D for the swirl configuration would lie between 0.8 and 0.9. Several L/D were plotted between these values and are included in Chapter 4 discussion.

Each length and pressure combination was repeated several times and used to evaluate the results. In the second configuration, axial flow and tangential injection were

varied repeatedly and recorded to see the effect on the flow and tones generated. The flow pressure was established axially first, with the pressure noted on the axial flow and tangential flow gauges. The tangential injected pressure was increased through the swirl chamber feed valve, with the additional pressure being added to that value displayed on the tangential flow gauge (see Figure 3.2 item (e) and (f)). As an example, the pressure established for Figure 3.18 was initiated axially at 20 psig (Axial = 20 psi), and then 5 psig (Tangential = 5 psi) was added to the tangential flow. Major peaks were recorded and plotted for further analysis in Chapter 4.

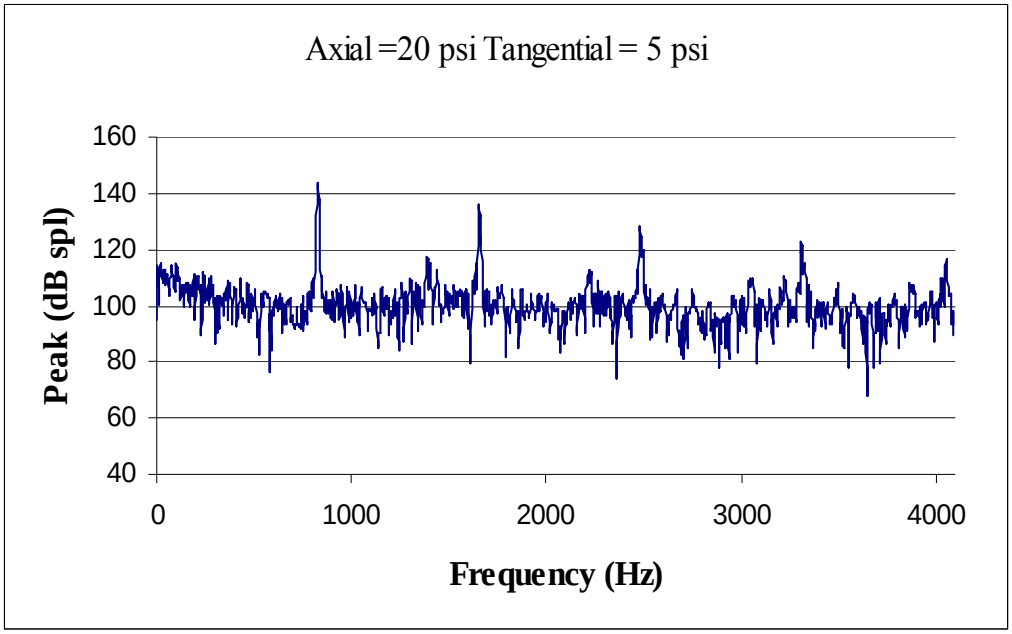

Figure 3.18. Chart with axial and tangential flow components.

Chapter Four

Experimental Results and Discussion

Basic Parameters

There are four scaled parameters utilized to describe the flow in these experiments. The primary parameters were length to depth ratio (L/D), Swirl Number (S), the Reynolds Number (Re), and the Strouhal Number (St). The depth of the cavity was fixed, thus the length was varied in the experiment to obtain an optimum resonant frequency resulting within the cavity. The thread pitch precision of 20 threads per inch resulted in a negligible error in L/D, discussed below.

The derivation of the Swirl Number, completed in chapter two, left us with,

$$S = \frac{(G/2)}{(1-(G/2)^2} \tag{4.1}$$

where,

$$G = \frac{w_{m0}}{u_{m0}} \tag{4.2}$$

with w_{m0} and u_{m0} representing the tangential injection and axial velocities respectively. This allowed us to calculate the swirl number through the use of the velocity components within the apparatus based on the pressure gauge readings.

The scaled parameters allows for a more appropriate comparison of the results. The parameter utilized here was the Strouhal Number, defined as,

$$St = \frac{fL}{V} \tag{4.3}$$

where we have,

V = average velocity of the baseline jet flow, as measured by the pressure gauges,

f = frequency of the oscillations created within the cavity,

L = characteristic length of the cavity.

We also utilize the Reynolds Number, but here we have based it on cavity length (Re_L) as,

$$\mathrm{Re}_L = \frac{\rho V L_c}{\mu} \tag{4.4}$$

A third parameter was the velocity of the flow used in calculating the remainder of the flow characteristics. The velocity was calculated using the Bernoulli equation [23] and the pressure readings from the flow gauges,

$$p_t = p_s + \frac{1}{2}\rho U_\infty^2 \tag{4.5}$$

and replacing U_∞ with U, as the average velocity of the baseline jet flow, rearranging to solve for U, we obtain,

$$U = \sqrt{\frac{2}{\rho}\left(P_t - P_s\right)} \tag{4.6}$$

where we have:

U = average velocity for the baseline jet, but used on all cavity lengths;

ρ = density of water;

P_t = total pressure of the water; and

P_s = static pressure of the water

It must be kept in mind that the static pressure remained constant and the total pressure difference $(p_t - p_s)$ was the pressure measured on the gauge (psig). Table 4.1 contains the pressure readings and resultant velocities used in these experiments.

For the tangential injection, similar calculations were used. The pressure difference here was measured between the axial flow and the tangentially injected flow on the more precise gauge at the tangential injector valve. The pressure was initiated with the axial flow valve, and then the additional pressure was injected through the tangential injector valve. To minimize the error due to back-pressure, the pressure readings were recorded as the difference before and after opening the tangential injector valve only, after the axial flow was established and stabilized.

Table 4.2 contains sample values of the swirl number (S). Included in Table 4.2 are the values of the flux momentum calculated from the axial and tangential pressure readings, which were in turn used to calculate the Swirl Number.

Table 4.1. Average Velocity calculations based on gauge pressure readings.

Gauge Pressure (psig)	Average Velocity (ft/s)
48	84.46
45	81.81
40	77.13
35	72.15
30	66.79
25	60.97
20	54.54
15	47.23
10	38.56
5	27.27

Table 4.2. Table of flux momentum (G) and Swirl Number (S) based on pressure readings at tangential injector valve. Tangential pressure is additional pressure difference above the established axial pressure.

Pressure (psig)		Calculations	
Axial	Tangential	G	S
30	0	0.00	0.00
30	5	0.41	0.21
30	10	0.58	0.31
30	15	0.71	0.40
30	15	0.71	0.40
30	20	0.82	0.49
30	5	0.41	0.21
30	5	0.41	0.21
30	10	0.58	0.31
30	10	0.58	0.31

Additionally, the Strouhal Number (St) was calculated using the frequency peaks generated within the cavity. Table 4.3 contains the values that were generated through these experiments, with peak measured in dB of sound pressure level (spl). Not all levels and ranges of pressures are included in the table for brevity. It is instructive to note the values of the Strouhal numbers over a range of velocities.

It should be noted that these values are representative of only one axial pressure exploited in these tests. Values range from those established in Table 4.1. It is evident that there is a wide range of Strouhal Numbers evident in this test, representative of the wide range of frequencies experienced.

Table 4.3. Table of Strouhal Numbers (St) based on total velocity and frequency peak measured. Pressure readings taken at the tangential injector valve.

Pressure (psig)		Total Pressure (psig)	Measured Values			
Axial	Tangential		Velocity (ft/s)	Peak (dB spl)	Freq (Hz)	St
30	0	30	66.79	140.20	896.20	0.503
30	5	35	72.15	141.00	972.20	0.505
30	15	45	81.81	126.84	124.00	0.057
30	20	50	86.23	141.38	1072.20	0.466
30	5	35	72.15	120.70	1848.30	0.961
30	5	35	72.15	116.10	40.00	0.021
30	10	40	77.13	141.10	864.14	0.420
30	10	40	77.13	117.60	44.00	0.021

Sources of Error

A concerted effort was made to minimize the sources of error in this experiment. The possible sources of error encountered in these experiments are detailed below.

In conducting the tests in this study, the construction of the apparatus created several modes of potential error. The axial flow apparatus was utilized [5] with a modified inlet orifice to obtain as small a length as possible. One source of error here is the length of the retaining lip within the cavity chamber was not an exact figure. An approximate value was used in the L/D calculations. A second source of error was the construction and positioning of the pinhole port below the pressure transducer. Its location within the cavity chamber was as far forward as practical, yet the small diameter of the hole may have had an attenuating effect on the tone peak reading. The pressure

and frequency errors are utilized as in Smith [5], with frequency error approximately 1% and decibel sound pressure level (dB spl) at 2%.

The pitch on the threads used in these tests was set at 20 threads per inch. Effort was made to ensure the establishment of the L/D was as close to the required value as possible. The current pitch presented a negligible error in this regard, as previously established [5].

Considering the Swirl and Axial flow apparatus, the general construction was such that an hermetic seal was virtually impossible when it was required that the chamber be assembled and re-assembled several times to change the swirl and cavity chamber configuration. The water seal was also minimal, resulting in a loss of pressure and resulting mass flow through the apparatus. Pressure readings were taken as though there were no pressure losses through the apparatus.

When taking the pressure readings, there were two gauges that provided the greatest cause of error. The first gauge, measuring the axial flow, was graded into 10 psi increments with a one inch inlet, and the fluctuation of pressure ranged to a maximum of approximately +/- 5 psig. The tangential flow gauge was graded into 5 psi increments and, coupled with a smaller diameter inlet, maximum pressure fluctuations were seen at only +/- 2 psig. In taking the readings, the experimental method contributed to error through setting the valve reading as close to the center of the required reading as possible. The pressure was seen to fluctuate to a maximum of that stated, with some days the pressure fluctuated very little. The ability of the pressure to be maintained at a constant setting was more of a nuisance, with repeated adjustments being required. The unsteadiness was minimized through repeated testing and recording of pressure peaks.

Notwithstanding the above discussion, the extrapolation of Rossiter's constant (γ) [1] recreated in Table 4.4, also resulted in some error in the calculations. An Excel® spreadsheet was utilized to discover that constant at lower L/D. When extrapolating, the use of a linear and second order trend line created two sets of equations used to calculate the value of Rossiter's empirical constant. (see Figure 4.1).

Below, Table 4.5 shows the values used and the corresponding extrapolation. The linear extrapolation was extended to zero and used consistently throughout the remainder of this study.

Contained within Table 4.5 are the values of the percent error in the Strouhal Number (St), which is our preferred goal. As the reader can see, we are dealing with an extremely low value of error, particularly at the range of L/D used in this experiment. The values of L/D are at or below 1.0. For this reason, we can safely use the linear extrapolation to determine the Rossiter Constant for the remainder of the tests.

Table 4.4 Rossiter's Empirical Constant (γ)

L/D	(γ)
4	0.25
6	0.38
8	0.54
10	0.58

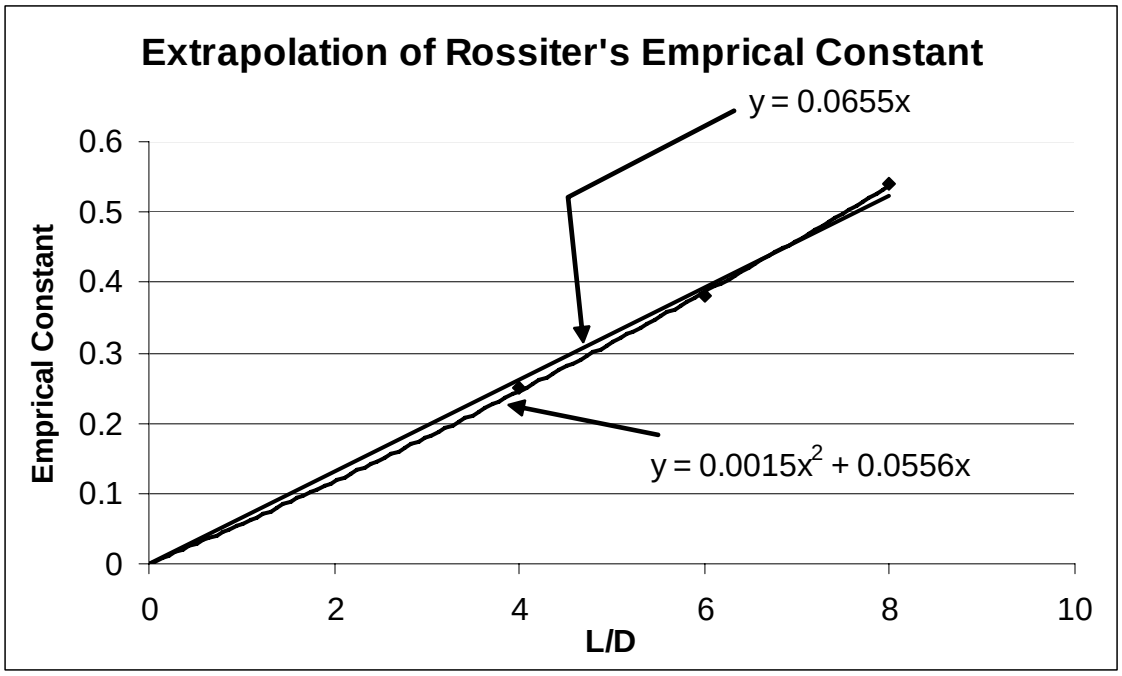

Figure 4.1. Extrapolation of Rossiter's Empirical Constant

Table 4.5. Extrapolation of Rossiter's Empirical Constant

Extrapolation				
L/D	Linear	2nd Order	Error (%)	
			(γ)	St
0.2	0.0131	0.0113	14.05	0.186
0.8	0.0524	0.0458	12.67	0.696
0.9	0.0590	0.0516	12.55	0.774
1.0	0.0655	0.0575	12.21	0.849
8.0	0.5240	0.5440	3.68	4.2

There were several peaks recorded during testing that were not considered as modes for consideration. Within the cavity, the frequencies recorded were those that excited or were coupled with other frequencies, as discussed in Meganathan [4], where three Rossiter Modes (f_1, f_2, and f_3) present resulted in the relationship,

$$f_3 - (f_1 + f_2) = \Delta f \cong 0 \tag{4.7}$$

These peaks were not considered for analysis, although they have been included for clarity and validation of the results and discussion. Additionally, the sampling rate of the test apparatus was below that set for calibration of the pressure transducer. Frequencies higher than the sampling rate could not detect the presence of higher frequencies of the Rossiter Modes. The sampling rate was established at 4096 samples per second. Any frequency above this value would not be recorded accurately.

Although temperature measurements of the water were not critically measured in these tests, the outside air temperature was recorded at the beginning of each of the test runs. The temperature during the tests experienced ranged from 40 to 95 degrees Fahrenheit. This temperature range may have contributed to some fluctuation in tones experienced. Further study of the effects temperature has on the flow is recommended.

Baseline Measurements

The baseline measurements utilized for the axial flow experiments were those used in Smith [5], since the same Kistler® pressure transducer was utilized [27, 28]. Although that transducer was later replaced with a second transducer, of the same manufacture and specification, the data acquisition file in LABView® was modified to

reflect the changes in response specifications to ensure a smooth transition. See Table 4.6 for specifications.

Figures 4.2 through 4.4 contain the baseline power spectrum of that for axial flow only. The axial velocities are listed with the corresponding graph (L/D = 0.9).

Figures 4.5 through 4.7 contain the power spectrum of the baseline tangential flow. Again, the cavity was fixed at L/D = 0.9. Here the tangentially injected flow was measured without any axial flow.

The number and level of the peak pressure pulses should be noted in particular. Several plots contain a single peak while others contain several across the spectrum. In these cases, the highest peak pressure is referred to as the primary peak.

The reader is directed to note the shift in the primary peak to the right with an increase in velocity. Even though the peaks move to the right, there exist several peaks that become the primary peak with higher velocity. The shift form a lower frequency to a higher is referred to as mode jumping (Mode 1 – bottom of Figure 4.3 and Mode 2 – top of Figure 4.4). In this particular case, the flow velocity was maintained at 66.79 ft/s and the mode shifted randomly during the tests. This effect was experienced several times throughout the testing at other velocities, both with and without swirl.

Table 4.6. Table of specification differences between transducers.

Specification	Transducer 1	Transducer 2
Response	55.09 mV/psi	49.69 mV/psi
Response	0.002769 psi/bit	0.003071psi/bit
Cal Factor	18.152	20.125

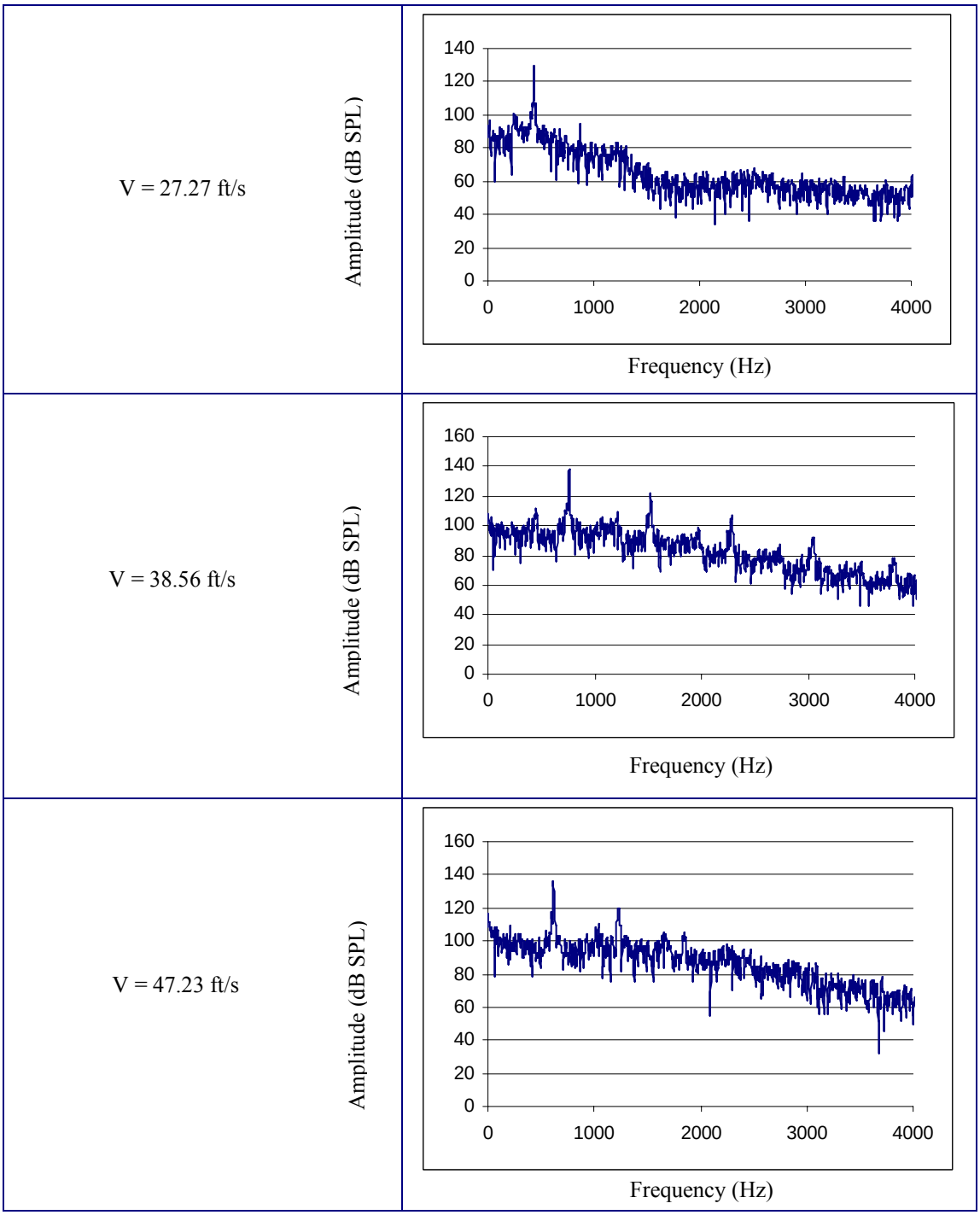

Figure 4.2. Plot 1 of Axial Baseline Frequency Response with flow at indicated velocities.

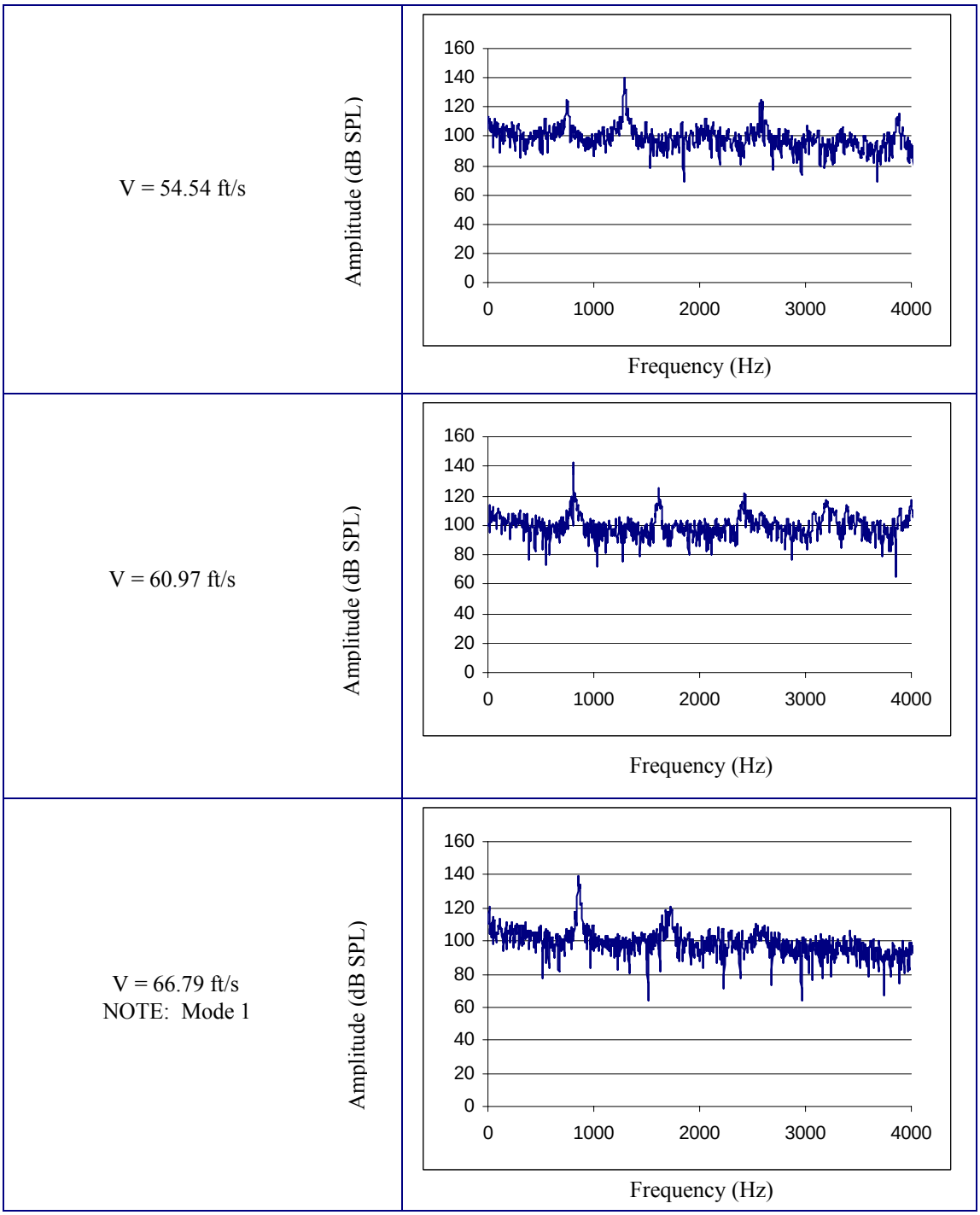

Figure 4.3. Plot 2 of Axial Baseline Frequency Response with flow at indicated velocities.

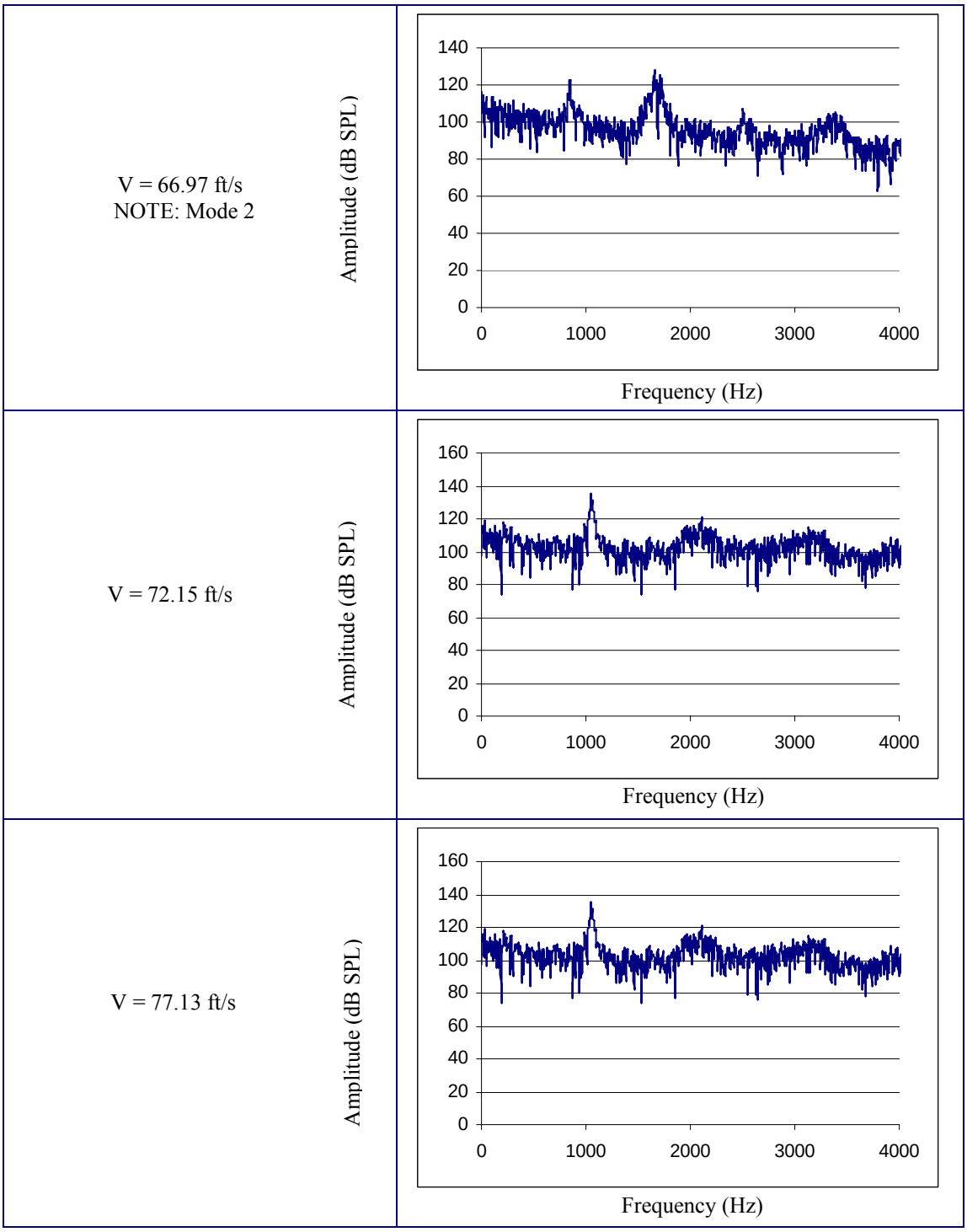

Figure 4.4. Plot 3 of Axial Baseline Frequency Response with flow at indicated velocities.

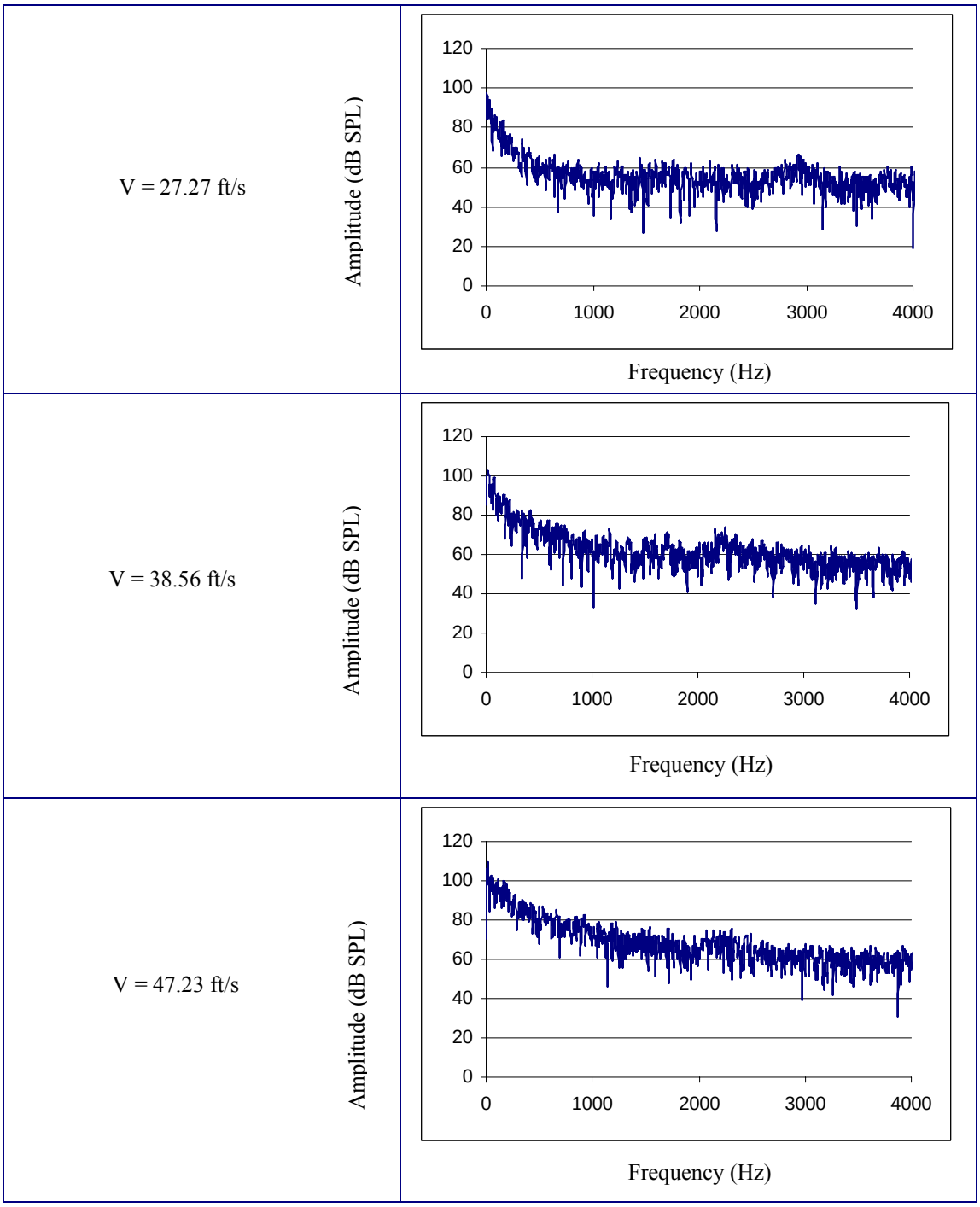

Figure 4.5. Plot 1 of Tangential Baseline Frequency Response with flow at indicated velocities.

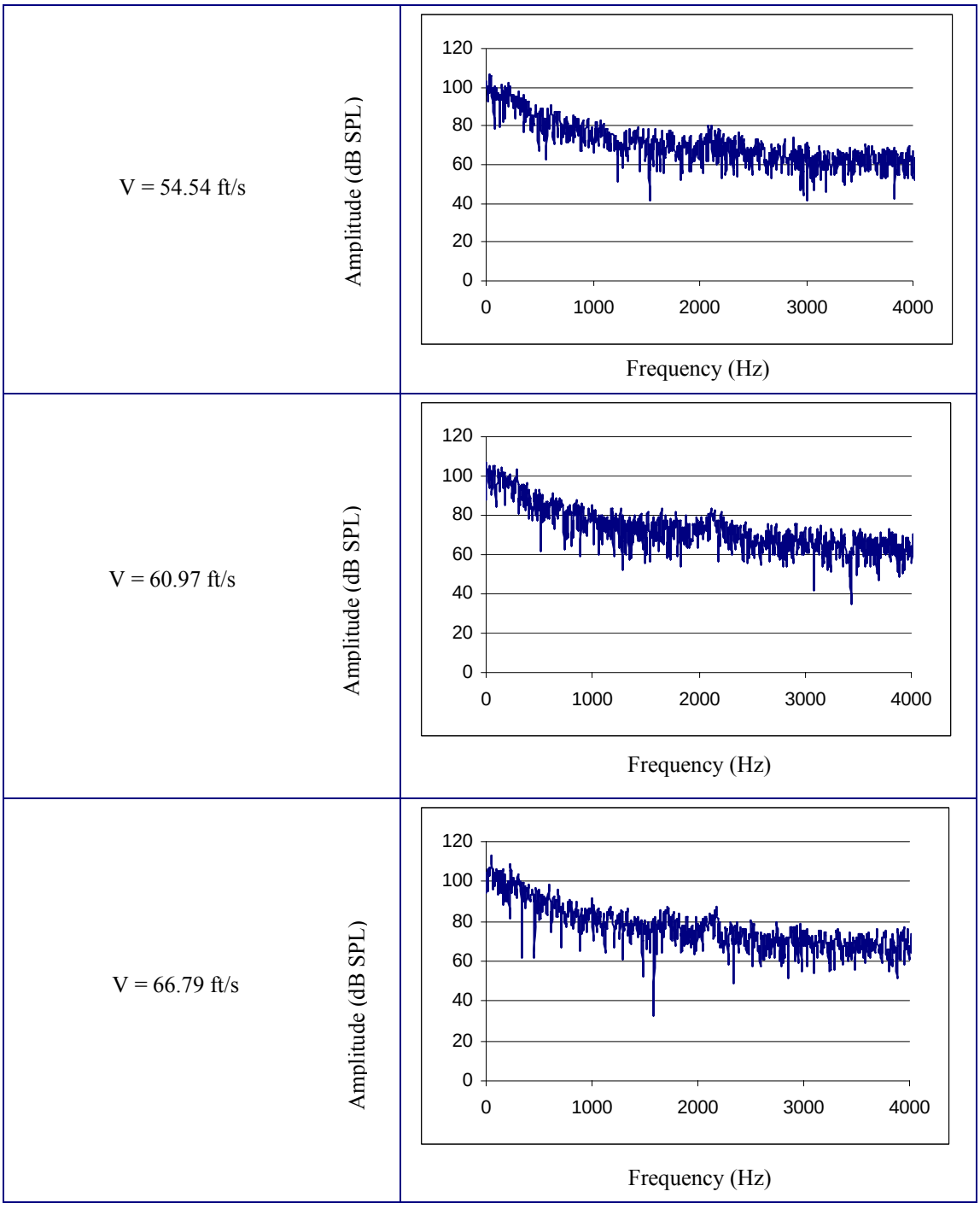

Figure 4.6. Plot 2 of Tangential Baseline Frequency Response with flow at indicated velocities.

V = 72.15 ft/s	Amplitude (dB SPL)	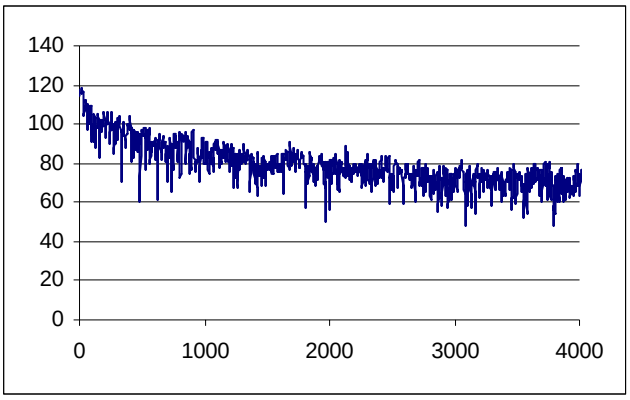
V = 81.81 ft/s	Amplitude (dB SPL)	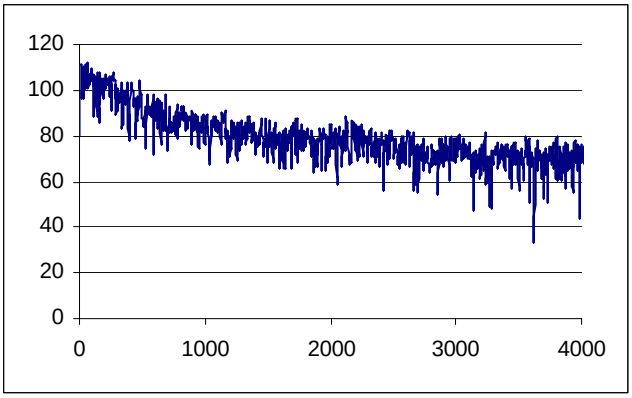
V = 84.46 ft/s	Amplitude (dB SPL)	No Data Collected

Figure 4.7 Plot 3 of Tangential Baseline Frequency Response with flow at indicated velocities.

Concerning the tangential baseline plots, of particular note is the absence of any pressure peaks in any of the velocities presented. The presence of broadband noise across the spectrum demonstrates the lack of contribution swirl has to the generation of pressure pulses when subjected to the cavity.

Effects of Swirl

It is important here to remember that the testing of swirl effects was carried out with a fixed L/D = 0.9. This ratio was used since that obtained by Smith [5] and the authors earlier testing established the peak oscillations in that region. This was considered to be the optimum L/D. Figures 4.2 through 4.7 show the baseline graphs of the axial and tangential flows established in the trials for comparison with the mixed axial and tangential flow power spectra. The reader is directed to note the peak oscillation levels in each of the axial graphs and the lack of peaks in the tangential graphs. There exists a strong oscillation in each of the axial flow graphs, but only an expected level of noise in the tangential baseline graphs, well below 100 dB spl.

Figure 4.8 represents the visual effect of swirl on one of the flow conditions, where axial flow was set at 38.56 ft/s and the tangential flow established at 47.23 ft/s. It is interesting to note the structure of the flow at the exit and the apparent lack of a symmetric structure. What is interesting in figure 4.8 (b) through (d) is the appearance of a helical mode in the exit flow.

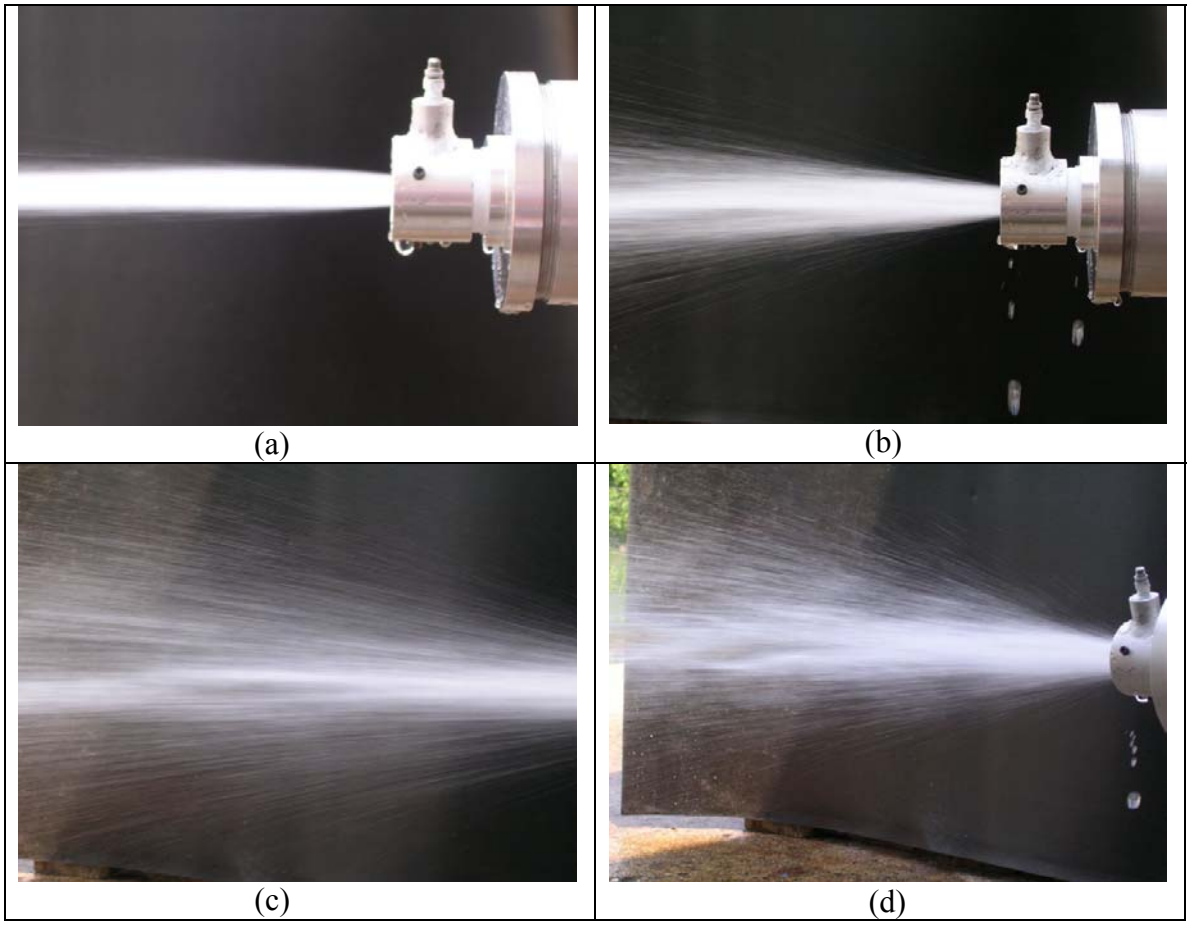

Figure 4.8. Effect of swirl on axial flow. (a) Axial velocity = 38.56 ft/s, (b) axial velocity = 38.56 ft/s with tangential velocity = 47.23 ft/s, (c) and (d) axial velocity = 47.23 ft/s and tangential velocity = 60.97 ft/s.

Frequency Peaks

The testing of lower L/D ratios presented some interesting results. The lower L/D exhibited the expected behaviour of producing high peak oscillations that increased in frequency coupled with evidence of harmonics of the primary peak. Figures 4.9 to 4.11 show the increasing progression of the peak oscillation as well as the harmonics.

For the lower L/D tests, the lowest L/D generated an interesting peak at low velocities, compared to the remaining L/D tests. In Figure 4.9, the peak shifted to the right with increased velocity, but appeared at a much higher frequency than expected. At the bottom of Figure 4.11, for V = 77.10 ft/s, there is a demonstration of the Rossiter mode (Equation 4.7) with associated frequencies f_1 = 1024 Hz, f_2 = 1952 Hz, and f_3 = 2976 Hz.

Cavity Modes

When viewing Rossiter's equation (Equation 2.1), the integer mode number (m) represents the wholesale jump in frequency recorded, as seen in the preceding analysis. There can be seen a differentiable shift in frequency peaks when the velocity of the flow is increased. This phenomenon is called mode shifting. Figure 4.10 shows the shift in primary peak when the velocity is increased from 66.79 ft/s to 77.13 ft/s. The primary peak is considered the highest level seen in the figure. Labels A and B indicate the same peak existing but that shift to the right when the velocity is increased. The mode shift occurs when peak B becomes the primary at 77.13 ft/s.

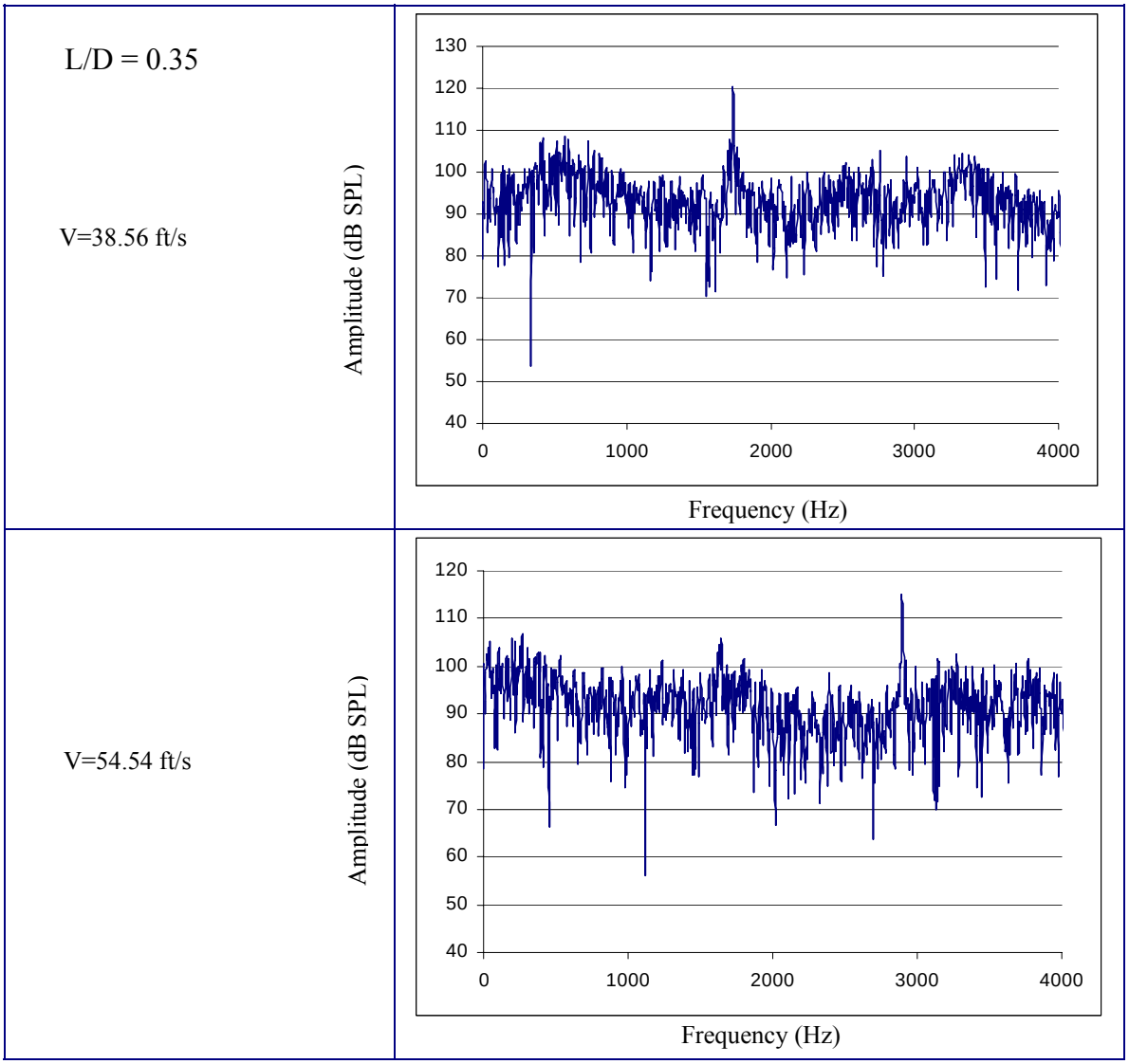

Figure 4.9. Graphs of Lower L/D Data (L/D = 0.35) with associated velocities listed.

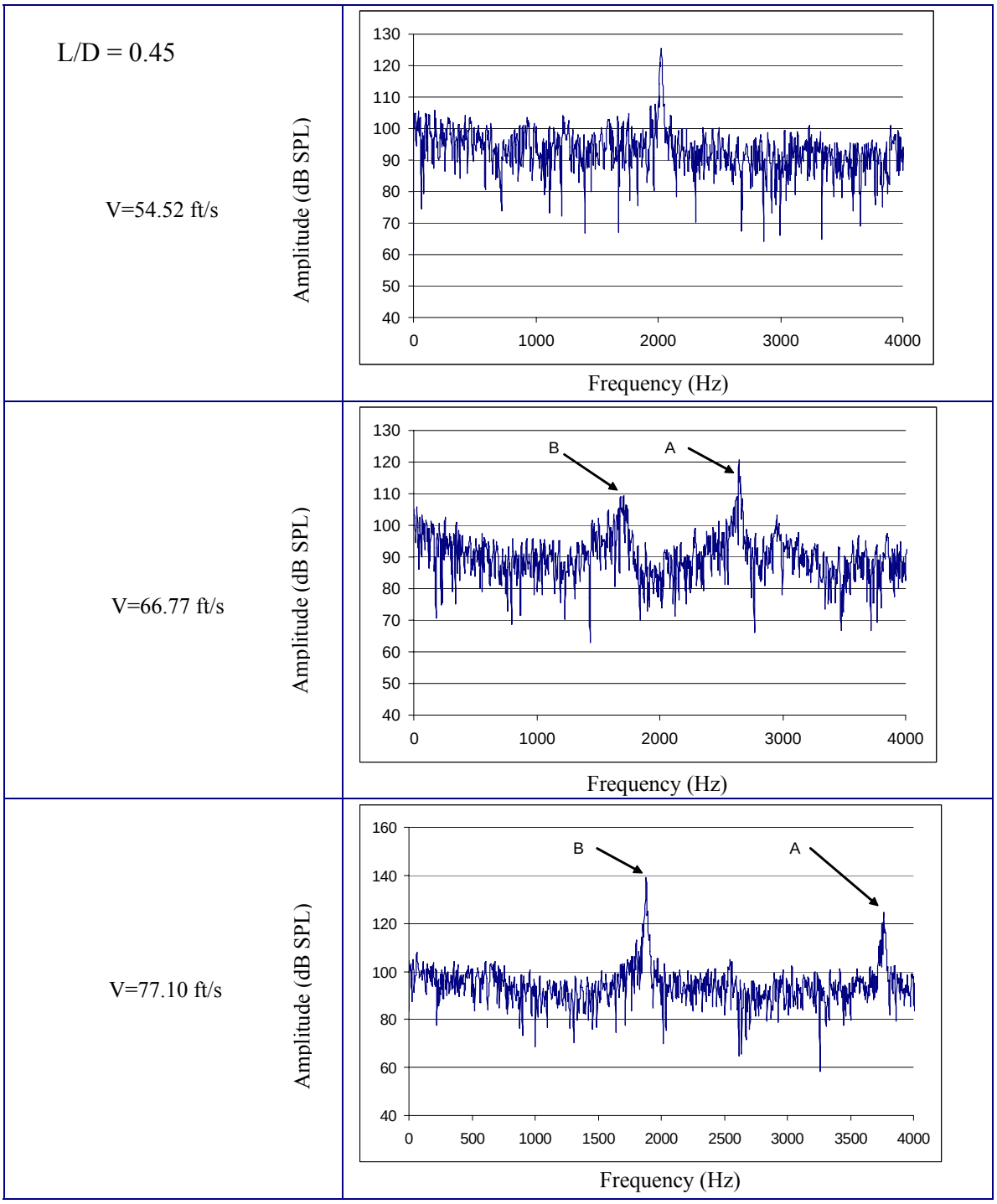

Figure 4.10. Graphs of Lower L/D Data (L/D = 0.45) with velocities listed. Peak A shifts right and decreases in intensity, while peak B shifts right and increases in intensity.

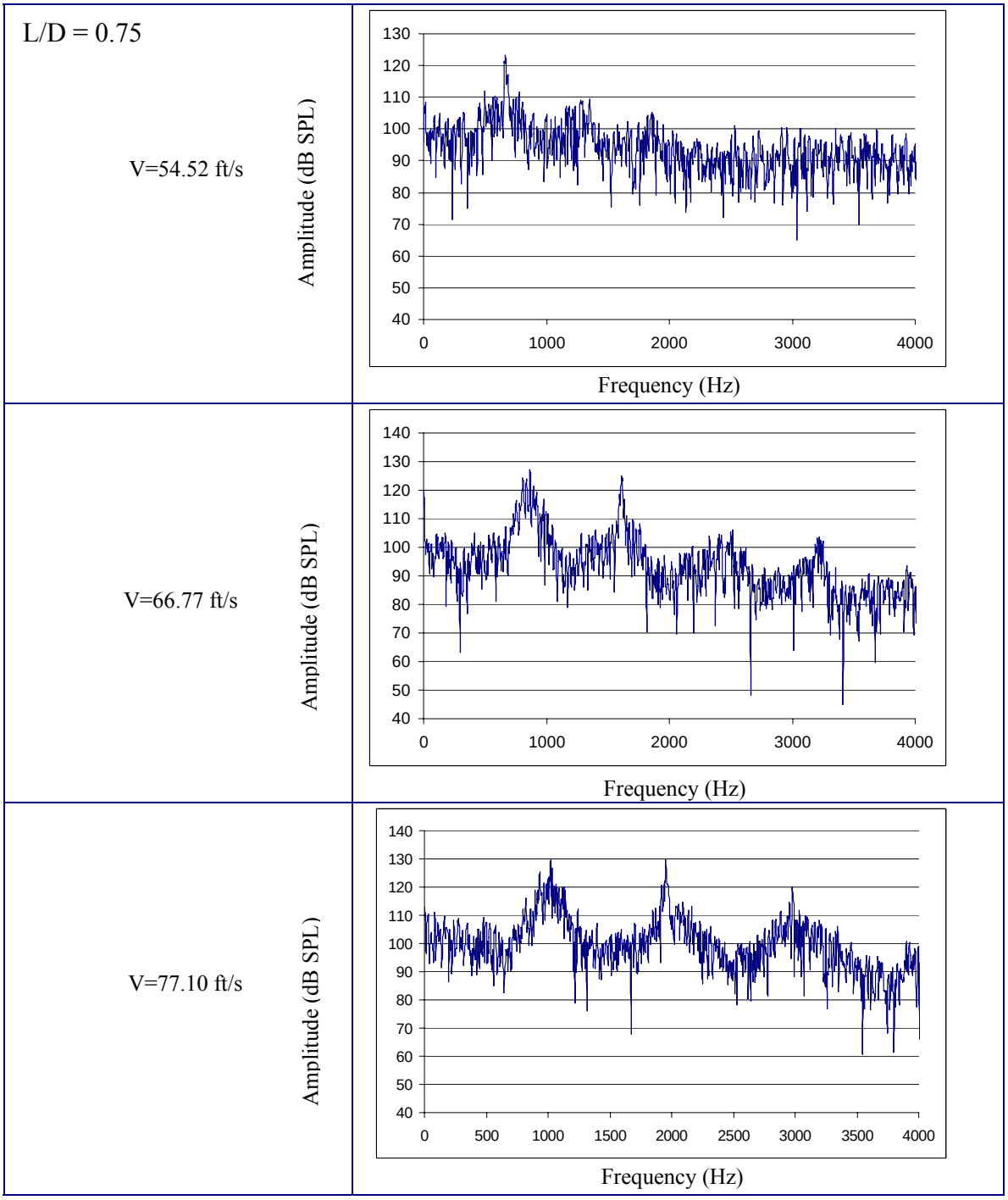

Figure 4.11. Graphs of Lower L/D Data (L/D = 0.75) with velocities listed. Note characteristic shift to the right with increased velocity.

We can experience pulses in "depth mode", occurring when the cavity depth is considered in pulse creation and is an integer multiple of the natural frequency of the cavity. The frequency is found through,

$$f = \frac{a_0}{\lambda} \tag{4.8}$$

with a_0 as the sound speed of water, and λ as the wavelength of the acoustic wave. Table 4.7 contains the values expected for the first four modes. Here we are using D = 0.5" (0.0417 ft), and a_0 = 4862.2 ft/s.

When compared to Equation (4.3), there are no frequencies encountered that confirm the existence of depth mode oscillations. Therefore, it will be assumed that depth mode is not being encountered in these tests.

The formula for the Helmholtz resonator is,

$$\frac{2\pi f_c l_T}{a_0} \tan \frac{2\pi f_c l_T}{a_0} = \frac{\pi R^2 l_T}{V_C} \tag{4.9}$$ [31]

with:

f_c = The natural frequency of the cavity;

l_T = The length of the throat;

a_0 = The speed of sound in the medium;

R = The radius of the pinhole; and

V_C = The volume of the cavity.

Table 4.7. Frequency with corresponding mode number.

Mode Number	$\lambda = \frac{2D}{m}$	f (equation 4.3)
1	0.0833	58369.75 Hz
2	0.0417	116599.5 Hz
3	0.0278	178899.3 Hz
4	0.0208	233759.6 Hz

The equation is solvable numerically and the corresponding graph in Figure 4.12 shows the behaviour of the Helmholtz resonator [5]. The data from this test is included for comparison.

The results agree well with the Helmholtz resonator in the range of L/D < 1.05, and with that of Smith [5] along the range tested.

Of note in Figure 4.13 is the apparently rapid increase in the frequency at very low L/D. It is unclear as to the reason for this occurrence. The structure of the apparatus precluded tests below L/D = 0.25 and the technique employed in collecting data only covered as small range of L/D < 0.4. It may be worth exploring the effect of an extremely low L/D and the effects on the frequency created.

Figure 4.14 shows another example of mode shifting with increased velocity. The peaks A and B shift to the right and switch in peak levels.

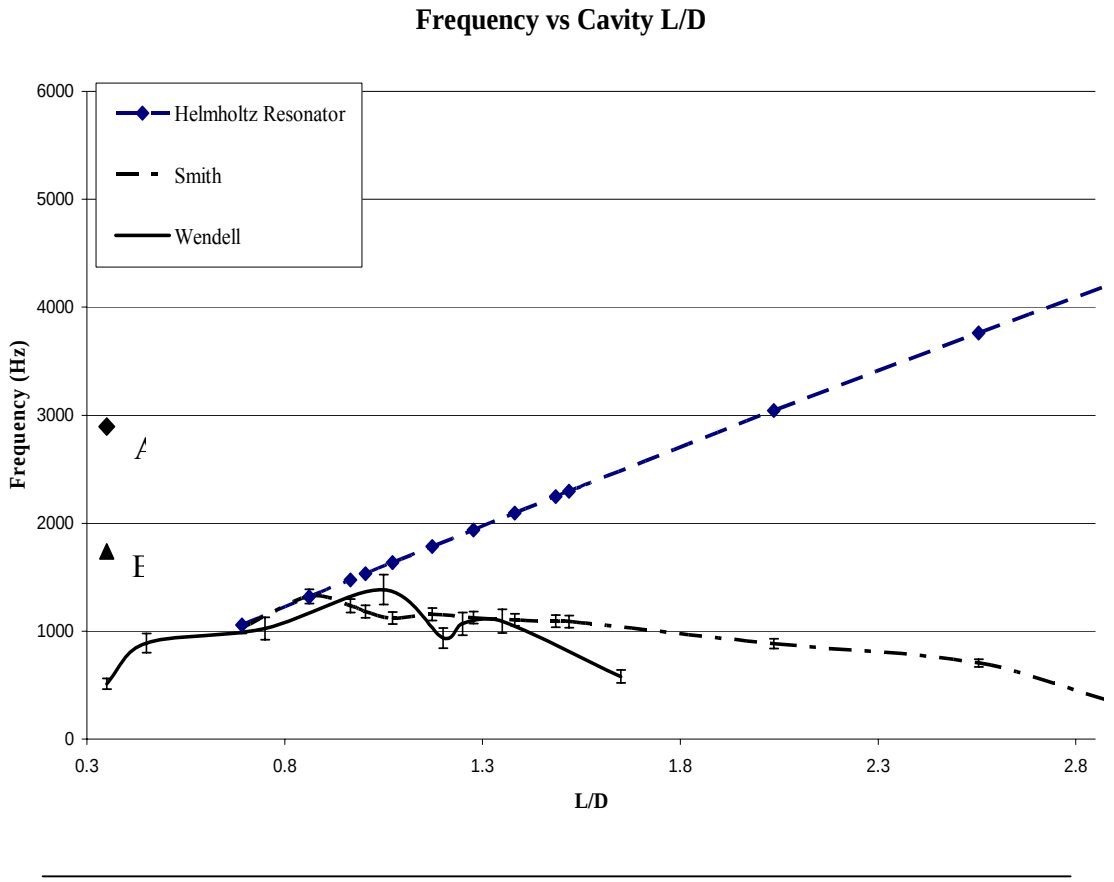

Figure 4.12. Plot of the Frequency versus L/D for Helmholtz Resonator, Smith [5], and tested results. Points A and B indicate the additional higher than expected frequencies encountered at the lowest L/D tested. Error bars set for 10% maximum error based on apparatus and set-up.

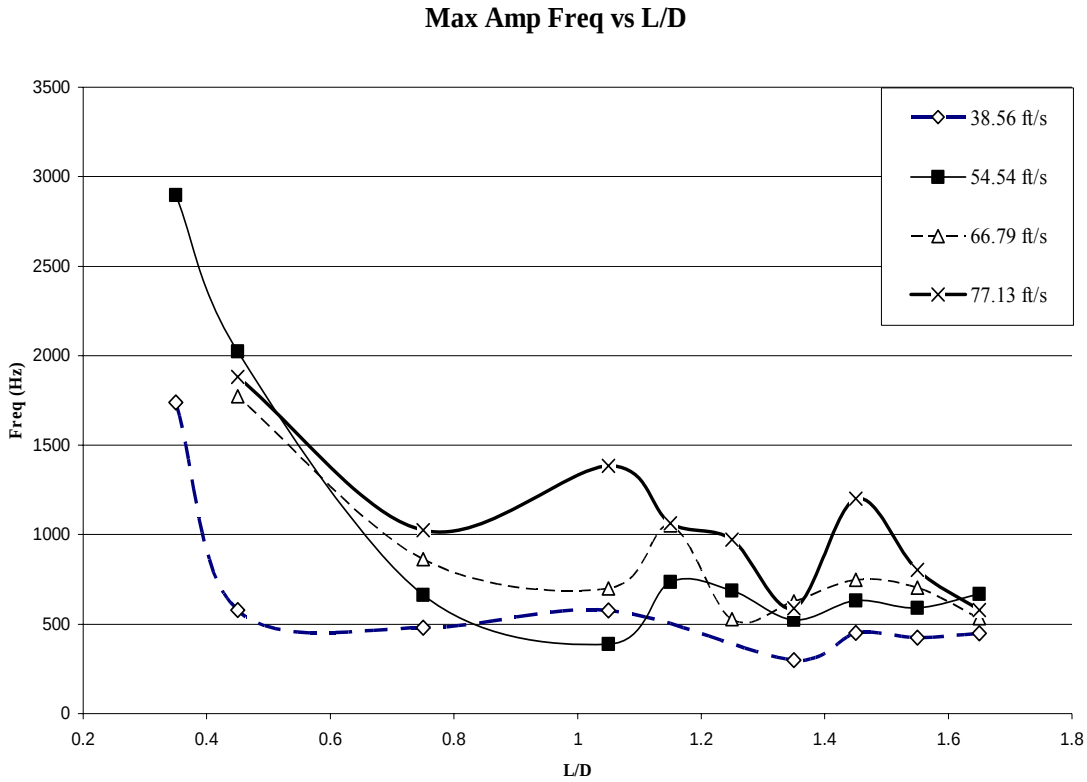

Figure 4.13. Plot of the frequency of maximum amplitude detected versus L/D at lower L/D ranges ($0.35 < L/D < 1.35$). Note the rapid increase in frequency at lowest L/D.

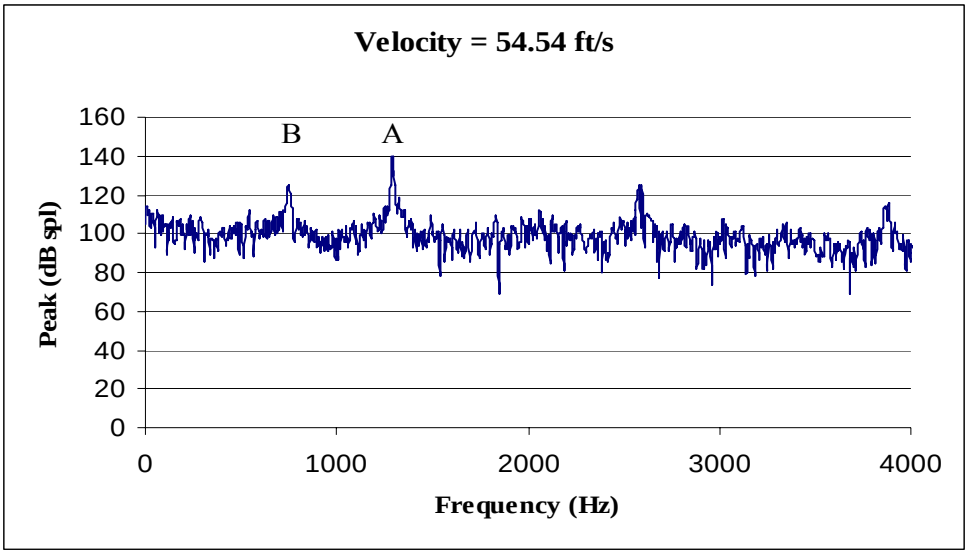

(a)

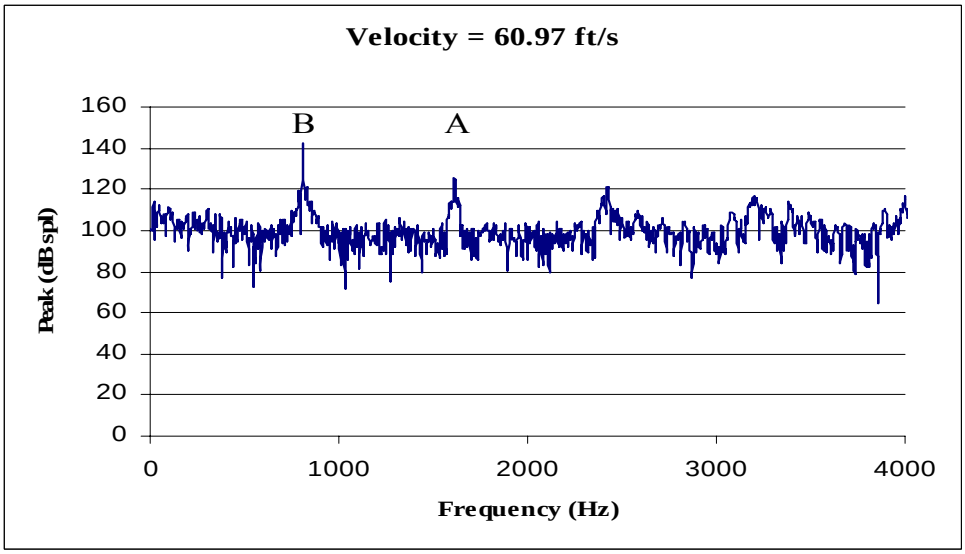

(b)

Figure 4.14. Graphs showing the mode shift with increase in flow velocity. Peaks are labelled A and B for demonstration and bookkeeping in this figure. In (a), peak A travels to the right with increased flow velocity and decreases in amplitude, in (b).

Swirl Flow

When swirl is introduced into the flow, the effect on frequency and peak oscillations is subtle yet present. The first mode of oscillation is cancelled when the swirl number reaches a strong swirl level ($S > 0.6$). Additionally, the second mode frequency response is seen to flatten in $S > 0.6$. Figure 4.15 shows the effect of swirl on the Strouhal Number, and the demise of the first mode at $S > 0.6$. With the error estimate at approximately 10%, the second mode of frequencies is grouped around $St = 0.8$, which agrees with that established by Chen [26], in that the maximum frequency occurs at $St = 0.92$.

An apparent trend in Figure 4.15 is the increase in Strouhal number in the region of weak swirl ($S < .3$) with a flattening of the curve at moderate swirl numbers ($S \approx 0.4$) and above ($S > 0.6$) in high swirl. The presence of helical modes in the cavity is one reason for the demise of the first Rossiter Mode.

The apparent trend shown in Figure 4.16 shows that there is a correlated increase in the peak amplitudes detected with associated increase in swirl number. The trend lines have been placed for demonstration of the apparent trend only.

In Figure 4.17, there is an evident increasing trend in frequency with an increased Reynolds number. In this plot, the increased Reynolds number represents an increase in velocity of the flow. When the same plot is presented as Strouhal Number versus Reynolds Number Figure 4.18, the evidence shows that the Reynolds Number has no effect on the Strouhal Number as expected.

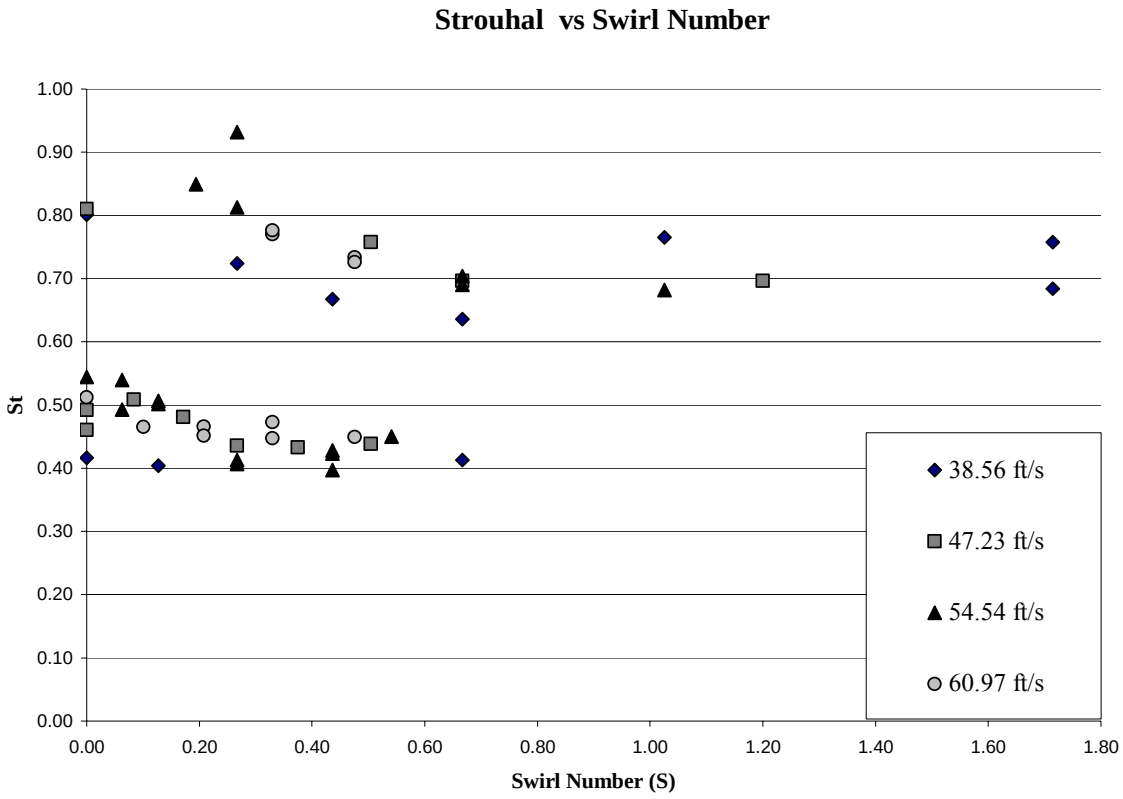

Figure 4.15. Plot of Strouhal Number versus Swirl Number.

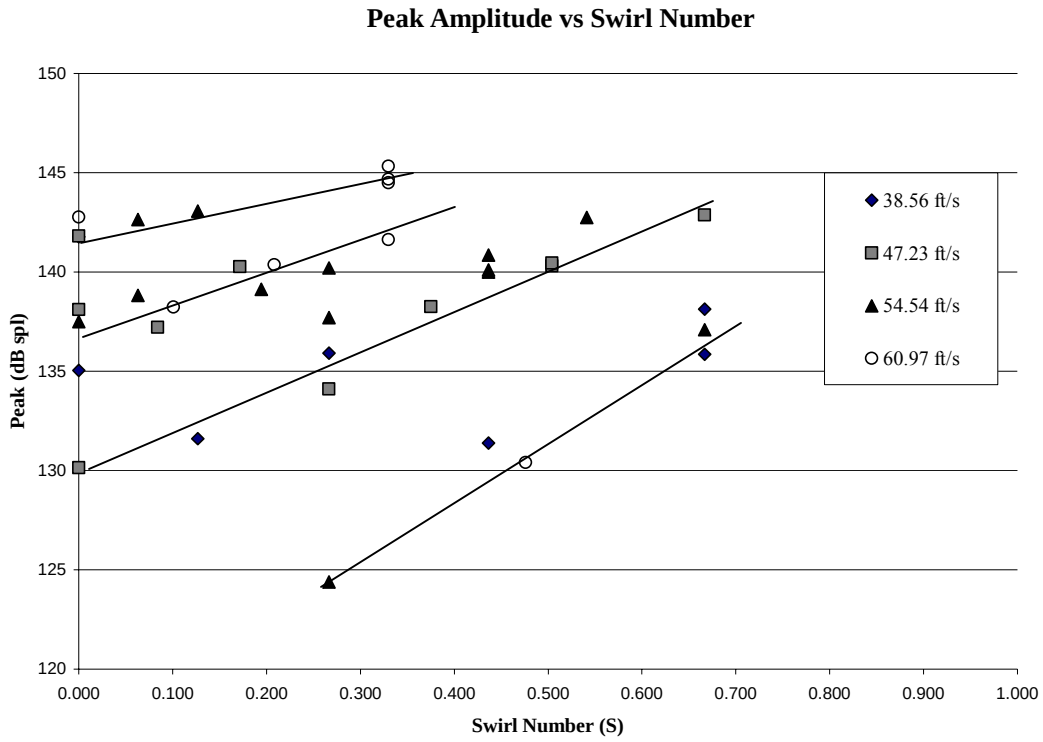

Figure 4.16. Plot of peak amplitudes detected versus swirl number. Note increasing trend with higher swirl number.

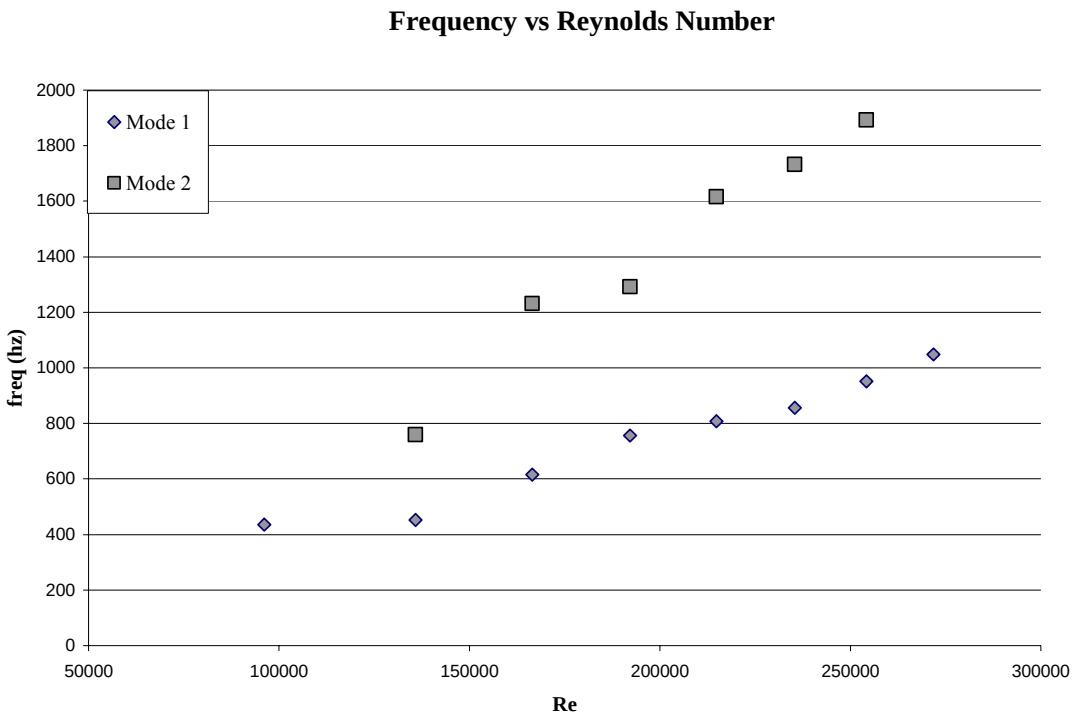

Figure 4.17. Plot of frequency versus Reynolds number for the range of L/D in this study.

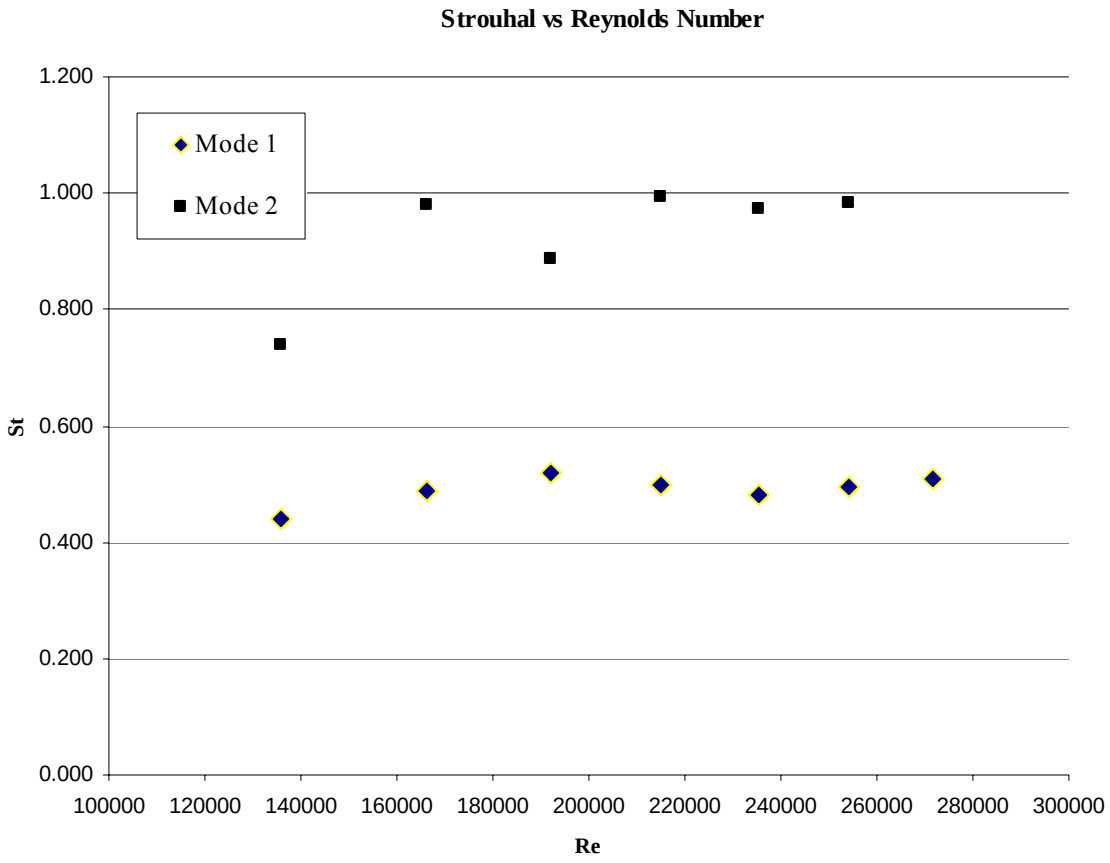

Figure 4.18. Plot of Strouhal Number versus Reynolds number for the range of L/D in this study.

The effects of swirl are presented in Figures 4.19 and 4.20 at the fixed axial velocity of 54.54 ft/s. The baseline plot (top of Figure 4.19) is also presented here. Note the presence of multiple peaks the shifting to the right, with the reduction in the number of peaks at higher swirl velocities.

Inlet Orifice Damage

During the tests, it was noted that there was an abrupt discontinuation of the oscillations. It was discovered that the inlet orifice has failed (see Figure 4.21) during the pressure runs. The possible cause of failure could be attributed to either the material being fatigued through use in the tests, or that the natural frequency of the inlet orifice was reached, causing it to fail under stress. It is unfortunate that a structural analysis could not be carried out prior to publication of this paper.

Helical Modes and Aliasing

It is possible for aliasing to present an expected frequency as shown on Table 2.7, for the first helical mode ($j'_{1,0}$). Notwithstanding, longitudinal modes may also be present. Figure 4.22 shows the effect of aliasing on the output waveforms. An example of aliasing in the longitudinal mode is presented in Figure 4.22 (a). The effect is demonstrated at peaks B and C. Peak B is the second mode, and Peak C the third mode. Using the aliasing formula, peak (C) in Figure 4.22 (a) occurs as expected with an error of less than 0.5%.

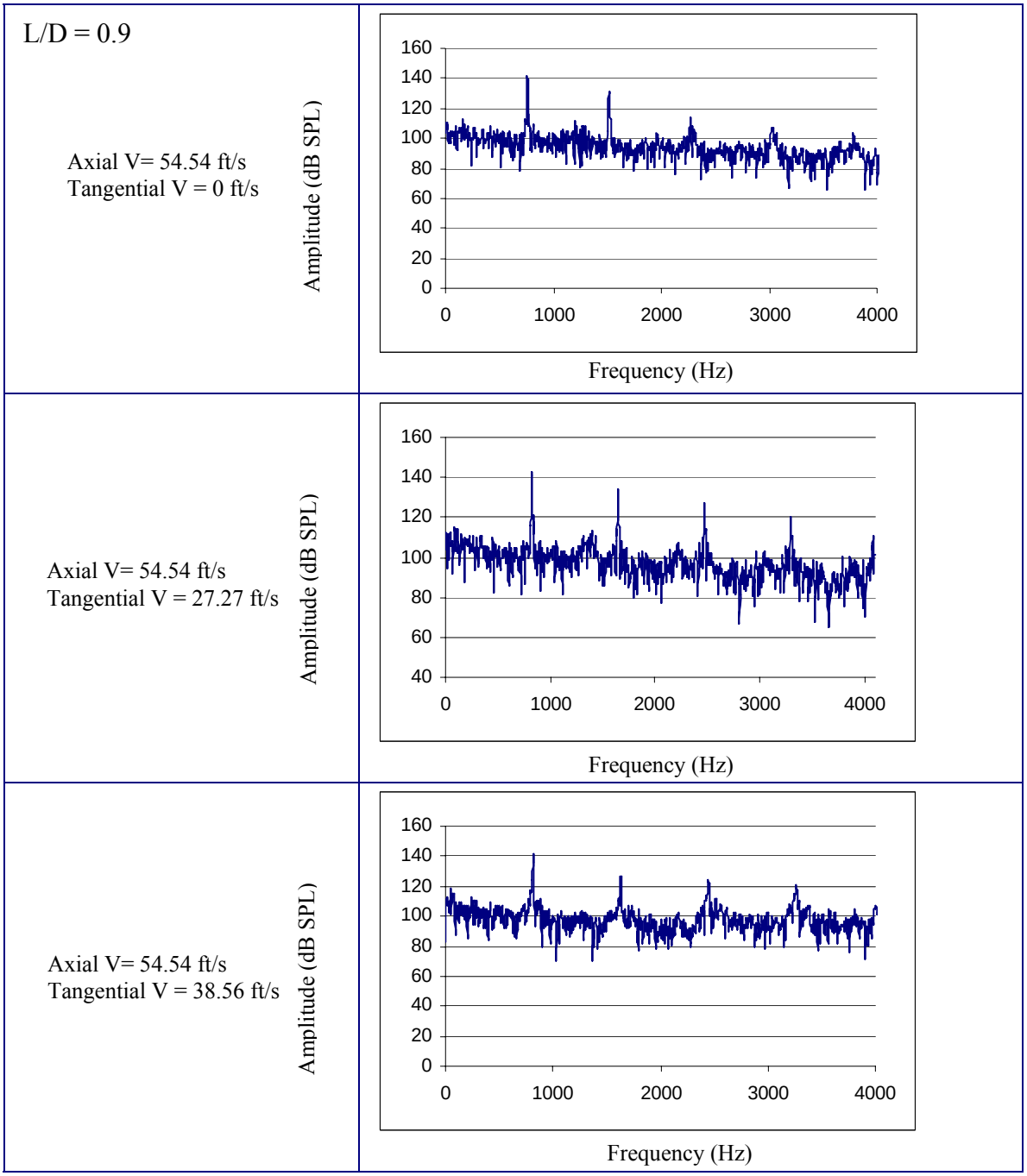

Figure 4.19. Plot 1 of power spectrum for Axial and Tangential flow. Velocities are recorded and placed beside respective graph.

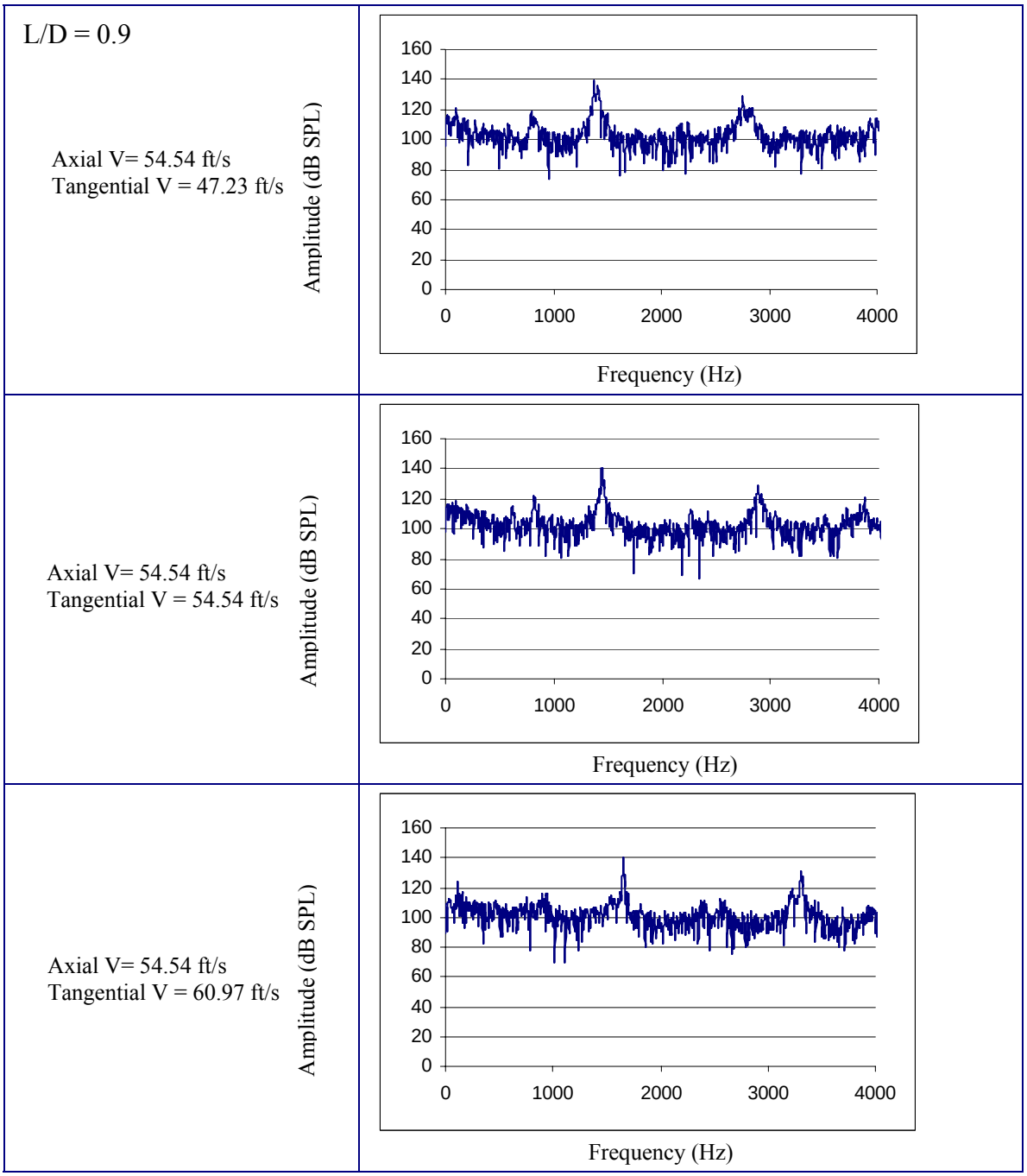

Figure 4.20. Plot 2 of power spectrum for Axial and Tangential flow. Velocities are recorded and placed beside respective graph.



Figure 4.21. Photos of inlet orifice cap damage after testing. Note replacement inlet orifice with thicker orifice wall at lower right (for comparison).

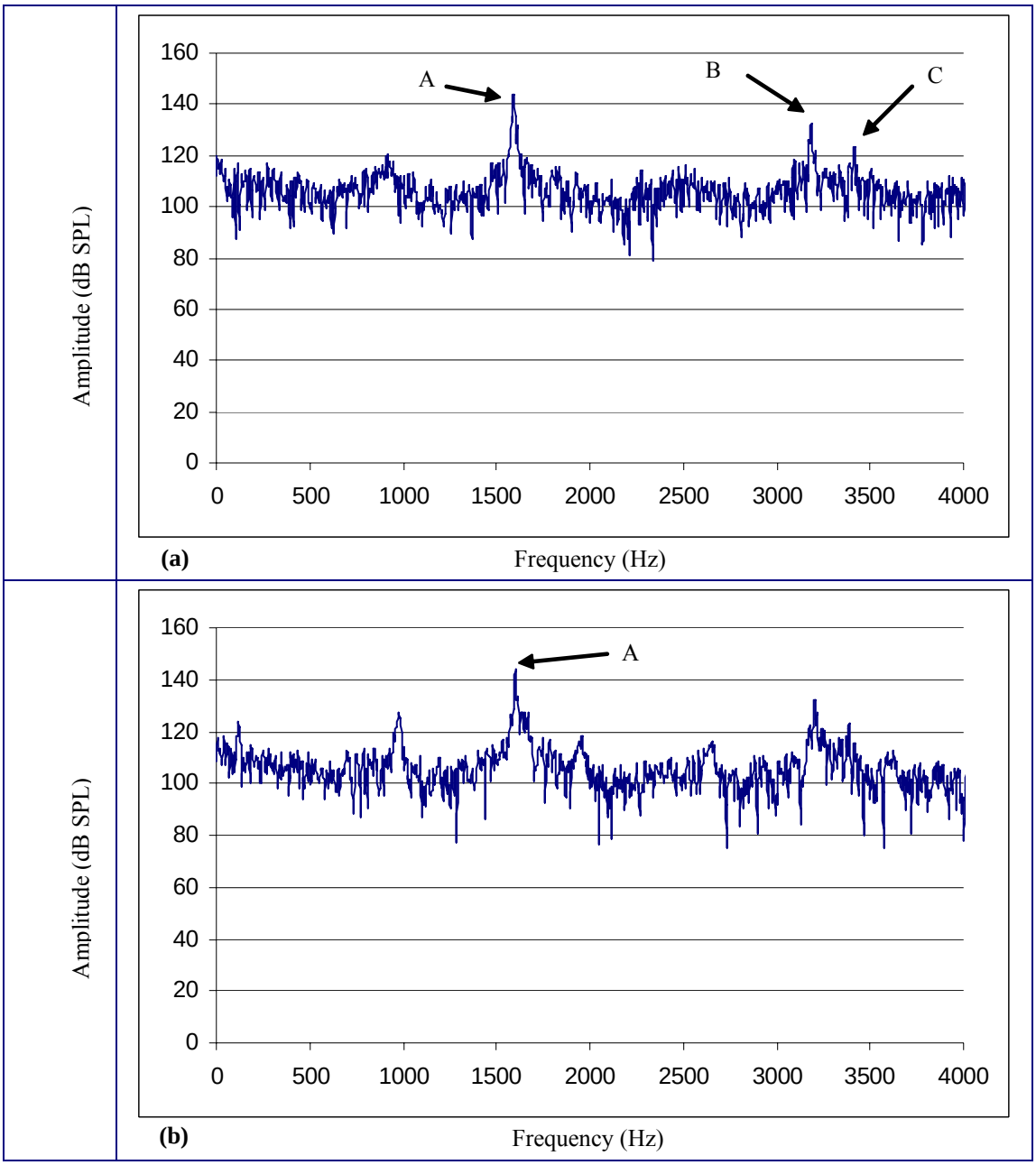

Figure 4.22 Plot of the aliasing effect on longitudinal and helical modes. Velocities are the same for each plot. In (a), the longitudinal mode is demonstrated. Point A is the primary, point B is the second mode, and C is the aliased third mode frequency. In (b), the helical mode is demonstrated. Point A is the expected frequency of the first helical mode. Velocities are Axial = 60.97 ft/s and tangential = 77.13 ft/s.

Figure 4.22 (b) is an example of the helical mode aliasing. Peak (A) is the expected frequency based on Equations 2.16 and 2.17. The velocities are the same for Figures 4.22 (a) and (b), with the axial velocity of 60.97 ft/s, and the tangential velocity set for a total of 77.13 ft/s.

Figure 4.23 and Figure 4.24 show the same result expected for the first helical mode, with an error of approximately 5% in the observed frequency.

It should be noted here that the first helical mode is present only with higher axial and tangential velocities. Of particular note is the peak aliased frequency of Figure 4.24 at axial velocity = 60.97 ft/s and tangential velocity at 81.81 ft/s. The error here is approximately 0.12%.

Figure 4.25 shows the trend experienced with higher swirl velocities present, approaching that of the calculated frequency in Equation (2.17). The tests here were limited in maximum velocity to below 84 ft/s. Further study of the effects above this limit is recommended.

It must be born in mind that the present study does not confirm the presence of the helical modes, only the supposition of their presence. The aliasing theory presented does not clearly determine the presence of these helical modes, but offers some evidence that they may exist in theory. With the low sampling rate and high frequencies experienced in this study, it is proposed that the first helical mode is indeed present, but there may exist other modes that have not been analysed or confirmed. Notwithstanding, having determined the potential presence of first helical mode through the analysis of several higher swirl velocity tests, the author recommends further study in this regard.

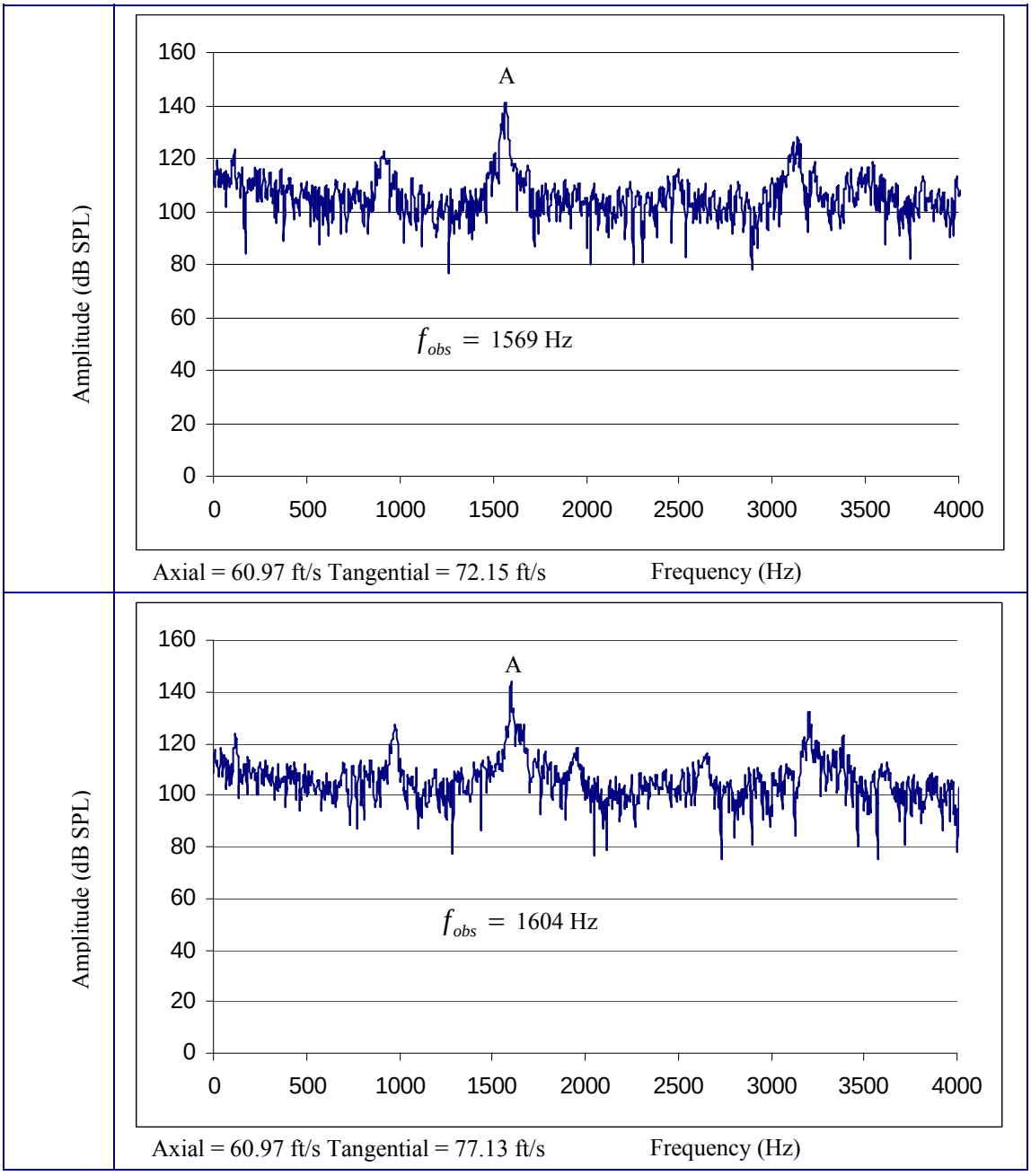

Figure 4.23 Plot 1 of the first helical modes (peak A) present in swirled flow. Velocities are expressed in each plot.

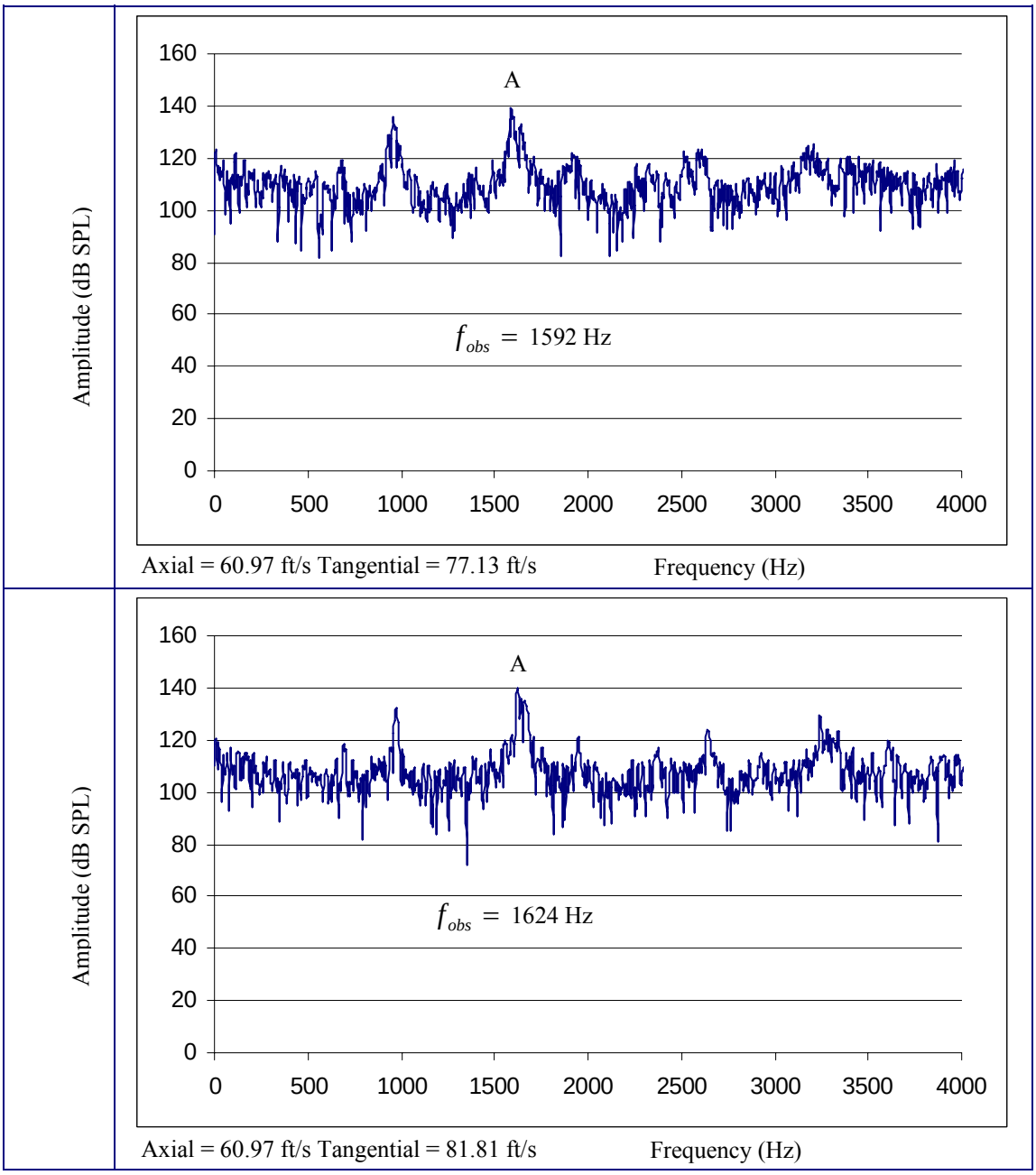

Figure 4.24 Plot 2 of the first helical modes (peak A) present in swirled flow. Velocities are expressed in each plot.

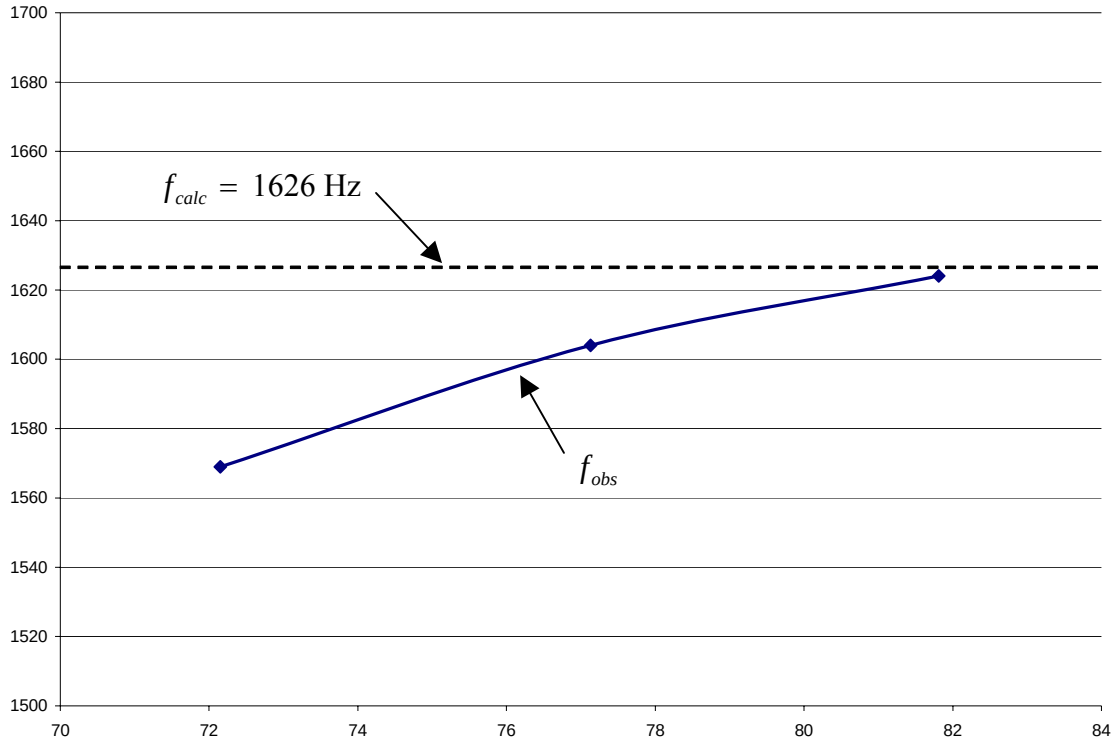

Figure 4.25 Plot of the trend in observed frequency with increased swirl velocity.

Chapter 5

Conclusion

Results

This study is both a continuation and incremental step forward in ongoing research at the University of Tennessee Space Institute. The goal of this study is to accomplish a deeper understanding of cavity instabilities, both with and without swirl introduced. Furthermore, it is our goal to make use of the instabilities to attenuate or to amplify their effects on cavity flows. The original experimental procedure was re-designed to examine the unsteady pressure pulses that occur when an incompressible fluid (water) flows through an axisymmetric cavity at wider range of length to depth ratios (L/D) than that of previous studies. The L/D examined in this study ranged from 0.25 to about 1.5, with the average flow Reynolds numbers ranging from 100,000 to 530,000.

Results establish that, without swirl, large amplitude oscillations are generated in the cavity for specific length to depth ratios for a given flow rate. As the length to depth ratio increases the maximum amplitude decreases, but the frequency of the maximum amplitude is greatest at a length to depth ratio of approximately 0.85. As the flow rate decreases, the value of the maximum amplitude and its frequency decreases. For shorter length to depth ratios ($0.2 < L/D < 0.6$) the cavity has a behaviour analogous to a Helmholtz Resonator, and at $L/D > 0.9$ presented similar to Rossiter's Empirical observations. Higher L/D ratios ($L/D > 1.65$) did not display appreciable oscillations at the speeds studied in this work.

The results also show close agreement with previous studies concerning the region of Strouhal number that exhibits the highest peak oscillation amplitude. The maximum peak oscillations occurred around St = 0.8 in this work.

Additionally, the analysis of the variable cavity chamber L/D confirmed that the Reynolds Number has no effect on the Strouhal number, consistent with previous studies.

Swirl was introduced to change the stability characteristics of the flow, at a fixed L/D ratio (L/D = 0.9). The primary goal of this research was to study the changes which may be implemented by introducing swirl. The swirl flow injected tangentially within a restricted range of velocities achieved a marked change in peak frequencies observed. The greatest change in peak frequencies was noted for the axial velocity of 47.23 ft/s with the tangential range of 38.56 to 54.54 ft/s. The first Rossiter mode was not present with the swirl at and above moderate swirl (S > 0.3) and there was a marked division of modes when measured at specific velocities. Mode jumping was noted with regularity as well as an apparent helical structure visible in the cavity exit flow. It was noted that, with a fixed axial velocity, only highest tangential velocities tested in this study resulted in little or no cavity oscillations.

It can be surmised that the effect of higher swirl significantly change the shear layer developed inside the cavity. This is responsible for the creation or lack thereof the pressure oscillations, and that only a certain range of axial and tangential velocities affected the flow. It was observed that with higher swirl velocities there was evidence of the presence of the first helical mode in the flow. The observed frequency plots agreed well with that of the calculated frequency for this geometry. With higher swirl velocities, a trend was observed where the frequency observed (f_{obs}) approached that of the

calculated frequency. The trend indicated an approach to theory at higher velocities but the limit of test velocity was achieved and could not be explored further. Albeit the presence of these observed peaks occurred with only some regularity, this was evidence of the first helical mode.

Future Study

Having explored a limited range of velocities in these tests, it is recommended that future work carry the investigation of cavity flow with swirl to higher velocities. Additionally, the miniaturization of the apparatus presents an interesting field of study and applications.

With the tremendous amount of broadband noise present in the pressure spectra, the possibility of applying filters, to cancel out noise as well as aliased frequencies, could possibly present a clearer picture in the measurements analysis.

It is also recommended that further study of the helical modes and the presence of helical frequencies be undertaken.

List of References

List of References

1. Rossiter, J.E., "Wind-Tunnel Experiments on the Flow over Rectangular Cavities at Subsonic and Transonic Speeds," *Reports and Memoranda* No. 3438, 1964.
2. Chahine, G.L. and Johnson, V.E., "Mechanics and Applications of Self-Resonating Cavitating Jets," *Jets and Cavities – International Symposium*, ASME, FED – Vol.31, 1985.
3. Meganathan, A.J., "Flow of Jets Passing Over Axisymmetric Cavities," Ph.D. Dissertation, University of Tennessee, August 2005.
4. Meganathan, A.J., "An Experimental Study of Low Speed Open Cavity Flows," M.Sc Thesis, University of Tennessee, December 2000.
5. Smith, J.D.B., "An Experimental Study of Axisymmetric of Cavity Oscillations in Low Speed Incompressible Flow," M.Sc Thesis, University of Tennessee, December 2000.
6. Chahine, G.L., Johnson, V.E., and Frederick, G.S., "Self Resonating Pulsed Water Jets for Aircraft Coating Removal: Feasibility Study," Hydronautics, Inc., Laurel, MD, Technical Report 8268-1, June 1982.
7. Majdalani, J., "A Novel Flow Field Solution in a Rectangular Cavity Subject to Small Amplitude Oscillations," AIAA Paper No. 98-2693.
8. Colonius, T, Basu, A.J., and Rowley, C.W., "Numerical Investigation of the Flow Past a Cavity," AIAA Paper No. 99-1912.

9. Guo, Z. and Dhir, V.K., “Single- and Two-Phase Heat Transfer in Tangential Injection-Induced Swirl Flow,” *International Journal of Heat Transfer and Fluid Flow*, Vol. 10, No. 3, September 1989.
10. Gupta, A.K., Lilley, D.G., and Syred, N., *Swirl Flows*, First Ed., Abacus Press, 1984.
11. Vakili, A.D., and Gauthier, C., “Control of Cavity Flow by Upstream Mass Injection,” *AIAA Journal of Aircraft*, Vol 31, No. 1, 1994.
12. Lucas, M.J., *Handbook of the Acoustic Characteristics of Turbomachinery Cavities*, First Ed., ASME Press, 1997.
13. Fick, W., Griffiths, A.J., and O’Doherty, T., “Visualization of the Precessing Vortex Core in an Unconfined Swirling Flow,” *Optical Diagnostics in Engineering*, Vol. 2(1), 1997.
14. Kikuyama, K., Murakami, M., and Nishibori, K., “Development Of Three-Dimensional Turbulent Boundary Layer in an Axially Rotating Pipe,” *AIAA/ASME Joint Fluids, Plasma, Thermodynamics and Heat Transfer Conference*, St. Louis MI, June 7-11, 1982.
15. Gauthier, C., “Experimental Study of Cavity Flow Oscillations with Upstream Mass-Injection,” M.Sc Thesis, University of Tennessee, December 1990.
16. Baker, D.A., “Investigation of Aeroacoustics of an Axisymmetric Cavity,” M.Sc Thesis, University of Tennessee, August 2000.
17. Rowley, C.W., Colonius, T, and Basu, A.J., “On Self-Sustained Oscillations in Two-Dimensional Compressible Flow Over Rectangular Cavities,” *Journal Fluid Mech*anics., Vol. 455, 2002, pp 315-346.

18. Heller, H.H. and Bliss, D., “The Physical Mechanism of Flow-Induced Pressure Fluctuations in Cavities and Concepts for their Suppression,” AIAA Paper 75-491, 1975.

19. Heller, H.H., Holmes, D.G., and Covert, E.E., “Flow-Induced Pressure Oscillations in Shallow Cavities,” *Journal of Sound and Vibration*, Vol. 18(4), 1971.

20. Chen, C.H., “Study of Subsonic and Transonic Flow Separation – With and Without Upstream Disturbances,” Ph. D Dissertation, University of Tennessee, 1975.

21. Gauthier, C., “Experimental Study of Cavity Flow Oscillations with Upstream Mass Injection,” MSc Thesis, University of Tennessee, 1990.

22. Karamcheti, K., “Acoustic Radiation from Two-Dimensional Rectangular Cutouts in Aerodynamic Surfaces,” NACA TN 3487, 1955.

23. White, F.M., *Viscous Fluid Flow*, Second Ed., McGraw-Hill, 1991.

24. Tam, C.K.W., and Block P.J.W., “On the Tones and Pressure Oscillations Induced by Flow Over Rectangular Cavities,” *Journal of Fluid Mechanics*, Vol. 89, Part 2, 1978.

25. Ho, C.M., and Heurre, P., “Perturbed Free Shear Layers,” *Annual Review of Fluid Mechanics*, Annual Reviews Inc., 1984.

26. Chan, Y.Y., “Spatial Waves in Turbulent Jets,” *Physics of Fluids*, Vol. 17, American Institute of Physics, 1974.

27. *Piezotron*^{TM} *– Miniture, High Sensitivity, Voltage Output Pressure Sensors*, Kistler Instrument Corporation, 2003.

28. *Instruction Manual, Universal Pressure Transducers, Types 211B(X),* Kistler Instruments Corportation, 2003.

29. Goldstein, R.J., ed, *Fluid Mechanics Measurements,* Second Edition," Taylor and Francis, 1996.

VITA

Lee Charles Wendell was born in Ottawa, Ontario, Canada on October 7, 1964. He graduated from Nicholson Catholic College in 1983 and after a period of employment in Toronto, joined the Canadian Armed Forces in 1986 as an Integral Systems (IS) Technician. Completing his maintenance training in 1987, he was posted to the Base Aircraft Maintenance Engineering Organization in Trenton, Ontario, employed on several aircraft types, including the Boeing 707 and Lockheed C-130 Hercules. In 1990, he was posted to Halifax and Shearwater, Nova Scotia, where he completed his Avionics (AVS) Technician training course, and was employed on the Sikorsky CH-124 Sea King helicopter. During his employment at 12 Aircraft Maintenance Squadron (AMS) in Shearwater, he applied and was accepted for the University Training Plan for Non-Commissioned Members (UTPNCM). He attended and graduated from Saint Mary's University, Halifax, Nova Scotia in 2000, with a double honours degree in Physics and Mathematics. From here he attended the Aerospace Engineering Officer Basic Course (AOBC) at the Canadian Forces School of Aerospace Technology and Engineering (CFSTAE) in Borden, Ontario. Upon completion of AOBC, Lee was posted to 8 AMS Trenton where he was employed as the Quality Manger and Unit Safety Officer for two years. Promoted to Captain in May 2003, his final year at 8 AMS was spent as the Aircraft Servicing Officer (ASO), responsible for the maintenance, scheduling, and organization of Canada's military airlift capability. Lee applied and was selected for Sponsored Post Graduate Training at the University of Tennessee Space Institute in

August 2004, and then completed the requirements for the Masters of Science Degree in Aerospace Engineering in December 2006. Captain Lee Wendell is posted to the Aerospace Engineering Test Establishment (AETE) in Cold Lake, Alberta, where he will be employed as the aerodynamic specialist for fighters and trainers in the Canadian Air Force.